The Development of Active Water Scintillator for the T2K Experiment

Marieke Navin

Department of Physics and Astronomy
University of Sheffield

Thesis submitted for the Degree of Doctor of Philosophy in the University of Sheffield

· March 2010 ·

To Jon and Tilly

Abstract

The Tokai to Kamioka (T2K) experiment started taking data in January 2010. Using the most intense source of man-made neutrinos the experiment will study oscillations of an off-axis muon neutrino beam between the JPARC accelerator complex and the Super-Kamiokande Detector 295 km distant. The unknown mixing angle θ_{13} will be measured by observing the $\nu_\mu \rightarrow \nu_e$ oscillation. The neutrino energy spectrum, flavour content and interaction rates of the unoscillated beam will be measured by a set of detectors located 280 m (ND280) from the neutrino production target, which is where the UK effort is focussed.

Currently some of the ND280 sub-detectors contain passive water layers that are added to provide an oxygen rich target to reduce the systematic uncertainties that will arise by comparing signals between the Super-Kamiokande water Cherenkov detector and the primarily plastic ND280. This thesis presents the motivation for and development of active water-based scintillator layers to replace the passive layers thereby providing extra kinematic information of neutrino interactions. It is found to be a worthwhile endeavour if certain experimental challenges can be overcome.

Contents

List of Figures

List of Tables

Acknowledgments

There is a saying in Africa that it takes a whole village to raise a child. In my case, it takes a whole department to support one girl to do a PhD! There are so many people to thank, without whom I would never have got this far; indeed I never really thought that this day would come!

First and foremost thanks must go to Lee, my supervisor, for never giving up on me despite the obstacles I have faced. It all started with frozen chickens! I am indebted to Lee for giving me this chance and helping me finally get to this point. Thanks for being a brilliant travel companion (even long haul) and for giving me all the fantastic opportunities that doing this thesis presented. Huge thanks must also go to John MacMillan and Phil Lightfoot for their untiring help on all aspects of the scintillator hardware. Thanks to Susan Cartwright for her unending patience on the Theory of Everything and always finding time to explain the ins and outs of neutrino physics to me, and for also reading through the first draft of the thesis, red pen in hand. Thanks to Matt Robinson and Paul Hodgson for their computer support and all things technical. Thanks to Rob Duxfield for coding advice and to Jon Perkin for being the local ROOT guru. Thanks to Greg Ward, Mark Ward and Ben Still for useful discussions and help in the lab and to Omar Veledar for off-topic discussions. Also, huge thanks to the technicians who helped with the building of the prototype detector. This list comes no-where near

to thanking everyone in the HEP group and the department as a whole for all the support, advice and useful discussions I have had over the years. Thanks also to the T2K collaboration in the UK and all over the world. Especially to Stan Yen and all the UBC and TRIUMF scientists who helped me during the scintillator development of this thesis.

Finally this thesis would not have been possible without the emotional support of my non-physics friends (and for looking after me in Sheffield in the final stages of this thesis), and the yummy mummies for helping me through the early stages of having a baby while trying to finish up. Also thanks to my boss at the Museum of Science and Industry for the extra unpaid leave on the end of my maternity leave, which was invaluable for finishing the final experimental section of the thesis. There are not enough words to thank all of my family for all helping to babysit while I finally finished. And finally thanks to Jon for his constant companionship and faith in me and for being so supportive. I would never have managed without you.

Chapter 1

Neutrino Physics

Chapter 1 of this thesis summarises the history and our understanding of neutrinos and neutrino oscillations. Chapter 2 describes the T2K experiment, which aims to precision measure some of the parameters of neutrino oscillation. Chapter 3 describes the motivation for including active water scintillator layers in some of the T2K sub-detectors. Chapter 4 describes the development of this water-based scintillator and chapters 5 and 6 discuss the experimental methods and techniques to build the hardware for such sub-detectors including the design, construction and testing of a detector prototype. Finally, in Chapter 7 a discussion summarising this work and making predictions for future work is given.

1.1 Neutrinos in the Standard Model

The neutrino is one of the elementary particles which make up the Universe. Neutrinos are produced in the fusion reactions inside the Sun and other stars, by natural background radiation inside the earth, by supernovae, by charged particles bombarding the Earth's atmosphere and were also produced in the Big Bang. Neutrinos are the second most abundant known particle after cosmological photons; on average there are several hundred neutrinos per cubic centimetre of space and billions penetrate our bodies unnoticed every second. Despite their abundance, neutrinos remain mysterious because they are difficult to observe.

The Standard Model of particle physics provides a consistent theory of the fundamental particles and their electromagnetic, weak and strong interactions [1]. There exist two types of fundamental particles: fermions and bosons. The fermions are divided into leptons which experience only the electroweak force and quarks which feel both the electroweak and the strong force. The fermions are summarised in table 1.1. Particle interactions are mediated in the Standard Model by gauge boson exchange: photons for electromagnetism, W and Z bosons for weak interactions and gluons for strong interactions.

Neutrinos belong to the lepton family of particles and exist in three

Particles	Flavour			Charge
Quarks	u	c	t	$+\frac{2}{3}$
	d	s	b	$-\frac{2}{3}$
Leptons	e	μ	τ	-1
	ν_e	ν_μ	ν_τ	0

Table 1.1: Table of elementary fermion particles in the Standard Model.

flavours: ν_e, ν_μ and ν_τ. Each forms a doublet with its corresponding charged lepton: the electron, muon and tau. In this model, massless neutrinos exist only in these left-handed doublets, partnering the charged leptons. Since, in the Standard Model, the masses for the quarks and charged leptons are generated through the Higgs mechanism, which requires right-handed fields, the neutrinos remain massless and their helicity state is fixed: left-handed for neutrinos and right-handed for anti-neutrinos. The number of light neutrinos (i.e. those with $m < m_Z/2$) are confirmed to be 2.984 ± 0.008 by the LEP experiments [1].

Lepton number is always conserved so neutrinos are always associated with charged leptons of the same generation, or produced in particle-antiparticle pairs [2]. Having neither colour nor charge, neutrinos are the only particles to interact predominantly via the weak interaction. The large mass of the W and Z bosons means that the weak force only applies over very short distances, rendering it a notably weaker force than the strong or electromagnetic forces and thereby making the interactions of neutrinos extremely difficult to detect.

The Standard Model has been widely tested and is remarkably successful at describing many observed phenomena. It is however an incomplete theory, since there is no unification of the strong and electroweak forces and gravity is not incorporated in the model at all. Furthermore integral empirical patterns are not explained, such as the existence of three generations of fermions of increasing mass and why the quarks and leptons have the masses they do. It also does not contain a neutrino mass term; in recent years a plethora of evidence pointing to non-zero neutrino masses has been amounting through neutrino oscillation studies which are only possible if neutrinos do have finite mass. To attempt to explain these elements and unify all four of the fundamental forces Grand Unified Theories (GUTs) are being developed. Vital inputs to these theories can be provided by probing phenomena that are not predicted by the Standard Model and neutrinos have a vital role to play in driving these boundaries into the next paradigm of human understanding.

1.2 A brief history of the neutrino

1.2.1 Postulation

The existence of the neutrino was first proposed by Pauli in 1930 to explain the continuous electron energy spectrum observed in nuclear β^-decay [3]. At the time, β^-decay was understood to be the decay of a nucleus A into a lighter nucleus with the emission of an electron:

$$A(Z, N) \rightarrow A(Z + 1, N - 1) + e^- \tag{1.1}$$

Since the progeny nucleus is less massive than the parent nucleus, the energy of the electron should equal that difference owing to $E_{max} = \Delta mc^2$, where Δm is the difference in mass. However the electrons from the decaying nuclei were observed to emerge with a range of energies up to E_{max}. It seemed as if β^-decay violated the law of energy conservation. This led Pauli to account for this missing energy with a "desperate remedy", a postulation of the involvement of a third neutral particle that carried away the missing energy and angular momentum and escaped detection. It had to be electrically neutral (to conserve charge) and have spin 1/2 (to conserve angular momentum). Fermi worked out a detailed theory of β^-decay and the weak interaction and named Pauli's particle the neutrino, meaning "little neutral one". Bethe and Peierls [4] estimated a diminutive interaction cross section for neutrinos leading Pauli himself to fear he had predicted the existence of a particle that would never be detected.

1.2.2 Experimental Detection of Neutrinos

In 1953, Reines and Cowan succeeded in detecting anti-neutrinos from a nuclear reactor produced via the inverse β^-decay:

$$\overline{\nu}_e + p \rightarrow n + e^+ \tag{1.2}$$

The neutrinos were detected via the prompt photons produced by the annihilation of the positron with an electron in the water/cadmium chloride target followed by the delayed emission of photon created when the neutron is captured by a cadmium nucleus in the target [5].

In 1962 Lederman, Schwartz and Steinberger in an experiment with a high-energy proton beam at the new Alternating Gradient Synchrotron (AGS) in Brookhaven, USA, demonstrated that the neutrino associated with the muon and that with the electron were different and distinct particles [6]. This experiment also illustrated the validity of lepton-type conservation, thus explaining the absence of some otherwise expected decays.

The J/ψ particle, discovered in 1974, was interpreted as a bound quark-antiquark state of a new flavour of quarks known as charm [7], [8]. Now physicists could group the leptons and quarks into two generations and the

quark model seemed complete. Ordinary matter is composed of particles in the first family, and the second family is a repeat pattern of the first albeit heavier and more unstable. However in 1975 the tau lepton was discovered [9] signalling the possibility of a third family of particles. In 1976 evidence for the bottom quark was found at the Fermi National Accelerator Laboratory (FNAL) [10]; evidence for the top quark had to wait until 1995 when advances in accelerator and detection technology made it possible [11, 12].

The actuality of a tau neutrino followed naturally. Studies of tau lepton decays provided indirect evidence of ν_τ but it took until the year 2000 at the DONUT (Direct Observation of NU-Tau) experiment at Fermilab before the tau neutrino was conclusively identified by its charged current interaction:

$$\nu_\tau + N \rightarrow \tau^- + X \tag{1.3}$$

and by identifying the τ lepton as the only lepton created at the interaction vertex [13].

Neutrinos from other sources have also been observed. In 1968 neutrinos were observed from the Sun by Raymond Davis Jr. and his collaboration at the Homestake Mine experiment [14]. In 1987 neutrinos from the supernova explosion SN1987a were detected by the Kamiokande [15] and IMB [16] experiments. In 2002 Raymond Davis Jr. and Masatoshi Koshiba were awarded the Nobel Prize for their discovery of cosmic neutrinos.

1.3 Neutrino Mass Measurements

The finite mass of the neutrino is not predicted or explained in the Standard Model. Direct measurements of neutrino masses investigate the kinematics of weak decays. From the charged decay products of tritium, pions and tau neutrinos the missing neutrino mass is reconstructed from energy and momentum conservation. The current limits on the neutrino masses from such direct measurements are given in table 1.2.

An alternative way to generate neutrino mass is to abandon the fundamental distinction between matter and antimatter. Majorana neutrinos are their own anti-particles (possible for neutrinos as they are uncharged). In this scheme the neutrino and anti-neutrino are distinguished only by their helicity. Some nuclei are stable in normal β-decay (involving one weak interaction vertex) but can decay via a lepton number violating double weak interaction process with an extremely long lifetime via the process (A, Z) $\rightarrow$ (A, Z + 2) + e^- + e^-, The null results of these searches provide limits on the Majorana neutrino mass (see table 1.2).

Additionally cosmological data provide information on the total mass of light active neutrinos. A combined analysis of data from the Wilkinson Microwave Anisotropy Probe (WMAP) and the 2dF Galaxy Redshift Survey (2dFGRS) give limits on the sum of neutrino masses as stated in table 1.2.

Neutrino Type	Mass	Method
Electron	$m_{\nu_e} < 2.2$ eV (95% C.L.)	Tritium Beta Decay [17]
Electron	$m_{\nu_e} < 0.35$ eV (90% C.L.)	Neutrino-less Double β-Decay [18]
Muon	$m_{\nu_\mu} < 190$ keV (90% C.L.)	Two-body decay of Pion [19]
Tau	$m_{\nu_\tau} < 18.2$ MeV (90% C.L.)	Hadronic Tau Decays [20]
All	$\sum_{i=1}^{3} m_{\nu i} < 1.0$ eV (95% C.L.)	WMAP and 2dF galaxy survey [21]

Table 1.2: Current Limits on Neutrino Masses

1.4 Neutrino Oscillation

Neutrino oscillation is the phenomenon whereby neutrinos travelling over long distances at close to the speed of light mix between electron, muon and tau flavours. Over the past decade a plethora of evidence from observations of solar, atmospheric, reactor and long-baseline accelerator neutrinos has been amassing, implying non-zero neutrino masses.

Neutrino oscillations between neutrinos and anti-neutrinos were first postulated by Pontecorvo in 1957 [22]. By 1962 Z. Maki, M. Nakagawa and S. Sakata had formulated a theory for neutrino flavour oscillation [23] and in 1968 Pontecorvo also developed a theory of neutrino oscillations [24]. The first evidence for neutrino oscillations was not observed until Ray Davis Jr's solar neutrino experiment detected a deficit in the number of neutrinos observed compared to that expected from predictions by the standard solar model [14], [25].

1.4.1 Theory

Neutrinos are created and detected as weak eigenstates ν_α $(\nu_e, \nu_\mu, \nu_\tau)$ via weak interactions, but propagate as mass eigenstates ν_i (ν_1, ν_2, ν_3). Neutrino oscillations arise since the mass eigenstates are misaligned with the weak eigenstates. The weak eigenstates are a coherent superposition of mass eigenstates:

$$|\nu_\alpha\rangle = \sum_{i=1}^{3} U^*_{\alpha i} |\nu_i\rangle \tag{1.4}$$

where $|\nu_\alpha\rangle$ is a neutrino with definite flavour. $|\nu_i\rangle$ is a neutrino with definite mass and is represented by:

$$|\nu_i\rangle = \sum_{i=1}^{3} U_{\alpha i} |\nu_\alpha\rangle \tag{1.5}$$

U represents the unitary mixing matrix, called the Maki-Nakagawa-Sakata (MNS) matrix, or sometimes the PMNS matrix to include Pontecorvo. This matrix can be parameterised as follows:

$$U = \begin{pmatrix} c_{12}c_{13} & s_{12}c_{13} & s_{13}e^{-i\delta} \\ -s_{12}c_{23} - c_{12}s_{23}s_{13}e^{i\delta} & c_{12}c_{23} - s_{12}s_{23}s_{13}e^{i\delta} & s_{23}c_{13} \\ s_{12}s_{23} - c_{12}c_{23}s_{13}e^{i\delta} & -c_{12}s_{23} - s_{12}c_{23}s_{13}e^{i\delta} & c_{23}c_{13} \end{pmatrix} \quad (1.6)$$

This is often written as the product of three separate matrices:

$$\begin{pmatrix} 1 & 0 & 0 \\ 0 & c_{23} & s_{23} \\ 0 & -s_{23} & c_{23} \end{pmatrix} \begin{pmatrix} c_{13} & 0 & e^{-i\delta}s_{13} \\ 0 & 1 & 0 \\ -e^{+i\delta}s_{13} & 0 & c_{13} \end{pmatrix} \begin{pmatrix} c_{12} & s_{12} & 0 \\ -s_{12} & c_{12} & 0 \\ 0 & 0 & 1 \end{pmatrix} \quad (1.7)$$

where $c_{ij} = \cos\theta_{ij}$ and $s_{ij} = \sin\theta_{ij}$. The mixing angles θ_{ij} parameterise the three possible rotations between the neutrino states and δ is the CP-violating phase. Traditionally θ_{12} and Δm^2_{12} are known as the "solar" mixing parameters, concerned with $\nu_e \rightarrow \nu_x$ flavour oscillations and θ_{23} and Δm^2_{23} as the "atmospheric" mixing parameters describing $\nu_\mu \rightarrow \nu_\tau$ oscillations. The third component, θ_{13} and Δm^2_{13}, has not yet been measured. It describes, for example, $\nu_\mu \rightarrow \nu_e$ in a typical accelerator experiment.

If the ν_i possess differing masses they build up a relative phase difference. In the simplest case, two mass states dominate the oscillations. The probability for flavour oscillation in this case is:

$$P_{\nu_\alpha \rightarrow \nu_\beta} = \sin^2 2\theta \sin^2 \left(1.27 \frac{\Delta m^2}{E} L\right) \quad (1.8)$$

The survival oscillation probability is simply $P_{\nu_\alpha \rightarrow \nu_\alpha} = 1 - P_{\nu_\alpha \rightarrow \nu_\beta}$, that is:

$$P_{\nu_\alpha \rightarrow \nu_\alpha} = 1 - \sin^2 2\theta \sin^2 \left(1.27 \frac{\Delta m^2}{E} L\right) \quad (1.9)$$

Equation 1.9 illustrates that the oscillation probability modulates sinusoidally over the distance travelled, L (m) and is dependent upon the neutrino energy, E (MeV), the mixing angle and Δm^2 (eV^2), which is the mass squared difference between the two mixing ν_i states $\Delta m^2 = m_j^2 - m_i^2$. This equation is true in vacuum for all cases, is true in matter for $\nu_\mu \leftrightarrow \nu_\tau$, but may be modified for oscillations involving ν_e which can experience additional charge-current interactions due to electrons in matter, known as the MSW effect [26]. An example of the survival oscillation probability of muon neutrinos as a function of the neutrino energy is shown in figure 1.1.

Neutrino experiments apply equation 1.9 to calculate the oscillation parameters Δm^2 and $\sin^2 2\theta$ from measurements of the survival probability. This enables the experimenters to create a "map" of allowed parameter space from the results of the various experiments. Such "exclusion plots" exhibit the allowed and forbidden regions in the (Δm^2, $\sin^2 2\theta$ or $\tan^2\theta$) parameter

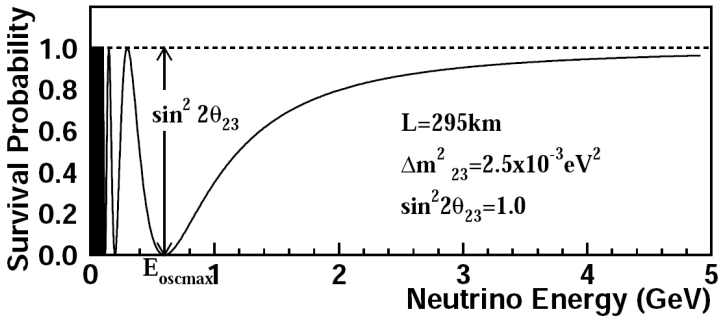

Figure 1.1: Survival probability of muon neutrinos as a function of the neutrino energy. The neutrino travel distance is 295km and oscillation parameters are assumed to be (Δm^2,$\sin^2 2\theta_{23}$) = (2.5×10^{-3} eV^2, 1.0) [27]

space. Experiments initially showed that there were four distinct regions of allowed parameter space for the mixing parameters which were called the "Vacuum Oscillation Solution" (VAC), "Small Mixing Angle Solution" (SMA), "Large Mixing Angle Solution" (LMA), and "Low Δm^2 Solution for Large Mixing Angle" (LOW). Initially the SMA solution was theoretically favoured since small mixing angles are observed in the mixing between quarks, however experimental evidence has gradually amassed towards an LMA solution.

1.5 Evidence for Neutrino Oscillation

Although the first firm evidence of neutrino oscillations came from an atmospheric neutrino experiment, the first neutrino oscillation experiments involved investigating neutrinos from the Sun. These experiments will be briefly reviewed here as well as subsequent experiments utilising nuclear reactors and conventional particle beams as sources of neutrinos.

1.5.1 Measurements of $\sin^2\theta_{12}$ and Δm^2_{12}

Solar Neutrinos

The first experiment to detect solar neutrinos used the isotope ^{37}Cl as a target in a 100,000 gallon tank of C_2Cl_4. Neutrino capture on the ^{37}Cl, with an energy threshold of 0.8 MeV, produces a radioactive isotope of argon which is captured and counted. The unforeseen result was that only a third of the expected number of neutrinos was actually observed. This discrepancy henceforth became known as the "Solar Neutrino Problem".

In the late 1980s this deficit was confirmed by the Kamiokande experiment in Japan [28]. Situated a kilometre underground it detected electron

neutrinos when they scattered elastically off an electron in the detector's 700 tonne volume of purified water, and imparted enough recoil energy to generate a cone of Cherenkov radiation which was detected by a thousand 50 cm photomultiplier tubes. They were the first to directly verify that the detected neutrinos did come from the direction of the sun [29]. Sensitive to the flux of ^{8}B neutrinos ($^8\mathrm{B} \rightarrow 2^4\mathrm{He} + e^+ + \nu_e$) they detected 49% to 64% of what was predicted in the Standard Solar Model [30].

In order to detect the lower energy and more abundant pp chain neutrinos ($p + p \rightarrow {}^2\mathrm{H} + e^+ + \nu_e$) two gallium-based radiochemical detectors were developed in the early 1990s, the Soviet-American Gallium Experiment (SAGE) [31] and the Italo-German GALLium EXperiment (GALLEX) [32]. followed by the Gallium Neutrino Observatory (GNO) [33] also in Gran Sasso. The results of these experiments are shown in table 1.3.

Experiment	Measured Rate/Flux	SSM Prediction
Homestake (^{37}Cl)	$2.56 \pm 0.16 \pm 0.16$ SNU	$7.6^{+1.3}_{-1.1}$ SNU
SAGE (^{71}Ga)	$70.8^{+5.3+3.7}_{-5.2-3.2}$ SNU	
Gallex (^{71}Ga)	$77.5 \pm 6.2^{+4.3}_{-4.7}$ SNU	128^{+9}_{-7} SNU
GNO (^{71}Ga)	$62.9^{+5.5}_{-5.3} \pm 2.5$ SNU	
Kamiokande (ν_e)	$2.80 \pm 0.19 \pm 0.33$	$5.05(1^{+0.20}_{-0.16})$
Super-Kamiokande (ν_e)	$2.32 \pm 0.03^{+0.08}_{-0.07}$	

Table 1.3: Summary of solar neutrino observations at different terrestrial detectors before 2002. The Bahcall-Pinsonneault (BP2001) model predictions of the solar neutrino flux are presented in this table [34]. The experimental values are shown with statistical uncertainties listed first, followed by systematic uncertainties. The Solar Neutrino Unit (SNU) is a measure of solar neutrino interaction rate, and is defined as 1 interaction per 10^{-36} target atom per second. For the Kamiokande and Super-Kamiokande experiments the predicted and measured neutrino fluxes are given in units of 10^6 cm^{-2} s^{-1}. Adapted from [35].

The Solar Neutrino Problem was essentially solved with the advent of the Sudbury Neutrino Observatory (SNO) [36], built specifically to test the hypothesis of neutrino flavour change by measuring not only the electron type neutrino flux, but also the flux of all active neutrino flavours from the Sun. Located in Sudbury, Canada, it is a kilotonne heavy water Čerenkov detector, situated over 2km underground giving it a remarkably low cosmic ray background rate.

SNO detects neutrinos from ^{8}B decays in the Sun through three reactions: charged current ($\nu_e + d \rightarrow p + p + e^-$), elastic scattering ($\nu_x + e^- \rightarrow \nu_x + e^-$) and neutral current ($\nu_x + d \rightarrow \nu_x + p + n$) where $x = e,\ \mu,\ \tau$. The

elastic scattering reaction has some sensitivity to non-electron flavours, but is primarily sensitive to electron neutrinos. The neutral current reaction allows a measurement of the total flux of all active ^{8}B solar neutrinos, while a comparison of the neutrino fluxes measured through the neutral current and charged current reactions tests for solar neutrino flavour change.

The SNO collaboration published two measurements of solar neutrino flux from the first phase of the experiment in which pure D_2O was used as a target. In June 2001 the SNO collaboration reported their first results [37]. The flux of electron neutrinos from ^{8}B decay measured by the CC reaction rate was

$$\phi^{CC}(\nu_e) = 1.75 \pm 0.07(\text{stat.})^{+0.12}_{-0.11}(\text{sys.}) \pm 0.05(\text{theor.}) \times 10^6 \text{cm}^{-2}\text{s}^{-1} \quad (1.10)$$

This result was compared to the high statistics flux measurement of elastic scattering events $\phi^{SK}_{ES}(\nu_x)$ in Super Kamiokande, a larger and improved version of the Kamiokande water Čerenkov experiment. The 3.3σ difference in these two results provided the first evidence of an active non-electron flavour component in the solar neutrino flux. The total flux of active ^{8}B neutrinos was found to be in extremely close agreement with the predictions of solar models.

Observations of NC interactions on deuterium were also found to be consistent with solar models [38] and provided strong evidence for solar ν_e flavour transformation. Figure 1.2 shows the flux of non-electron flavour active neutrinos versus the flux of electron neutrinos deduced from the SNO data. The bands show the fluxes of neutrinos as predicted by the SSM and measured by the SNO NC, CC and ES reactions.

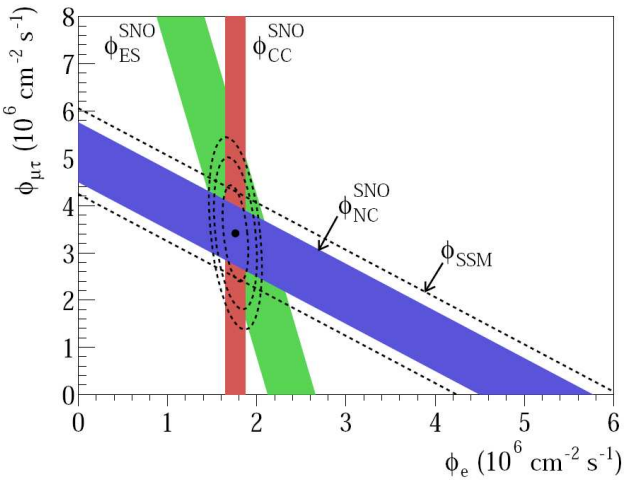

Figure 1.2: Flux of ^{8}B solar ν_μ or ν_τ vs flux of ν_e deduced from three neutrino reactions in SNO [38]. The diagonal bands show the total ^{8}B flux as predicted by the SSM [34] (dashed lines) and that measured with the NC reaction in SNO (solid band)

For the second phase of the SNO experiment an additional 2 tonnes of NaCl was added to the tank of heavy water to increase the neutron capture efficiency for the NC reaction [39, 40]. The results confirmed the prediction of the SSM total neutrino flux and are consistent with those expected for neutrino oscillations with the so-called Large Mixing Angle (LMA) parameters [41].

The third phase of SNO added an array of ^{3}He proportional counters (Neutral-Current Detectors), to detect the neutron liberated from the NC break-up of the deuteron. These NCD results agree well with the previous SNO phase results, using an independent method to the other results and reducing the uncertainty on the mixing angle measurement [42].

Reactor Neutrinos

After consistent deficits of the solar neutrino flux from solar neutrino experiments were observed, experiments were designed to investigate the flux of neutrinos from nuclear power reactors thus probing neutrino oscillations under "laboratory conditions" i.e. the incoming neutrino flux from the nuclear reactor would be very well known, in contrast to the hypothesised flux of neutrinos from the Sun. Experimenters hoped to be able to detect a variation of the observed flux and spectrum of the neutrinos with distance, known as the disappearance method.

At the Bugey nuclear power plant in France anti-electron neutrinos were detected by the charged-current interaction $\overline{\nu}_e + p \rightarrow e^+ + n$ and oscillations searched for at 15, 40 and 95 m from the reactor [43]. No oscillations were discovered. Similarly experiments at Gosgen in Switzerland [44] and Krasnoyarsk [45] and Rovno [46] in Russia all observed the expected neutrino fluxes within experimental errors. These experiments were built within 100 m of the reactors to ensure a high flux of neutrinos to allow maximum detection potential. Considering neutrinos have such an insignificant interaction cross section experimenters were concerned with achieving an appreciable neutrino signal.

The CHOOZ experiment in France took data between 1996 and 1998 [47] and Palo Verde in the USA from 1998 to 2000 [48]. These were larger experiments situated 1 km from the reactors. Although no evidence for neutrino oscillations was found, limits were set on the allowed values of parameter space due to a non-signal.

The Kamioka Liquid scintillator Anti-Neutrino Detector (KamLAND) was built to search for the oscillation of anti-electron neutrinos emitted from over 60 distant power reactors in Japan and Korea [49]. The neutrino detector/target is 1 kilotonne of ultra-pure liquid scintillator contained in a 13 m diameter spherical balloon that is suspended in mineral oil and viewed by 1879 photomultiplier tubes. A 3.2 kilotonne water Čerenkov detector surrounds the containment sphere and absorbs γ-rays and neutrons from the enclosing rock and tags cosmic ray muons. Neutrinos with energies over the

1.8 MeV threshold are detected via $\overline{\nu}_e + p \rightarrow e^+ + n$. The emitted positron promptly annihilates with an electron producing 2 γ rays. The neutron is thermalised by mineral oil and captured by a proton in a hydrogen or carbon atom via $n + p \rightarrow d + \gamma$. The $\sim$ 200 μs delayed 2.2 MeV γ-ray from this neutron capture is a powerful tool for reducing backgrounds.

Figure 1.3 shows the ratio of measured to expected fluxes as a function of the average distance from the source for KamLAND and previous reactor experiments. This plot clearly illustrates why the earlier reactor experiments

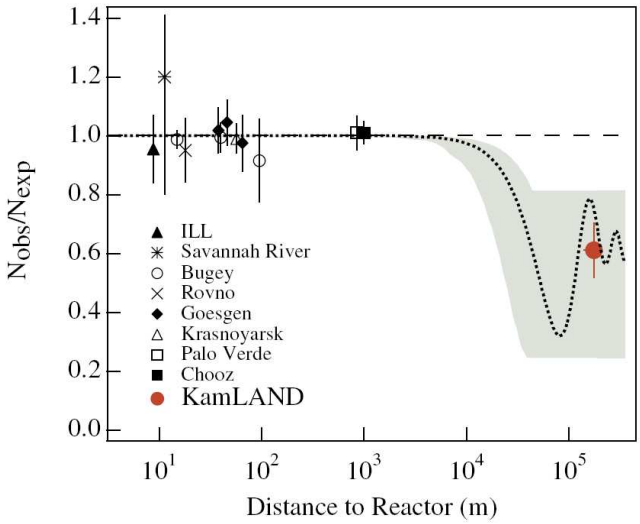

Figure 1.3: The ratio of measured to expected $\overline{\nu}_e$ flux from reactor experiments [49].

could not detect any neutrino oscillations. The dotted curve corresponds to values of $\sin^2 2\theta$ and Δm^2 for LMA solutions, and the dashed curve shows the case of small mixing angles or no oscillation. The shaded region corresponds to the 95% C.L. LMA region according to analysis of solar neutrino data.

KamLAND observed the first reactor anti-neutrino disappearance in 2003. The average $\overline{\nu}_e$ survival probability is:

$$\frac{N_{obs} - N_{BG}}{N_{expected}} = 0.658 \pm 0.044(stat.) \pm 0.047(syst.) \qquad (1.11)$$

It confirmed anti-neutrino disappearance at 99.998% C.L. and very tightly constrained the global solar LMA solution.

To illustrate the oscillatory behaviour of the data the ratio of the observed anti-neutrino spectrum to the expectation for no oscillation is plotted against L_0/E as shown in figure 1.4. All the data points and models are plotted with $L_0 = 180$ km and as if all anti-neutrinos detected in KamLAND were due to a single reactor at this distance. Figure 1.4 illustrates that the expectation for the best-fit oscillation has a much better agreement with the data when

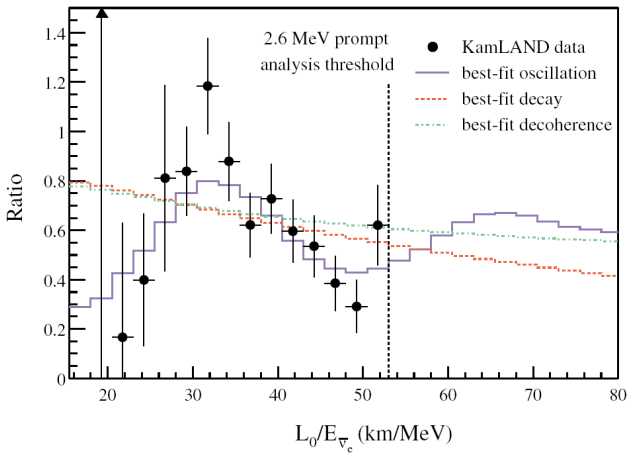

Figure 1.4: Ratio of the observed anti-neutrino spectrum to the expectation for no oscillation versus L_0/E. The curves illustrate the expectation for the best-fit oscillation, best-fit decay and best-fit decoherence models taking into consideration the individual time-dependent flux variations of all reactors and detector effects [50].

compared to two alternative hypotheses for neutrino disappearance (neutrino decay [51] and decoherence [52]).

A global analysis of solar and reactor neutrino results yields [42]

$$\Delta m^2_{12} = 7.59^{+0.19}_{-0.21} \times 10^{-5}\text{eV}^2 \tag{1.12}$$

$$\sin^2 2\theta_{12} = 0.87 \pm 0.03 \tag{1.13}$$

Figure 1.5 illustrates how the parameters θ_{12} and Δm^2_{12} as stated in table 1.4 are determined from the combined solar and reactor neutrino sources.

1.5.2 Measurements of $\sin^2\theta_{23}$ and $|\Delta m^2_{23}|$

Atmospheric Neutrinos

In 1998 the Super-Kamiokande collaboration reported the first firm evidence of neutrino oscillations from observations of atmospheric neutrinos [54]. Atmospheric neutrinos are created by the interaction of cosmic rays (primarily protons and helium) with the air nuclei in the upper atmosphere which create hadronic showers consisting mostly of pions ($\pi^{\pm}$) . These pions decay into muons and muon neutrinos via $\pi^+ \rightarrow \mu^+ + \nu_\mu$ and $\pi^- \rightarrow \mu^- + \overline{\nu}_\mu$. The muons further decay into electrons and electron-neutrinos via $\mu^+ \rightarrow e^+ + \nu_e + \overline{\nu}_\mu$ and $\mu^- \rightarrow e^- + \overline{\nu}_e + \nu_\mu$. The flavour ratio of muon to electron neutrinos from

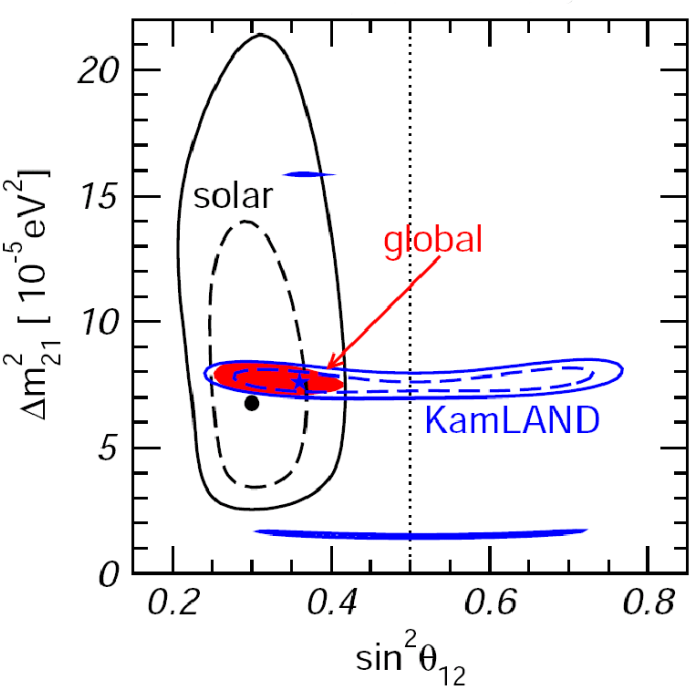

Figure 1.5: Determination of oscillation parameters from solar and reactor neutrino sources [53]

these cosmic ray showers is defined as:

$$\frac{N_\mu}{N_e} = \frac{(\nu_\mu + \overline{\nu}_\mu)}{(\nu_e + \overline{\nu}_e)} \tag{1.14}$$

and can be estimated with confidence to be close to 2 [55].

The first two atmospheric neutrino oscillation experiments were water Čerenkov experiments, Irvine-Michigan-Brookhaven (IMB) [56] and Kamiokande [57, 58]. The experiments measured the double ratio R of the observed flavour ratio (N_{Data}) to the expected ratio (N_{MC}), which largely cancels out experimental and theoretical uncertainties. The double ratio R is defined as:

$$R\left(\frac{\mu}{e}\right) = \frac{(N_\mu/N_e)_{Data}}{(N_\mu/N_e)_{MC}} \tag{1.15}$$

If $R = 1$ the physics in the Monte Carlo simulation accurately models the data. Both experiments measured a value of R that was much less than unity and found the measured flavour ratio different from two. Unable to explain the data as a result of systematic detector effects or uncertainties in the atmospheric neutrino fluxes, they postulated that neutrino oscillations of $\nu_\mu \leftrightarrow \nu_\tau$ might account for the observations.

The successor experiment, Super-Kamiokande (SK) [59], with ten times

the volume and twice the density of PMTs of Kamiokande, also measured R less than unity. Furthermore, SK measured a zenith angle dependence of R i.e. the number of upward-going muon neutrinos, which had travelled through the entire Earth to reach the SK detector, was smaller than the number of downward-going muon neutrinos, which had only travelled from the upper atmosphere to the underground detector. The zenith angle distributions with the best fit for $\nu_\mu \rightarrow \nu_\tau$ oscillations are shown in figure 1.6. R

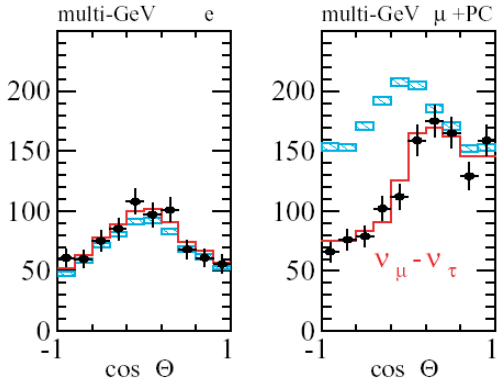

Figure 1.6: Zenith angle distribution for the atmospheric neutrinos used in SK oscillation analysis [54]. The cosine of a zenith angle, $\cos\theta = -1$ corresponds to the upward-going direction, $\cos\theta = 0$ to the horizontal direction and $\cos\theta = +1$ to the downward-going direction. The hatched region shows the Monte Carlo expectation for no oscillations and the bold line is the best-fit expectation for $\nu_\mu \rightarrow \nu_\tau$ oscillations.

was determined to be [60]:

$$R = 0.688 \pm 0.016\ (stat.) \pm 0.004\ (sys.) \tag{1.16}$$

The zenith angle distribution of $\mu-$like events and the value of R in this experiment significantly differ from the best predictions in the absence of neutrino flavour oscillations.

The most recent results from SK provide evidence of an oscillatory signature in atmospheric neutrino oscillations [61]. By plotting the number of atmospheric neutrino events observed in SK as a function of L/E for the data and MC predictions, a dip is observed which corresponds to the first maximum oscillation. This is illustrated in figure 1.7. This strongly constrains the allowed $\nu_\mu \leftrightarrow \nu_\tau$ oscillation parameter regions to:

$$1.9 \times 10^{-3} < \Delta m^2_{23} < 3.0 \times 10^{-3}\text{eV}^2 \tag{1.17}$$

$$\sin^2 2\theta_{23} > 0.90 \tag{1.18}$$

at the 90% C.L. Additionally, since alternative models that can explain the

zenith angle and energy dependent deficit of the atmospheric ν_μ do not predict a dip in the L/E distribution, they are disfavoured. This was the first direct evidence that the neutrino survival probability obeys the sinusoidal function predicted by neutrino oscillations.

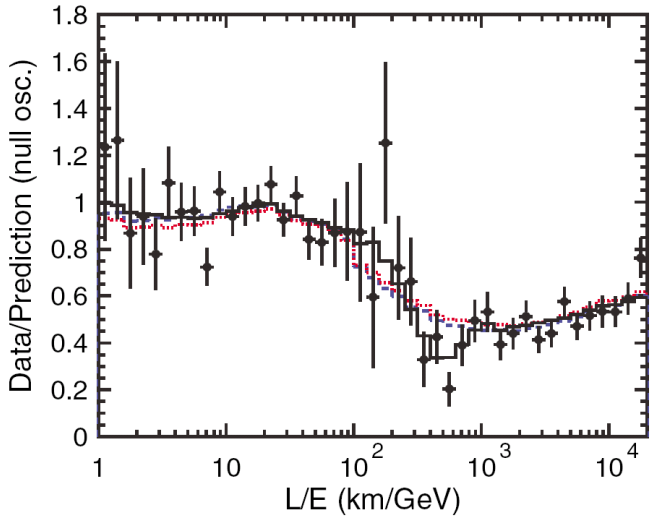

Figure 1.7: Ratio of data to MC events without neutrino oscillation (points) as a function of the reconstructed L/E and the best-fit expectation for 2-flavour $\nu_\mu \rightarrow \nu_\tau$ oscillations (solid line). Also shown are the best-fit expectation for neutrino decay (dashed line) and neutrino decoherence (dotted line) [61].

SK has also observed the signal of ν_τ appearance at 2.4σ [62]. The ν_τ excess has been observed in the upward-going direction as expected. The result is consistent with $\nu_\mu \rightarrow \nu_\tau$ oscillations.

Long Baseline Accelerator Neutrinos

Long baseline accelerator experiments were designed to confirm the observations of atmospheric neutrino oscillations with the use of accelerator-produced neutrinos, thereby with a fixed, well-known neutrino flight length.

KEK to Kamioka (K2K) was the first long baseline neutrino oscillation experiment [63]. Neutrinos were produced using a 12 GeV proton beam produced at KEK, the Japanese National High Energy Accelerator Laboratory in Tsukuba, Japan and fired at SK 250 km distant. Since the distance between the neutrino source (KEK) and detection (SK) is fixed, the probability of oscillations is energy dependent. Data taking from 1999 to 2004 revealed 112 beam-originated neutrino events in SK compared to an expectation of $158.1^{+9.2}_{-8.6}$ events without oscillation. A distortion of the energy spectrum was also observed, leading to the conclusion that the results are consistent with neutrino oscillations.

The Main Injector Neutrino Oscillation Search (MINOS) produces neutrinos using a 120 GeV proton beam at Fermilab, which are fired to a far detector 735 km distant. Recent MINOS results reveal 563 charged-current ν_μ interaction candidates compared to 738 $\pm$ 30 events expected in the absence of neutrino oscillations [64]. Figure 1.8 shows the reconstructed neutrino charged current energy spectrum. A clear deficit of events is observed at the dip position around 1.5 to 2 GeV allowing Δm^2_{23} to be measured accurately and the sinusoidal dependence of the probability is observed as expected in the neutrino oscillation hypothesis. The oscillation fit results are

$$|\Delta m^2_{23}| = (2.38^{+0.20}_{-0.16}) \times 10^{-3}\text{eV}^2 \text{ (68\% C.L.)} \tag{1.19}$$

and

$$\sin^2 2\theta_{23} > 0.84 \text{ (90\% C.L.)} \tag{1.20}$$

with errors at 68% confidence level for neutrino squared-mass difference and 90% confidence level for mixing angle.

Figure 1.9 shows the estimated allowed regions of $\nu_\mu \rightarrow \nu_\tau$ oscillation parameters from the atmospheric and long baseline neutrino oscillation experiments [53].

1.5.3 Measurements of $\sin^2\theta_{13}$

Only an upper limit on the third mixing angle θ_{13} is known. The CHOOZ experiment, which searched for $\overline{\nu}_e$ disappearance in reactor $\overline{\nu}_e$ flux, set the best limit to date on the mixing angle $\sin^2 2\theta_{13} < 0.17$ due to a non-signal [65].

SK and K2K experiments have also searched for $\nu_\mu \rightarrow \nu_e$ oscillations. In SK the signature of non-zero θ_{13} would be a matter-enhanced excess of upward-going electron-like events; no evidence for this was found [66]. The K2K experiment searched for ν_e appearance in a beam of ν_μ but found only a single electron candidate, consistent with background expectation [67]. Figure 1.10 shows the constraints set on θ_{13} from global data.

1.5.4 LSND and MiniBooNE Results

Another indication for neutrino oscillation was found by the Liquid Scintillator Neutrino Detector (LSND) experiment [68] which reported neutrino oscillations from $\overline{\nu}_\mu \rightarrow \overline{\nu}_e$ at the $\Delta m^2 \approx 1\text{eV}^2$ mass scale. This, together with the mass scales determined by the solar/reactor and atmospheric/accelerator experiments, cannot be accommodated in an extension of the Standard Model with three neutrino mass eigenstates and requires the addition of one or more sterile neutrinos or other extensions of the Standard Model (e.g. [69], [70]).

The MiniBooNE experiment, designed to confirm or refute this oscillation evidence, presented its first results in 2007 [71]. MiniBooNE searched for $\nu_\mu \rightarrow \nu_e$ appearance with a very similar L/E_ν range to LSND. The MiniBooNE collaboration report no evidence for oscillations. The exclusion con-

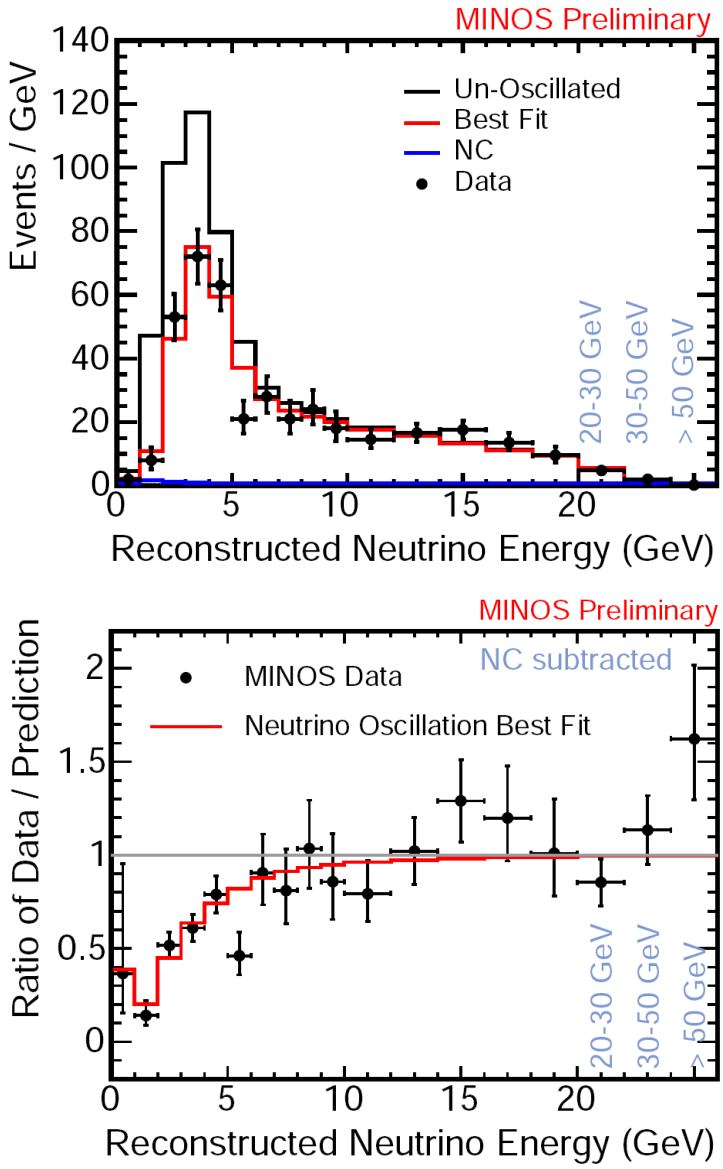

Figure 1.8: Top: Reconstructed neutrino charged current energy spectrum, black line shows predicted spectrum for no oscillation and red line predicted spectrum for $\nu_\mu \rightarrow \nu_\tau$ oscillations. Blue line shows the expected NC background contribution. Bottom: Ratio of the NC-background subtracted spectrum to the null-oscillation prediction (points), with the best-fit oscillation expectation overlaid (red) [64].

tour from MiniBooNE is shown in figure 1.11 in comparison to the LSND allowed region and the previous bound from the KARMEN experiment [72], in the framework of 2 flavour oscillations. They did however find a low-energy excess of data above background in neutrino mode (not in anti-neutrino mode) [74] its source is still under investigation.

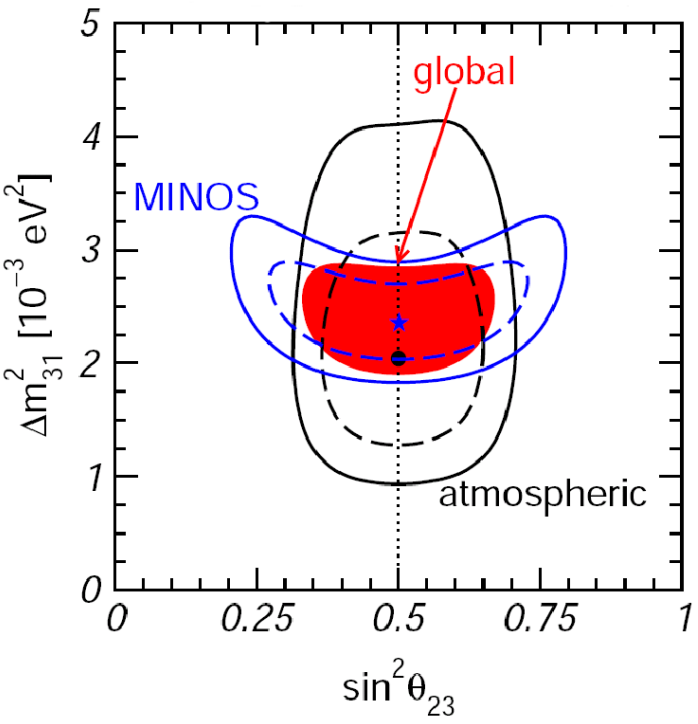

Figure 1.9: Determination of oscillation parameters from atmospheric and long baseline accelerator neutrino sources [53]

1.5.5 Neutrino Oscillation Parameters - Summary

The allowed values for the mass-squared differences Δm^2_{ij} and the mixing angles θ_{ij} at the 3σ level for three generations of neutrinos are summarised in table 1.4 [53]. Solar and long baseline reactor neutrino experiments have measured $\sin^2\theta_{12}$ and Δm^2_{12} and atmospheric and long baseline accelerator neutrino experiments have measured $\sin^2\theta_{23}$ and $|\Delta m^2_{23}|$. Only an upper limit on $\sin^2\theta_{13}$ is known, from a short baseline reactor experiment.

1.6 Conclusions

There are six mixing parameters associated with neutrino oscillation. $|\Delta m^2_{23}|$ and $\sin^2 2\theta_{23}$ have been measured via atmospheric and accelerator experiments and Δm^2_{12} and $\sin^2 2\theta_{12}$ via solar and reactor experiments. The sign of Δm^2_{23} and $\sin^2 2\theta_{13}$ are still unknown and determining these parameters is the aim of the next generation of neutrino oscillation experiments, with the measurement of the CP-violating phase δ as a major long-term goal.

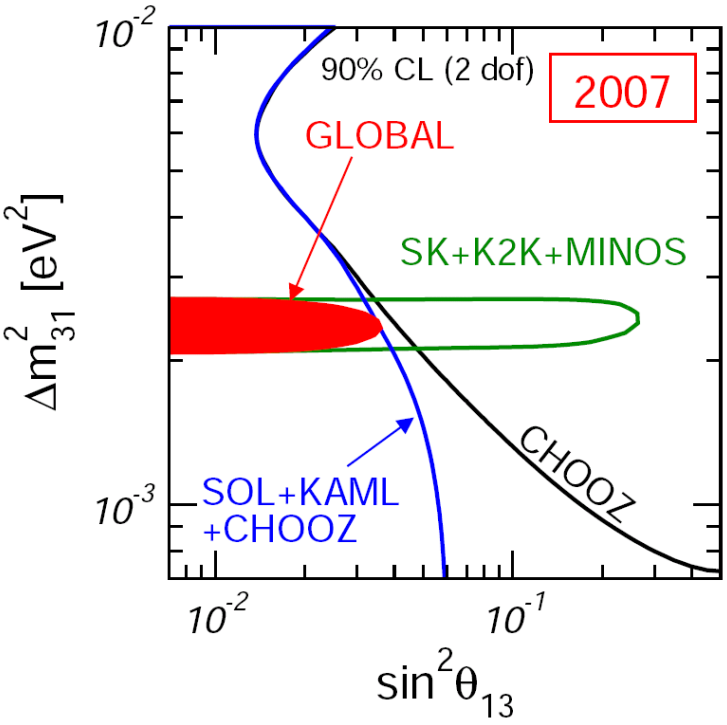

Figure 1.10: Constraints on θ_{13} from the global analysis of neutrino data [53]

Parameter	3σ values
Δm^2_{12}	(7.1 - 8.3) $\times 10^{-5}$eV^2
$\lvert\Delta m^2_{23}\rvert$	(2.0 - 2.8) $\times 10^{-3}$eV^2
$\sin^2\theta_{12}$	0.26 - 0.40
$\sin^2\theta_{23}$	0.34 - 0.67
$\sin^2\theta_{13}$	$\leq$ 0.050

Table 1.4: Values of the three-flavour neutrino oscillation parameters from global data including solar, atmospheric, reactor (KamLAND and CHOOZ) and accelerator (K2K and MINOS) experiments. Adapted from [53].

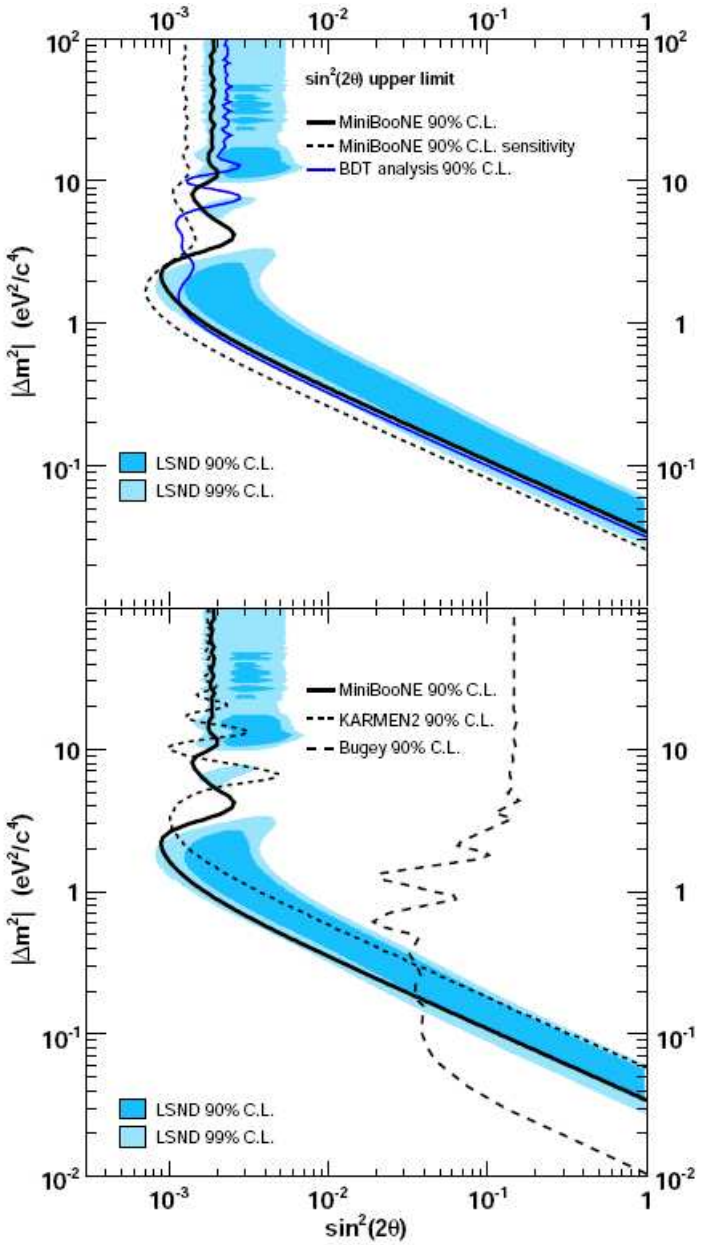

Figure 1.11: The top plot shows the MiniBooNE 90% CL limit (thick solid curve) and sensitivity (dashed curve) for events with reconstructed neutrino energy between 475 MeV and 3000 MeV within a two neutrino oscillation model. The bottom plot shows the limits from the KARMEN [72] and Bugey [73] experiments. The shaded areas show the 90% and 99% CL allowed regions from the LSND experiment [71].

Chapter 2

The T2K Experiment

2.1 Introduction

The T2K experiment is a second generation long baseline neutrino oscillation experiment that will probe physics beyond the Standard Model by high precision measurements of some of the parameters of neutrino oscillations. By firing an off-axis muon neutrino beam between the Japan Proton Accelerator Research Complex (JPARC) [75] and the Super-Kamiokande detector [59] 295 km distant, ν_e appearance in a ν_μ beam can be observed for the first time, allowing a sensitive measurement of the unknown mixing angle θ_{13}. The parameters $\sin^2 2\theta_{23}$ and Δm^2_{23} will also be measured more accurately than in any previous experiment. This chapter will describe the T2K experiment, including a description of the near detectors located at 280 m from the neutrino production target (ND280), where the UK effort is focused. The water-based scintillators that are the topic of this thesis are a potential upgrade to the passive water layers contained within some of these sub-detectors.

2.2 Aims of the T2K Experiment

The physics goals of the first phase of the T2K experiment are an order of magnitude improvement on the precision of the $\nu_\mu \rightarrow \nu_\tau$ oscillation measurements, a factor of 20 more sensitive search in the $\nu_\mu \rightarrow \nu_e$ appearance and a confirmation of the $\nu_\mu \rightarrow \nu_\tau$ oscillation or discovery of sterile neutrinos. In the second phase of the experiment (after an upgrade of the accelerator and far detector) the goals are another order of magnitude improvement in the $\nu_\mu \rightarrow \nu_e$ oscillation sensitivity and a sensitive search for CP violation in the lepton sector [75].

2.2.1 ν_μ Disappearance Measurement

The neutrino oscillation parameters $\sin^2 2\theta_{23}$ and Δm^2_{23} will be determined by measuring the survival probability of ν_μ after travelling from the JPARC facility in Tokai, Japan, to Super-Kamiokande 295 km to the west (full details of the experimental setup will be given in section 2.3). The ratio between the measured spectrum at Super-Kamiokande and that expected without oscillations will be determined. The reconstructed neutrino energy distribution and the ratio of the prediction with the best-fit oscillation parameters ($\sin^2 2\theta_{23}$=1.0 and $\Delta m^2 = 2.7 \times 10^{-3} eV^2$), to the prediction without oscillations is shown in figure 2.1. The oscillation pattern can be clearly seen. The

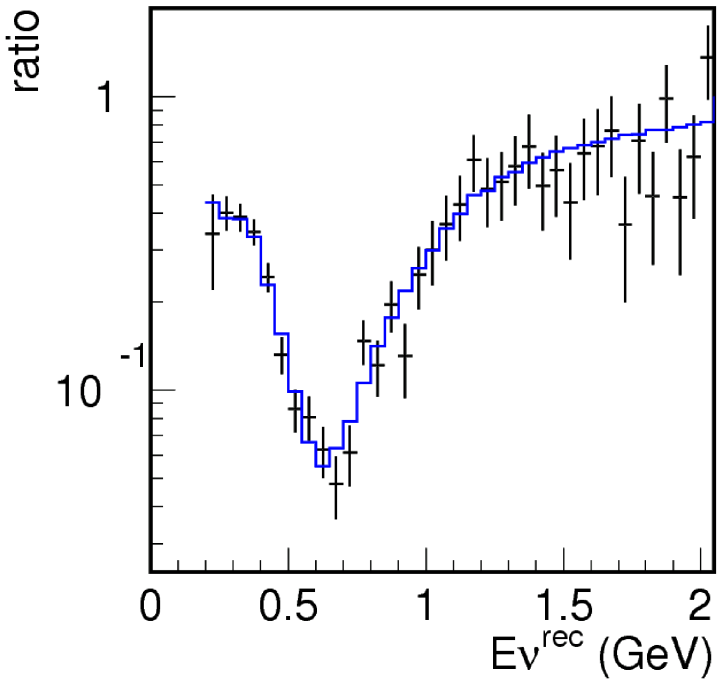

Figure 2.1: Ratio of measured spectrum with neutrino oscillation to expected spectrum without neutrino oscillation. The fit result of the oscillation is overlaid [76]. The off-axis angle is 2.5° with total of 5 $\times 10^{21}$ protons on target

depth of the disappearance signal dip corresponds to $1 - \sin^2 2\theta_{23}$ and its position gives Δm^2_{23}. The overall sensitivity is expected to be 1% in precision for $\sin^2 2\theta_{23}$ and better than 5×10^{-5}eV^2 for Δm^2_{23}.

2.2.2 ν_e Appearance Measurement

If $\nu_\mu \rightarrow \nu_e$ is observed in the first stage of the experiment it will prove in the first instance that $\theta_{13} \neq 0$. The neutrino beam will have a small ν_e contamination so the ν_e appearance signal is enhanced by tuning the neutrino energy at its expected oscillation maximum. The expected neutrino energy

resolution is sufficient to observe the oscillation pattern, as shown by the "dip" in figure 2.1, and hence confirm the ν_e appearance signal.

The ν_e appearance signal will be searched for in the charged current quasi-elastic (CCQE) interaction ($\nu_e + n \rightarrow e^- + p$). In this interaction the proton's energy is usually below the Cherenkov threshold so the signal is a single electromagnetic shower. The main source of background to the CCQE signal arises from neutral current single pion events and charged current single pion events. illustrated in figure 2.2. Understanding pion production will be vital to understand the background processes. Other possible background factors are e/μ misidentification, beam ν_e contamination and π^0 background. However the background from μ misidentification is negligible due to excellent e/μ separation at Super-Kamiokande and the ν_e contamination is as small as 0.2 - 0.3% [77]. A π^0 produced by neutral current and inelastic charged current processes is a possible background when one of the decay photons is missed or 2 photons overlap.

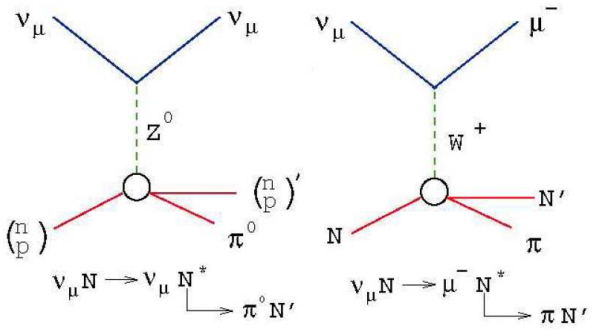

Figure 2.2: Feynman diagrams of a neutral current single pion event (left) and a charged current single pion event (right)

Figure 2.3 shows the reconstructed neutrino energy spectrum assuming $\sin^2 2\theta_{13} = 0.05$, $\Delta m^2_{13} = 0.003$ eV^2 and $\sin^2 2\theta_{23} = 1$. A clear appearance peak is seen at the oscillation maximum of $E_\nu = 0.75$ GeV. A sensitivity of $\sin^2 2\theta_{13} \leq 0.006$ at the 90% confidence level can be achieved.

2.2.3 $\nu_\mu \rightarrow \nu_\tau$ oscillation and search for sterile neutrinos

Sterile neutrinos ($\nu_{sterile}$) are a postulated fourth low-mass neutrino, which mixes with the standard neutrino flavours, but is sterile with respect to electroweak interactions.

Neutral current events are the sum of $\nu_\mu \rightarrow \nu_e, \nu_\mu$ and ν_τ oscillations, meaning that a neutral current measurement at Super-Kamiokande in association with $\nu_\mu \rightarrow \nu_e$ and $\nu_\mu \rightarrow \nu_\mu$ will allow an indirect measurement of $\nu_\mu \rightarrow \nu_\tau$. It also provides a constraint on the existence of the sterile neu-

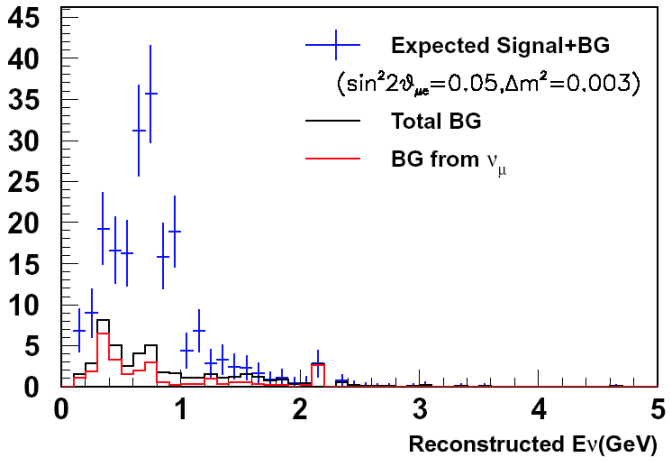

Figure 2.3: Expected reconstructed electron-neutrino energy distributions of expected signal plus background (BG), total BG and BG for ν_μ interactions for 5 $\times 10^{21}$ protons on target [76]

trino since the $\nu_\mu \rightarrow \nu_{sterile}$ oscillation causes a reduction of neutral current interactions.

The sensitivity to the fraction of $\nu_{sterile}$ in $\nu_\mu \rightarrow \nu_\tau$ oscillation is shown in figure 2.4 as a function of Δm^2 and $\sin^2 2\theta_{sterile}$. The best limit, $sin^2 2\theta_{sterile} \leq$

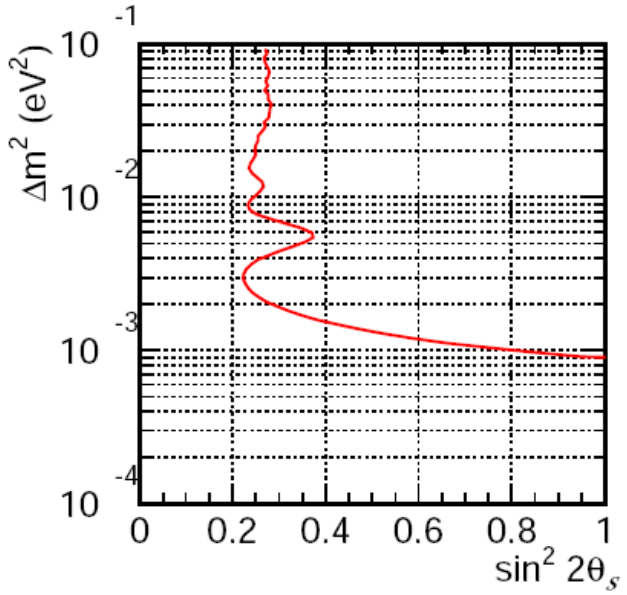

Figure 2.4: Sensitivity to the fraction of $\nu_{sterile}$ in $\nu_\mu \rightarrow \nu_\tau$ oscillation as a function of Δm^2 and $sin^2 2\theta_{sterile}$ with 5 $\times 10^{21}$ protons on target [77]

0.2 is obtained for $\Delta m^2 \approx 3 \times 10^{-3}$ eV^2. It is worth pointing out that these Conceptual Design Report calculations were carried out in 2005, using the then accepted limits; small changes in Δm^2 will not effect the overall conclusions.

2.2.4 Future Extension: CP Violation

In the second phase of T2K, after upgrades to the beam intensity and the fiducial volume of Super-Kamiokande, the statistics will increase by more than a factor of 100 [76]. This will increase sensitivity to $\sin^2 2\theta_{13}$ to below 10^{-3} and allow a measurement of the CP phase δ down to 10 - 20°. The CP asymmetry is illustrated in figure 2.5; with certain beam specifications it can become as large as 25%.

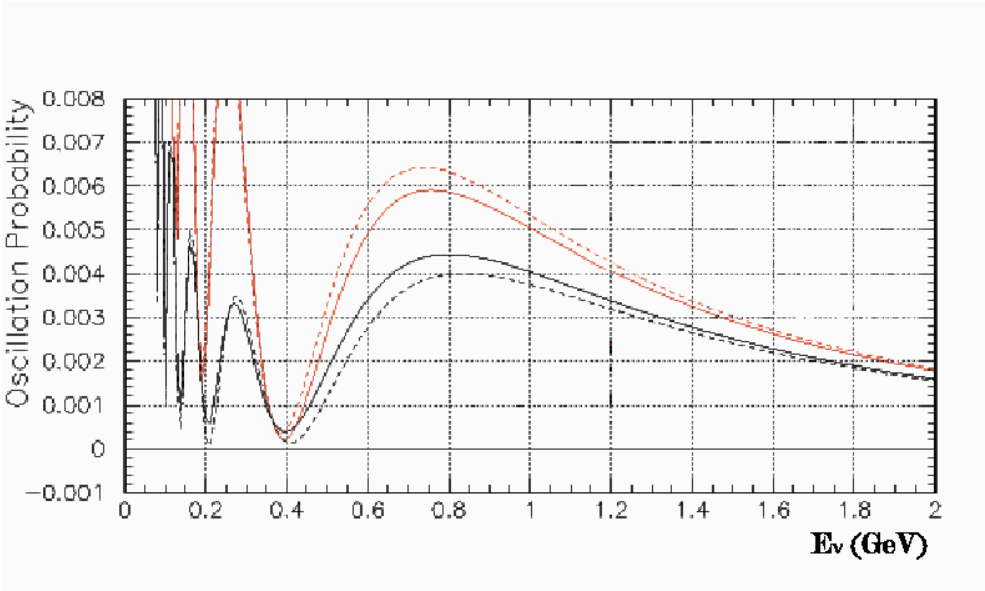

Figure 2.5: Oscillation probabilities for $\nu_\mu \rightarrow \nu_e$ (black curves) and $\overline{\nu}_\mu \rightarrow \overline{\nu}_e$ (red curves). The solid curves indicate an asymmetry due to matter effects. The difference between the dashed curves, with matter effects subtracted, are caused by the CP effect. The input parameters are E = 0.75 GeV, L = 295 km, ρ = 2.8 g/cm^2, $\sin^2 2\theta_{12} = 0.91$, $\Delta m^2_{12} = 6.9 \times 10^{-5}$ eV^2 (KamLAND best fit values at the time this graph was created), $\sin^2 2\theta_{13} = 0.01$ and $\delta = \frac{\pi}{4}$ [76]

2.3 T2K Experimental Overview

2.3.1 Tokai to Kamioka

An intense ν_μ beam will be created at the JPARC Proton Synchrotron facility at the Japan Atomic Energy Agency in the village of Tokai on the east coast

of Japan, about 110 km north-east of Tokyo. A near detector at 280 m will characterise the intensity, direction and composition of the beam, which will be aimed at the Super-Kamiokande detector 295 km away. Comparison between signals at the near and far detectors will indicate the presence of neutrino oscillations and probe the oscillation parameters.

A diagram of the JPARC facility is illustrated in figure 2.6. The schematic

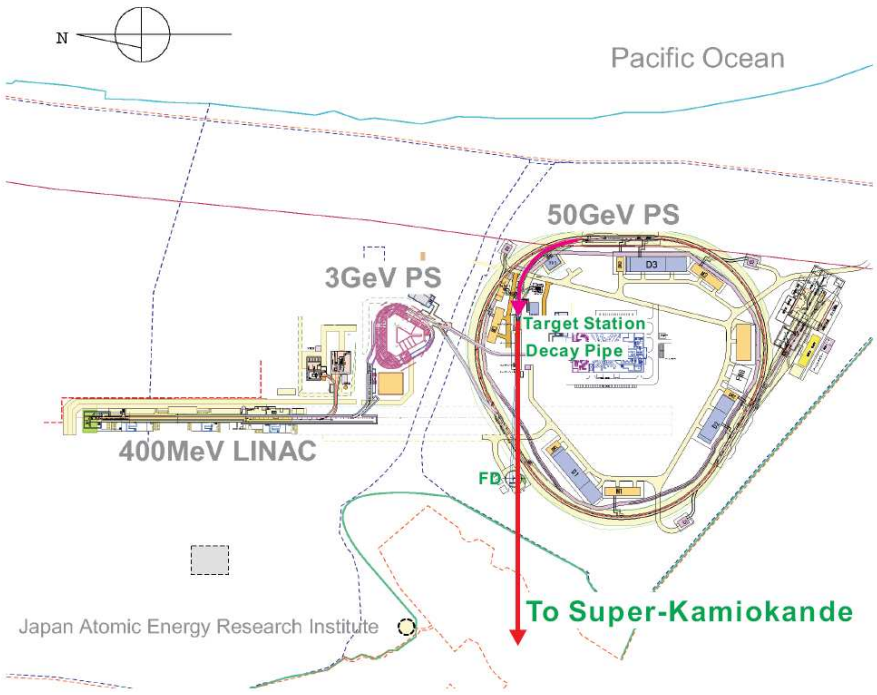

Figure 2.6: Overview of the JPARC Facility [77]

configurations of the T2K beamline and detectors are illustrated in figure 2.7. They consist of the proton beamline, target station, decay volume,

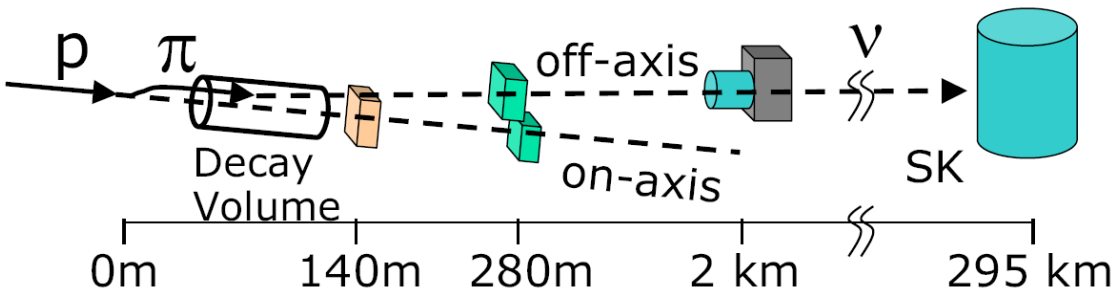

Figure 2.7: Schematic configurations of the T2K beamline and detectors [27]

beam dump, muon monitors at 140 m downstream from the target, first near

detectors at 280 m, second near detectors at 2 km (proposed) and SK far detector at 295 km distant.

2.3.2 The ν_μ Beam

In the first stages of the experiment a proton beam of energy 30 GeV will hit a helium-cooled graphite rod target to generate charged pions, which will be focused by electro-magnetic horns to a decay tunnel.

Muon neutrinos are produced by

$$\pi^+ \rightarrow \mu^+ + \nu_\mu \tag{2.1}$$

as well as a small flux of contaminating electron neutrinos arising from

$$K^+ \rightarrow \pi^0 + e^+ + \nu_e \tag{2.2}$$

and

$$\mu^- \rightarrow e^- + \nu_\mu + \overline{\nu}_e \tag{2.3}$$

The length of the decay tunnel from the target position is 110 m and at the end of the tunnel is the beam dump. The beam dump, composed of water-cooled graphite blocks surrounded by an iron shield, will stop all remaining protons, pions and low energy muons. Downstream of the beam dump is placed a muon monitor, called MUMON, which will be a segmented ionisation chamber and array of semiconductor detectors to monitor the intensity, profile and direction of the beam.

2.3.3 Off-Axis Beam Configuration

The neutrino beam direction is around 2.5 degrees away from the direction of Super-Kamiokande and the 280 m detector. This allows a quasi-mono-energetic ν_μ beam to be made with energy E_{ν_μ}

$$E_{\nu_\mu} = \frac{m_\pi^2 - m_\mu^2}{2(E_\pi - p_\pi \cos\theta)} \tag{2.4}$$

Figure 2.8 shows the neutrino energy spectra of charged current interactions at different off-axis angles. The off-axis beam configuration produces a narrow neutrino energy spectrum. The peak neutrino energy can be adjusted by choice of the off-axis angle, and can therefore be selected to be near the oscillation maximum at the far detector. The T2K off-axis angle will be able to be changed between 2° and 3°, corresponding to neutrino energies from 0.5 - 0.9 GeV.

Backgrounds arise from inelastic reactions of high-energy neutrinos. For the ν_e appearance search the main background is through the neutral current production of π^0s. With an off-axis configuration the highest possible intensity of low energy neutrinos is achieved, and with a reduced high-energy

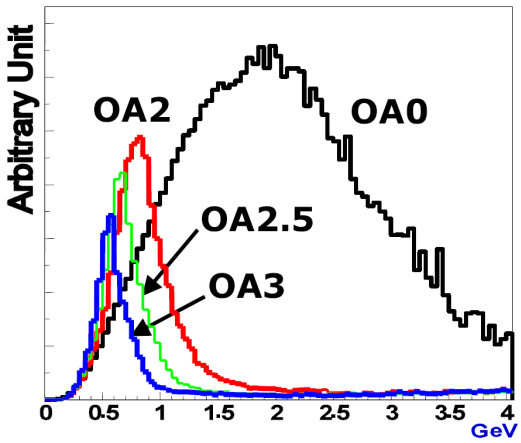

Figure 2.8: Neutrino energy spectra as a function of off-axis (OA) angle (angle stated in degrees) [76]

tail in the spectrum (as shown in figure 2.8). The intrinsic contamination of the beam by ν_e through kaon and pion decay is reduced by cutting out the high E_{ν_μ} tail.

2.3.4 E_ν Reconstruction

The oscillation maximum will occur at a neutrino energy E_ν less than 1 GeV for the 295 km baseline (with $\Delta m^2 \approx 3 \times 10^{-3}$ eV^2). The neutrino energy corresponding to the first oscillation maximum, E$_{oscmax}$, is obtained from

$$\left(\frac{1.27\Delta m^2_{23}}{E_{oscmax}}L\right) = \frac{\pi}{2} \tag{2.5}$$

Fortuitously this coincides with the peak of the main neutrino interaction cross-section, dominated by the charged current quasi-elastic interactions, as illustrated in figure 2.9. The reaction enables precision determination of both E_{ν_μ} and E_{ν_e}, which can be calculated by 2-body kinematics

$$E_\nu = \frac{m_N E_l - m_l^2/2}{m_N - E_l + p_l \cos\theta_l} \tag{2.6}$$

where m_N is the neutron mass, m_l is the lepton mass (= e or μ), E_l, p_l and θ_l are the energy, momentum and angle of the lepton relative to the neutrino beam, respectively.

2.3.5 Far/Near Correction

The neutrino source can be considered point-like at Super-Kamiokande, but is a line source at the near detector as the length of the decay pipe cannot be considered negligible. This causes the energy spectrum to be shifted to higher

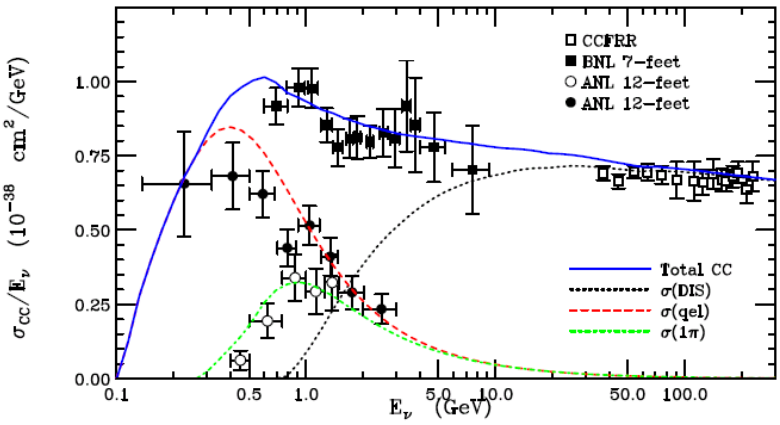

Figure 2.9: Charged current neutrino cross sections as a function of energy. Shown are the contributions from quasi-elastic (dashed), single pion (dot-dashed) and deep inelastic scattering (dotted processes). At the sub-to-few GeV range neutrino interactions are predominantly quasi-elastic [78]

energy at the far site than at the near site. This far/near effect is illustrated in figure 2.10, which compares the neutrino beam spectrum 2 degrees off-axis for the detectors at 280 m, 2 km and 295 km. Figure 2.11 (left) shows the

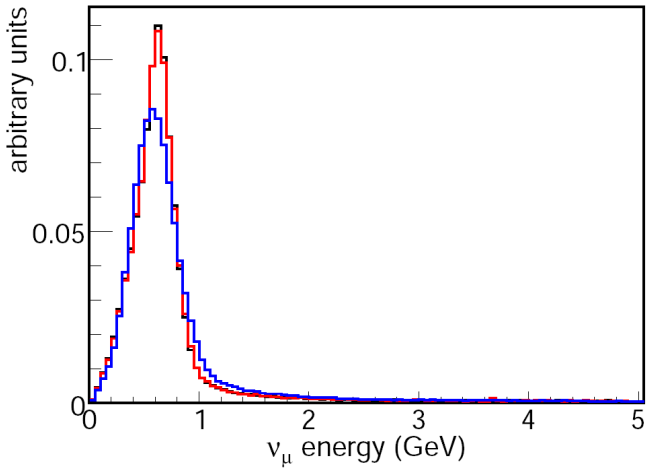

Figure 2.10: Comparison of the ν_μ spectra at 280 m (blue line), 2 km (red line) and 295 km (black line), for OA2° [79]

ratio of the far ν_μ flux to near flux as a function of energy. Since the peak positions are shifted at 280 m relative to at SK, the far/near ratio can be seen to change right in the region of the oscillation maximum.

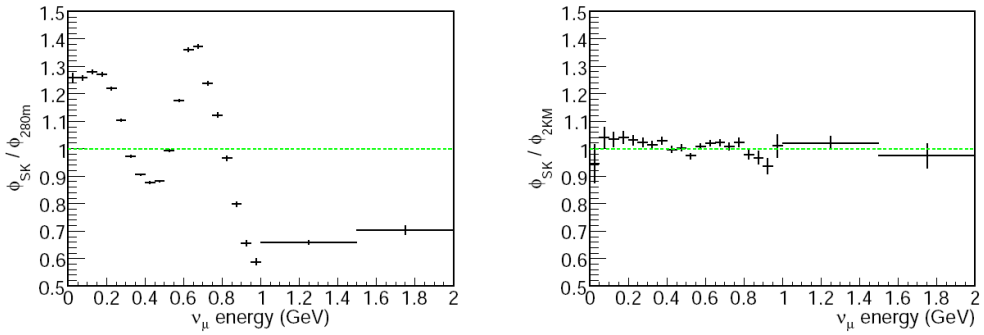

Figure 2.11: The far/near neutrino flux ratio as a function of energy 280 m from the T2K target (left) and 2 km from the T2K target (right) [79]

2.4 The T2K Near Detector

The Near Detector is located at 280 m from the neutrino source. It will consist of an off-axis detector (ND280) and an on-axis detector called The Interactive Neutrino Grid (INGRID).

2.4.1 On-Axis Detector: INGRID

The purpose of INGRID is to monitor the neutrino beam direction, vital to precisely maintain the off-axis angle of the beam. It will also monitor the intensity and mean energy. It will do this via 14 modules in a cross configuration (7 horizontal and 7 vertical), with 2 additional modules to account for beam asymmetry, centred on the beam position. The INGRID module configuration is shown in figure 2.12. Each module is composed of 11 layers of 3 cm thick scintillator with 6.5 cm thick layers of steel placed between each tracking plane [80].

INGRID has been designed to provide sufficient statistics to determine daily the beam direction within 1 mrad, corresponding to a 2% (14 MeV) shift in the off-axis spectrum. It will also be able to resolve beam displacement better than 1 mm at the target [81].

2.4.2 Off-Axis Detector: ND280

The ND280 must measure the flux and spectrum of ν_μ and cross-sections for ν_μ interactions for the ν_μ disappearance study. Similarly for the ν_e appearance study the flux, spectrum and cross-sections for interactions of ν_e need to be measured. Also vital is the characterisation of the backgrounds (mainly the poorly understood π^0 production channels) which may affect the ν_e appearance signal. To facilitate these precise measurements the detector needs to be large volume and highly segmented to identify and measure the

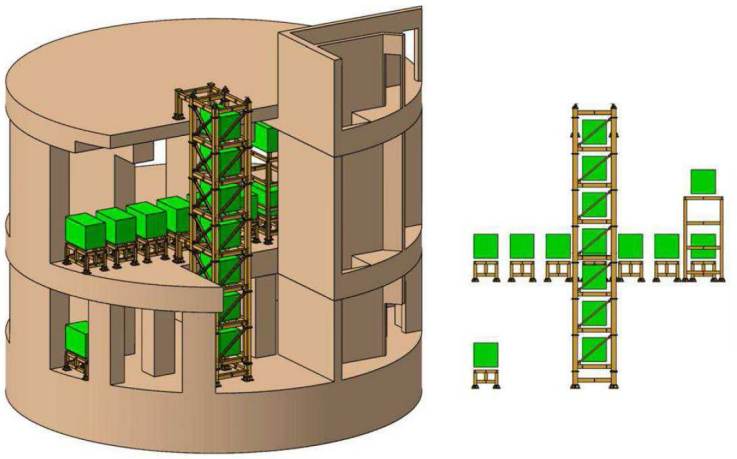

Figure 2.12: Design of the on-axis INGRID detector. The centre of the cross intersects with the centre of the beam. Each module in the cross is a muon-detector of iron and plastic scintillator [80]

energies of interacting particles. Since this is a neutrino beam experiment an interaction can occur anywhere within the ND280.

The design for ND280 is shown in figure 2.13. It consists of the UA1 magnet, a π^0 detector (P0D), a tracking detector consisting of time projection chambers (TPCs) and fine grained scintillator detectors (FGDs), and several electromagnetic calorimeters: a downstream ECal (DSEcal), a barrel ECal (BrECal) which surrounds the four outer faces of the tracker region and a P0D ECal which surrounds the four outer faces of the P0D region. All of the detectors, except the BrECal and P0D Ecal, will be assembled inside a metallic frame (known as the basket). The gaps inside the magnet yoke are instrumented with scintillator slabs to form the side muon range detector (SMRD).

It is not practical to use a water Cherenkov detector at this distance since the high neutrino flux produces unacceptable event overlap. Therefore the ND280 is based primarily on plastic scintillator (extruded polystyrene with 1% PPO and 0.03% POPOP). However this introduces a systematic error in that neutrino interactions in the ND280 will be on plastic (and therefore primarily on carbon), whereas neutrino interactions in Super-Kamiokande are on water (and therefore primarily on oxygen). For this reason various components of the ND280 will include water layers to act as neutrino targets. Wet and dry runs will allow the water-based interactions to be separated. At present all the water layers simply contain water and are therefore passive.

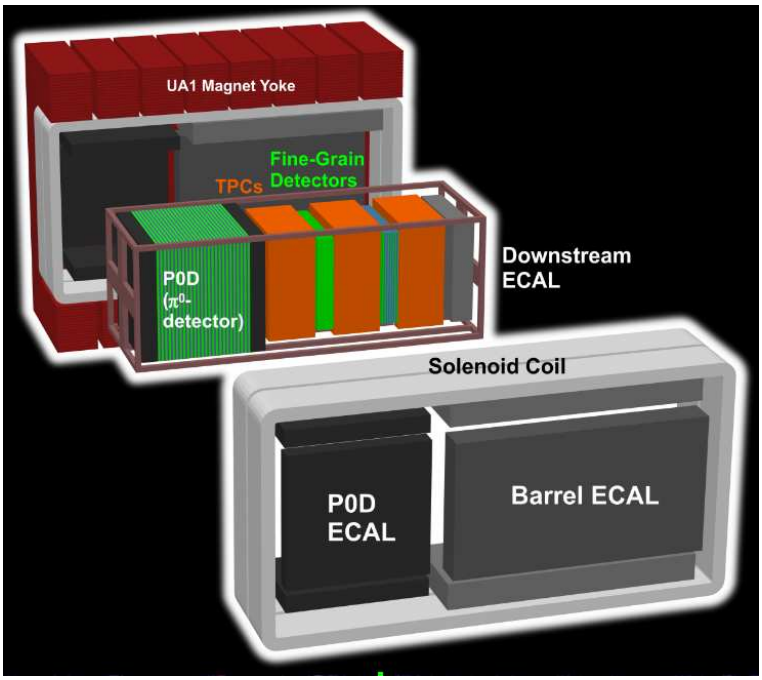

Figure 2.13: Expanded view of the 280m detector [77]

2.4.3 Magnet

The ND280 detector components will be placed in the volume inside the UA1 magnet (previously used in the NOMAD experiment and recommissioned for T2K) operated with a magnetic field of 0.2 T.

2.4.4 Pi-Zero Detector (P0D)

The Pi-Zero Detector (P0D) will measure neutral current π^0 interactions, in particular those produced in a water target. It will measure the π^0 production channels $\nu_\mu + n \rightarrow p + \mu^- + \pi^0$ and $\nu_\mu + N \rightarrow \nu_\mu + N + \pi^0$, which have poorly known cross-sections at E < 1 GeV. The P0D consists of 40 $x - y$ scintillator bar tracking planes interleaved with sheets of lead foil (known as P0Dules). A diagram of the P0D is shown in figure 2.14. The triangular scintillator bars are 17 mm in height and 32.5 mm in base, co-extruded with a TiO_2 surface treatment. Each scintillator module is constructed from 128 (136) bars oriented in the x (y) direction. End caps keep the ends of the scintillator bars light-tight while guiding the each end of the wavelength-shifting (WLS) fibres to a multi-pixel photon counter (MPPC). The lead enhances γ conversion close to the vertex to allow maximum efficiency for π^0 event reconstruction. A coarse calorimeter plane (P0DEcal) is installed around the P0D to capture any escaping photons and to tag sideways-going muons and pions.

Plastic bladders, dimensions $0.03 \times 1.8 \times 2.1$ m^3, filled with 100 kg of

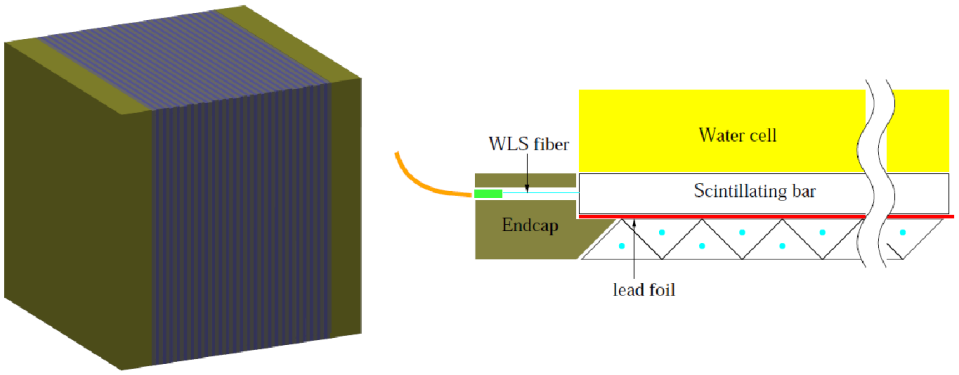

Figure 2.14: Diagram of the P0D detector, alternating water target and scintillator tracking layers (left) and a schematic of a P0D scintillator layer (right) [77]

water each will be used as passive targets and will be run in both empty and full configurations to statistically separate interactions on carbon and water.

Since the primary goal of the P0D active target is neutral current single π^0 production the P0D must have high efficiency to detect gamma rays leaving the fiducial volume. By requiring a localised cluster of energy deposited in the X or Y projection, the active target will detect 85% of gamma rays with $E > 100$ MeV that originate more than 30 cm from the edge of the detector [77]. The design goal for the P0D is to achieve a 30% reconstruction efficiency for π^0.

2.4.5 Tracker: TPC

Downstream of the P0D lies the tracking detector with the main aim of measuring the momenta of charged particles and the background ν_e in the beam. The ND280 tracker section consists of three time projection chambers (TPCs) and two fine grained detector (FGD) modules.

The purpose of the TPCs is to provide high resolution momentum measurements of curved tracks. The magnetic field in which the detectors will sit is relatively weak, meaning the curvature of tracks is limited, requiring a good space point resolution. This will enable the charge of the neutrino interaction products to be determined. Ionisation energy loss measurements will help distinguish electrons and protons from muons and pions.

A diagram of the TPC is given in figure 2.15. The inner box forms the field cage and drift volume and the outer box forms a carbon dioxide volume that provides electrical insulation from the cathode voltage.

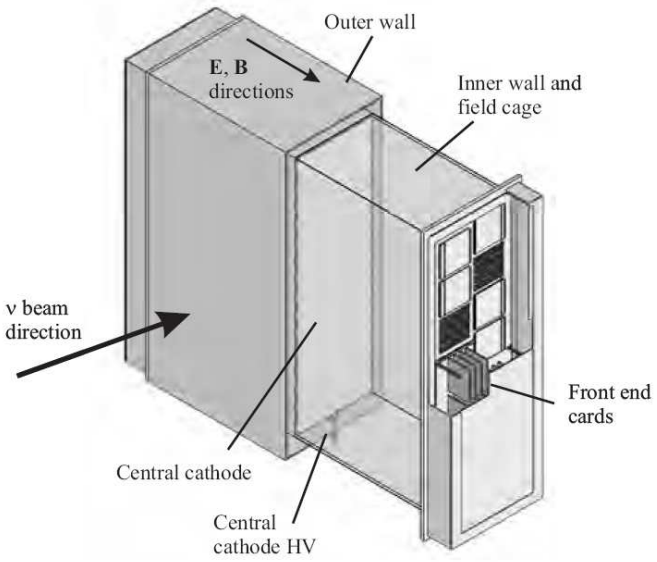

Figure 2.15: Drawing of the TPC showing the inner and outer boxes and central cathode [82]

2.4.6 Tracker: FGD

The ND280 detector will contain two massive FGD modules placed in between the TPCs. The FGDs provide target mass for neutrino interactions and track charged particles coming from the interaction vertex. They are thin enough ($<$ 30 cm) that most of the penetrating particles produced in neutrino interactions will reach the TPCs, which will measure their momenta and charges by their bending in the magnetic field. The FGDs will primarily measure the short ranged protons emerging from the CCQE interactions. The FGDs therefore need fine grained segmentation so that individual particle tracks can be separated and their directions determined.

The first FGD consists of 5760 extruded polystyrene scintillator bars arranged into 30 layers of 192 bars each. Each layer is orientated alternating in the x and y directions perpendicular to the neutrino beam, to allow for tracking information to be achieved. Each scintillator bar measures 0.96 cm $\times$ 0.96 cm $\times$ 184.3 cm with a WLS fibre through its centre leading to a MPPC at either end. The second (more downstream) FGD is water-rich and contains seven $x-y$ sandwiches of plastic scintillator layers alternating with six 2.5 cm thick layers of water. The neutrino interaction rates on carbon are determined from the all plastic FGD and the interaction rate on plastic plus water measured in the second FGD. The interaction rate on water is then determined by subtraction of the latter from the former. The scintillator, fibres and PMTs are housed in a light-tight dark box and the electronics mounted in crates outside of the dark box. A schematic diagram of an FGD is shown in figure 2.16.

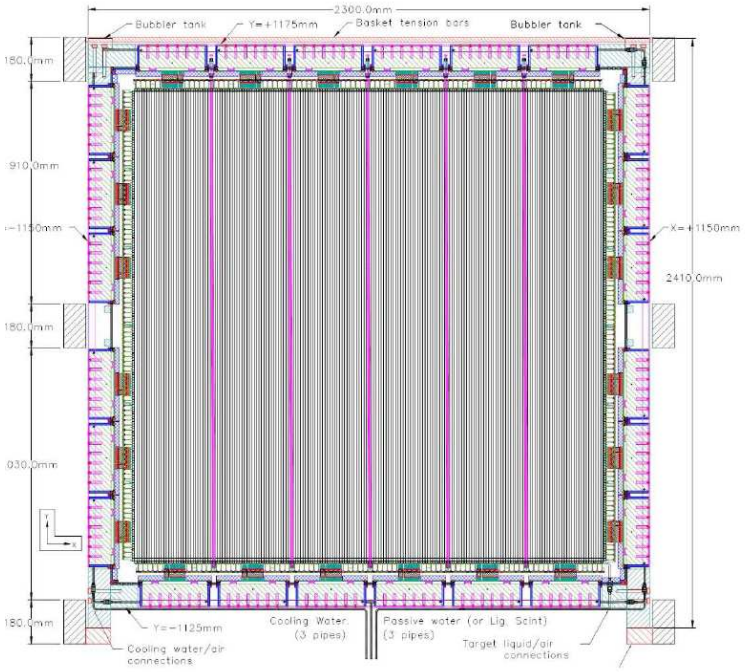

Figure 2.16: End view of an FGD. The XY scintillator layers hang from nylon straps (in magenta) inside the dark box. Twenty-four mini-crates on the four sides of the FGD contain the front-end electronics boards, and the PMTs are mounted on bus boards attached directly to the edges of the scintillator [83]

2.4.7 Electromagnetic Calorimeter (Ecal)

The main aim of the Ecal is to capture and characterise electromagnetic energy (γ-rays) produced in and escaping the inner detectors. Of particular importance (as a background to the ν_e appearance search) are the photons produced by the decay of neutral current produced π^0s.

The Ecal consists of lead-scintillator sandwich sampling calorimeter modules located around the ND280 inner detectors on all four sides and at the downstream end of the magnet. The Barrel Ecal surrounds the basket containing the TPCs and FGDs and will detect, reconstruct and identify particles leaving the tracking volume. The P0D Ecal surrounds the P0D and will identify photons and muons escaping the P0D. The Downstream Ecal (DSEcal), is located in the basket downstream of the Tracker and will identify particles that pass straight through the tracker volume.

The Barrel Ecal comprises 32 scintillator bar layers (cross-section 4 cm $\times$ 1 cm) separated by 31 layers of 1.75 mm thick lead sheets and the DSEcal 34 active layers interleaved with 33 lead sheet converter layers. The P0D is surrounded by more coarsely segmented Ecal layers comprising 6 active scintillator slabs separated by 4 mm thick lead converter.

The DSEcal has been constructed in Britain during 2008; and took cosmic

ray data and test beam data at CERN to test its overall performance during 2009.

2.4.8 Side Muon Range Detector (SMRD)

For CCQE processes, the neutrino energy is correlated with the muon energy, and can be reconstructed using the muon momentum and scattering angle. The TPC will measure the muon momenta for forward travelling muons, but muons scattered at larger angles will escape. They will however cross the magnet surrounding the entire detector, so between the iron plates of the magnet yokes plastic scintillator embedded with WLS fibres will be sandwiched. A muon's momentum can therefore be inferred from its range by instrumenting the iron at various depths.

The iron yoke consists of sixteen C-shaped elements, each of which is made of sixteen 48 mm thick iron plates, with 17 mm air-gaps between the plates. These air-gaps will be instrumented with slabs of 7 mm thick extruded plastic scintillator which contain an embedded S-shaped wavelength shifting fibre. This is illustrated in figure 2.17. This shape is chosen since it allows the fibre to collect the scintillation light over the whole surface of the slab while minimising the propagation length of scintillation light to the fibre and keeping the number of required readout channels to a minimum.

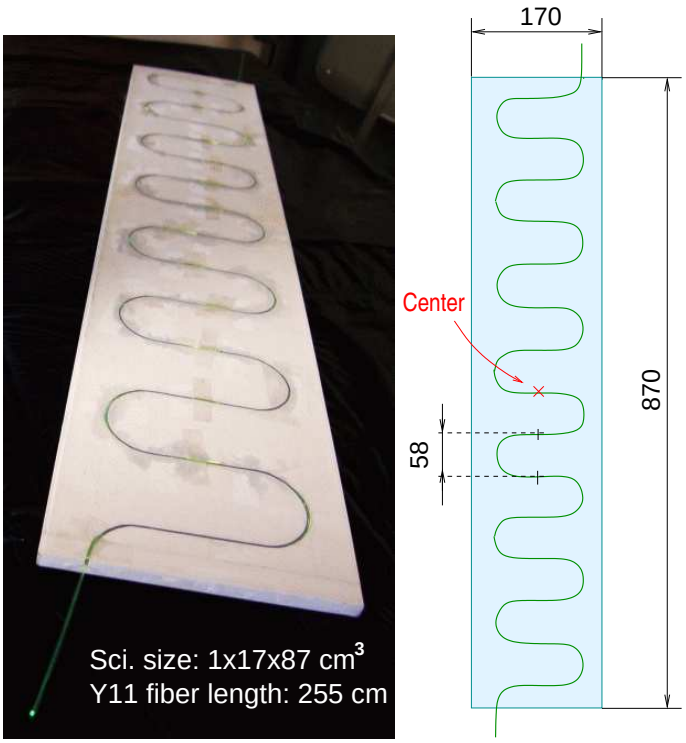

Figure 2.17: Prototype scintillator with machined S-shaped groove with an embedded WLS fibre. Photograph (left) schematic view (right) [84]

2.4.9 Current Status of the ND280

In January 2010 all of the sub-detectors have been fit inside the magnet which has been closed to contain them. Shortly thereafter in February 2010 the first cosmic ray event was seen in the ND280, illustrated in figure 2.18.

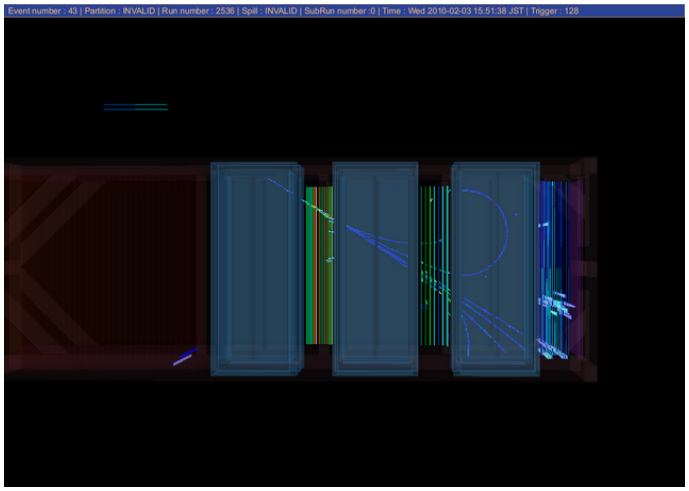

Figure 2.18: Cosmic ray interaction inside the ND280 taken February 2010

2.4.10 Intermediate Detector

The beam profile a few kilometres from Tokai is essentially identical to that at Super-Kamiokande, leading to a near to far ν_μ flux ratio which is nearly independent of energy (see figures 2.10 and 2.11). Furthermore, at this distance the event rate is sufficiently low enough to allow a large water detector Cherenkov detector to be used as an effective detector.

The conceptual design for a T2K Intermediate Detector, to be situated approximately 2 km from Tokai, consists of a "mini-Super-Kamiokande" water Cherenkov detector, with 20 cm PMTs (to give resolution comparable to Super-Kamiokande's 50 cm PMTs in a larger detector), along with a liquid argon TPC. This detector is probably essential to attain the sensitivities hoped for in the second phase of T2K, but no suitable site has yet been acquired. It is hoped to install it at a later date as a major upgrade.

2.4.11 The Far Detector: Super-Kamiokande

Super-Kamiokande is a 50 kiloton water Cherenkov detector, situated 1 km beneath the ground in a Japanese mine. The detector is illustrated in figure 2.19. The detector consists of a stainless steel tank 39 m diameter and 42 m tall. Within the tank a stainless steel framework supports 11,146 inward facing PMTs (which together with the water volume they view are referred to the Inner Detector). The PMTs (Hamamatsu R3600 [85], [86]) have a

photocathode diameter of 50 cm. The spaces between the PMTs are covered with opaque, black polyethylene telephthalate sheets, which improve the optical separation between the inner and outer detector and suppress unwanted low-energy events due to residual radioactivity occurring behind the PMTs. The Outer Detector is made up of a more sparse array of 1885 outward facing PMTs. The main purpose of the Outer Detector volume is to serve as an active veto counter for incoming particles such as cosmic ray muons, to tag exiting charged particles from the Inner Detector and also to act as a passive radioactivity shield for neutrons and γ rays from the surrounding rocks [87]. The entire surface of the Outer Detector is lined with reflective white Tyvek sheets.

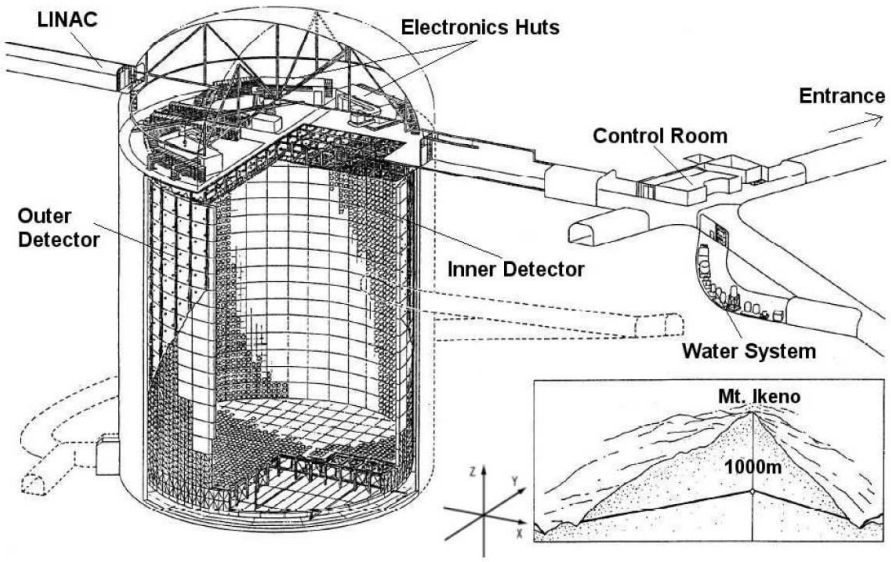

Figure 2.19: The Super-Kamiokande detector site, under Mt. Ikenoyama [88]

In 2001 an imploded PMT caused a chain reaction which destroyed a large number of PMTs; the detector has now undergone a massive refurbishment project to fully restore the PMT density for the T2K experiment. Each Inner Detector PMT is now encased within an acrylic cover to absorb the shock of any implosion that may occur. Figure 2.20 shows an image of the PMTs and their casings during the refurbishment of SK; the PMTs are waiting to be lowered into the main tank for fitting into the metal frame and testing.

2.4.12 Future Extension: Hyper-Kamiokande

In the second phase of the T2K experiment the proton beam intensity is expected to increase to 4 MW [75] and the neutrino production target will be upgraded to a liquid metal target to accept this beam. An upgrade to the far detector, Hyper-Kamiokande, a 1 Mt volume water Cherenkov detector

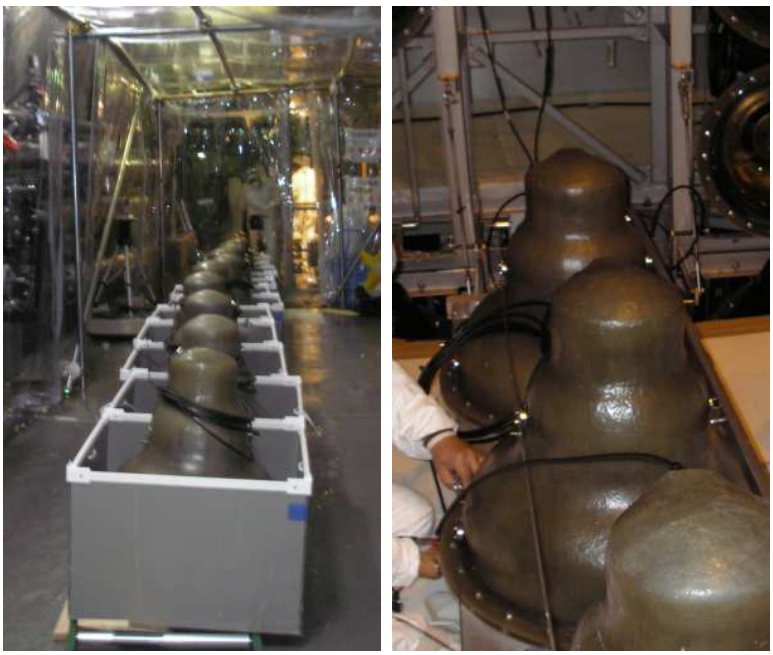

Figure 2.20: Photograph of the acrylic covers used to house the PMTs during the refurbishment of the Super-Kamiokande detector

in the Kamioka site is proposed. These two measures would increase the statistics by a factor of 200 allowing the measurement of $\sin^2 2\theta_{13}$ sensitivity below 10^{-3} and the CP phase δ measurement down to 10-20 degrees.

2.4.13 Conclusions

The aims and experimental configuration of the T2K experiment have been described. In particular interest to the topic of this thesis is the passive water layers contained within the ND280; these are included to provide an oxygen rich target to reduce systematic uncertainties when comparing the signal with that at the SK water detector. The possibility of upgrading these layers with a water-based active scintillator layer will be explored in all subsequent chapters.

Chapter 3

Motivation for Active Water in the T2K Near Detector

3.1 Introduction

The development of a water-based scintillating mixture to replace the passive water bags in some of the ND280 sub-detectors will provide an oxygen rich and active target material at the near detector to minimise cross-section uncertainties. This chapter presents a study to justify this possible future upgrade and investigate how efficient a water-based scintillator will need to be, when compared with plastic scintillator, to obtain more tracking information than is gained when using plastic scintillator alone. Subsequent chapters will then describe the development and testing of such a water-based liquid scintillator and its container for the ND280.

3.2 Water in the T2K Near Detector

The target mass for neutrino interactions in the ND280 will be provided by segmented scintillator bars read out by wavelength-shifting (WLS) fibres. For neutrinos near $\sim$ 700 MeV, the dominant reaction is charged current quasi-elastic (CCQE) ($\nu_\mu n \rightarrow \mu^- p$). Fine-grained segmentation allows tracking of both outgoing particles giving a strong kinematic constraint to reject backgrounds. Using a scintillator rather than a Cherenkov detector allows the detection of the recoil proton, which is below the Cherenkov threshold.

Unfortunately in this design the target mass is mostly plastic scintillator (therefore carbon rich), whereas the bulk of the mass of the far detector Super-Kamiokande is water (therefore oxygen rich). Systematic effects caused by the use of these different nuclear targets will unavoidably arise and the effects are not well known. The cross-section for all neutrino interactions depends on the target material in an unmeasured way. In particular the current theoretical understanding of the corrections for the cross-section differences from different nuclei (especially the modifications for pion ab-

sorption in the nuclear medium which can make 30-50% corrections to the total cross-sections) is poor. Additionally resonance production in oxygen is affected differently than in carbon due to long-range nuclear correlations. There are also no measurements of how the final state interaction probability for pions, in particular neutral pions, is affected by the target nucleus.

In the ND280, one of the FGDs consists entirely of layers of plastic scintillator bars while the second is water-rich, with scintillator layers alternated with 3 cm thick layers of water held in sheets of corrugated polypropylene. Neutrino interaction rates on water can be obtained from a subtraction analysis whereby the rates on the all plastic FGD and the water-rich FGD are measured, corrected for differences in efficiency, and the interaction rates on carbon determined from the plastic FGD are subtracted from the plastic and water FGD to determine the interaction rate for just water. An all plastic FGD will still be required in the first instance for the plastic/water comparison, to account for the plastic of the containers and WLS fibres that cannot be avoided.

The P0D is also a solid scintillator strip detector with a water target held inside thin (30 mm) high-density polyethylene containment bags inside PVC frames sandwiched between the 30 upstream scintillating bar tracking planes, with an aluminium drip pan to catch any leaks [89]. Oxygen cross-section measurements can be similarly made by comparing the interaction rate for event vertices in the upstream and downstream portions of the detector.

Presently the water in these cases does not contribute to the detection process of secondary particles. In utilising a water-based liquid scintillator, in addition to benefiting from oxygen as a neutrino target, the active water will improve the identification of secondary particles in a neutrino interaction.

3.3 Simulation of Sub-Detector with Active Water Component

The aim of this simulation study is to estimate how efficient an active water scintillator needs to be when compared with a plastic scintillator to provide extra pertinent information about the neutrino interactions. It is important to note here that this is not a full T2K detector simulation. Because of the CPU intensive nature of simulating optical photons, scintillation and optical photon propagation are parameterised in the official ND280 Monte Carlo and subsequently convoluted with the simulated electronics. Since this investigation is looking at the effect of changing the light yield of a scintillator mixture, these processes are an important aspect of this study. Therefore the full T2K software package is not used and a ND280 sub-detector is constructed using the Geant4 [90] framework, utilising physics lists that support scintillation and photon propagation. In particular the CCQE interaction is studied. This interaction is characterised by a long muon track and a short proton track. A typical such event is illustrated in figure 3.1. Since the pro-

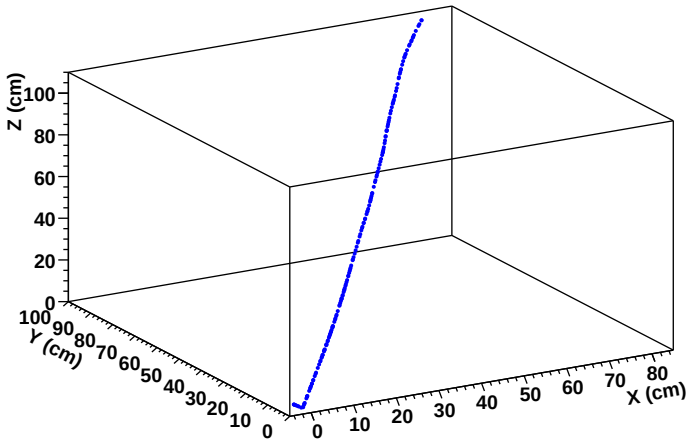

Figure 3.1: Diagram of a typical CCQE event exhibiting a long muon track and short proton track in the framework of the simulated detector. In this event the muon track is approximately 130 cm and the proton track 3 cm length

ton tracks are short extra sensitivity provided by active water layers could improve the detection of such tracks.

3.3.1 Neutrino Interaction Monte Carlo Generation

Neutrino interactions are simulated by the NUANCE [91] event generator. The generator takes information about the flavour, energy and direction of a neutrino and the incident material (single nuclei) as an input. The input T2K neutrino beam flux used for all event generation is shown in figure 3.2.

The event generation takes two steps. The first is the most CPU intensive and produces a binary file with the information about the rates of all the interaction types. This is then passed to an event generator which uses MC sampling of these rates to generate each event type and final particle states. The theoretical and phenomenological models for the calculations of effects of a bound nucleon target, electron scattering, quasi-elastic scattering, resonant processes, coherent and diffractive reactions, deep-inelastic scattering and nuclear processes are detailed in reference [91]. NUANCE outputs a list of events with information about the reaction mode of the event (e.g. charged/neutral current quasi-elastic, single-pion resonant production etc), final state particles and their energies and their x, y, z direction cosines.

Placement of the interaction vertices is left to the detector simulation, written using Geant4, which simulates the passage of particles through matter, allowing one to study the detector's response to neutrino interaction events. This detector simulation accepts the NUANCE output files as input files. One million events are generated using NUANCE upon C nuclei and one million upon O nuclei. The interaction vertices from the C events are

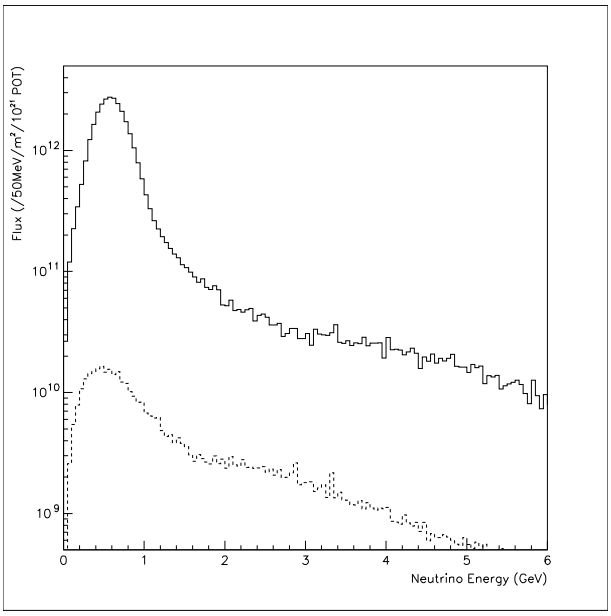

Figure 3.2: Energy spectra of the off-axis 2.5 degree T2K beam: solid line (ν_μ) and dashed line (ν_e). Both histograms have been normalised to 10^{21} 40 GeV protons on target [92]

chosen to be in the centre of the first plastic scintillator sheet and from the O events placed in the centre of the first active water sheet of the simulated detector.

3.3.2 Construction of a ND280 Sub-Detector

Geant4 provides tools for simulating detector geometries and propagating particles through them. The detector geometry is constructed from the creation of volumes which then have material properties associated with them. Volumes of the detector that actively measure a particle's passage are given sensitive properties, which means that the information about the particle and its energy deposited in the material is stored. The construction method of the simulated detector sets dimensions of the detector parts, defines materials (from input elements), geometries and surfaces. It also includes a horizontal, uniform magnetic field of 0.2 T perpendicular to the neutrino beam direction.

The design and dimensions of the sub-detector created for this study are based upon the design for the P0D detector, described in section 2.4.4. The sensitive detectors comprise plastic and water-based scintillator bars. The extruded plastic scintillator bars are triangular, arranged in a sheet of 40 slabs, alternating positioned upwards and downwards. Between 2 such sheets (where the top and the bottom sheets are oriented 90° with respect to each other) is a 0.6 mm thick sheet of lead. Three water sheets then follow

the transverse scintillator bar sheets. The water is held in corrugated plastic sheets with flutes $1\,\mathrm{cm}^2$ in cross-section. Each sheet is again alternately oriented longitudinally at 90° rotation in the transverse plane. This is illustrated in figure 3.3 detailing the naming used for the bars in the simulation. The first complete layer (i.e. 2 plastic sheets separated by a lead sheet and followed by 3 water sheets) is numbered layer 0. There are 40 such layers in total which make up the simulated sub-detector. The detector is 1.8 m long in the x plane (labelled front view) and 2.1 m long in the z plane. The neutrino beam travels in the positive y direction.

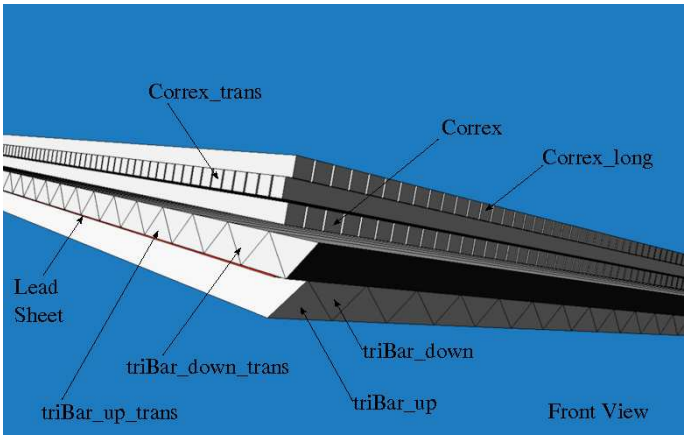

Figure 3.3: Diagram of single layer of simulated sub-detector

3.3.3 Physics List

There are three categories of physics models at the heart of the Geant4 program: those driven by theory, parameterised models which combine theory and data and empirical models driven solely by data. The user chooses which physics models and which cross-section data are used in a given energy range. A physics list consists of particles, processes and cross-sections. A set of ready made physics lists is available with the Geant4 source code. In this simulation the LHEP [93] list is chosen, which contains standard EM processes and describes showers well, with added optical photons and relevant processes which include Cherenkov, scintillation, absorption, Rayleigh scattering and boundary processes.

3.3.4 Method

In the MC the following track information is recorded: number of photons (NPhotons), number of tracks (NTracks), event identification number (EventID), energy deposition in MeV (EDep), name of bar (BarName), name of particle (ParticleName), PDG particle identification (ParticleID) and active water light yield (AwLightYield).

A scintillation photon is counted only once, before any reflection or transmission (since conservation of energy is not guaranteed in Geant4 [90]). The MC outputs the total number of photons in each scintillator bar after each simulation. The first simulation is run with the active water scintillator yield set to be 0% of that of the plastic scintillator (i.e. 0 photons/MeV). The same simulations are then repeated but with the active water scintillation yield increased each time in increments of 10% up to 100% (i.e. 10,000 photons/MeV). A 1000 events for each lightyield are generated.

Hits are recorded by the sensitive areas of the detector and are output into a ROOT file.

3.4 Results

3.4.1 Validation

A sanity check is performed to check that the photons created in the simulation are in line with the input light yield. Plotted in figure 3.4 is the number of scintillation photons yielded as a function of energy deposited in the plastic and water scintillator bars. For the plastic scintillator bar the frequency curve of the number of photons as a function of energy peaks at 10,000 photons/MeV as expected. Each active water scintillator bar light yield is also checked and they all output the expected values; that of a 50% light yield is presented and a peak at 5000 photons/MeV is observed as expected.

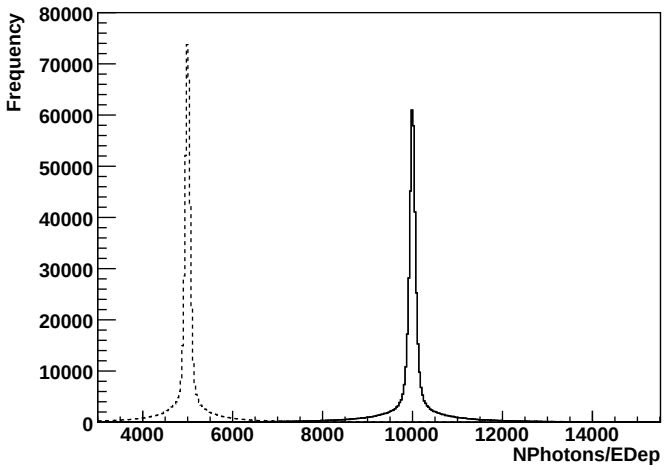

Figure 3.4: Plot to verify the input light yields of plastic and water scintillator bars: shown is the number of photons produced in plastic scintillator bars as a function of energy deposited (solid line) and those produced in water scintillator at 50% light yield (dashed line)

3.4.2 Minimum Ionising Particles in the simulation

The rate of energy loss of a charged particle passing through a material, $-dE/dx$, is approximately given by the Bethe-Bloch formula (see for example [94]). In brief terms:

$$-\frac{dE}{dx} \propto \frac{z^2}{v^2}\rho \tag{3.1}$$

where:

$$\begin{aligned} z &= \text{charge of particle} \\ v &= \text{velocity of particle} \\ \rho &= \text{density of scintillator} \end{aligned}$$

A plot of the Bethe-Bloch formula as a function of kinetic energy for different particle types is given in figure 3.5. It is observed that the rate of energy loss, $-dE/dx$, decreases with increasing velocity until about $v \simeq 0.96c$ where a minimum is reached [94]. Particles at this point are known as minimum ionising particles (MIPs). For carbon the MIP minimum is around $-dE/dx \simeq -1.8$ MeV/g/cm^2, as illustrated in figure 3.6. The input NUANCE muon momentum spectrum is plotted in figure 3.7. The average muon momentum is found to be 1.3 GeV/c. This corresponds to an energy loss of around $-dE/dx \simeq -2$ MeV/g/cm^2, confirming that the muons can be considered as MIPs in this study.

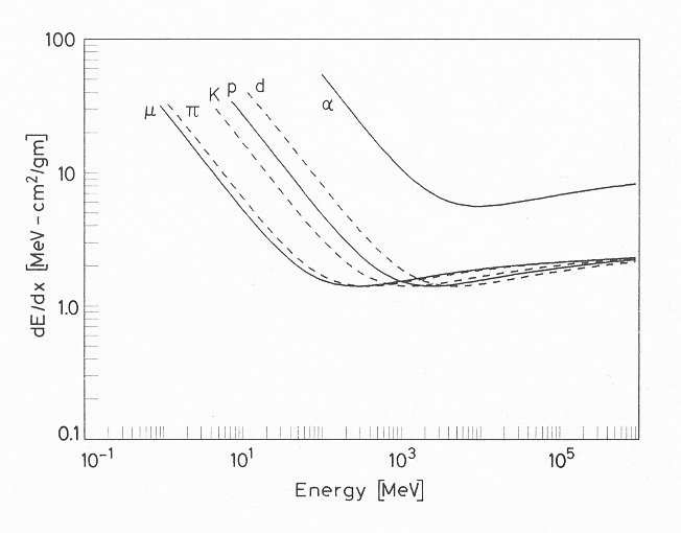

Figure 3.5: Variation of the rate of energy loss, $-dE/dx$, as a function of energy for different particle types [94]

The energy deposited by muons in plastic scintillator bars is plotted in figure 3.8. On average an energy deposition of 1.8 MeV/cm is expected. Since the average energy deposited by muons in scintillator bars is determined to be

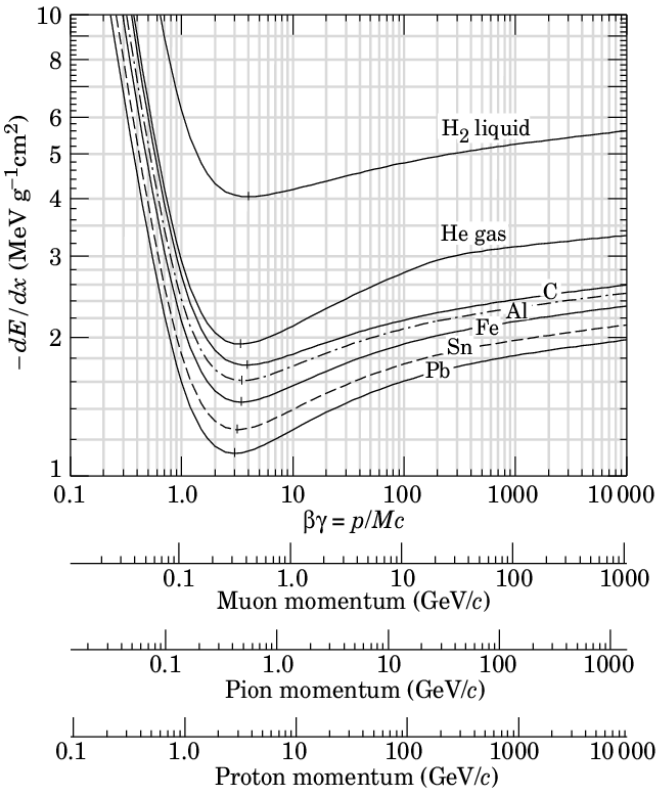

Figure 3.6: Mean energy loss rate in liquid hydrogen, gaseous helium, carbon, aluminium, iron, tin and lead [95]

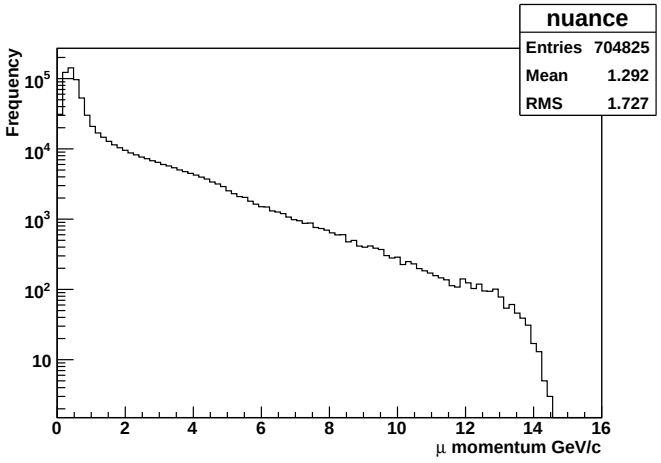

Figure 3.7: NUANCE input muon momentum

2.6 MeV/bar, this implies the average muon traverses 1.4 cm of a particular triangular bar which is consistent with the geometry of the bars.

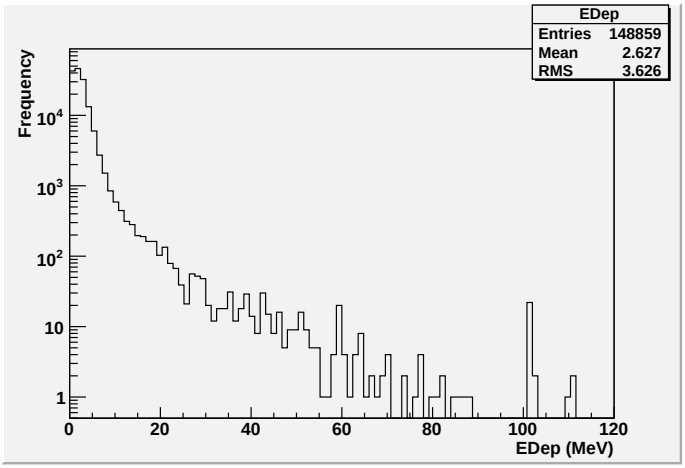

Figure 3.8: Energy deposited by muons (per bar) in plastic scintillator bars

3.4.3 Threshold for water-based scintillator

For the sake of this study it is assumed that MIPs, and therefore muons, represent the weakest detectable signal. The average number of photons per plastic scintillator bar per MIP particle is plotted in figure 3.9. The

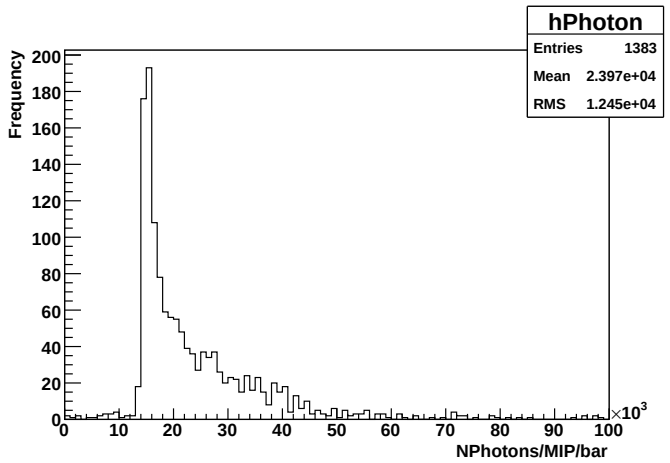

Figure 3.9: Number of photons per plastic scintillator bar per MIP particle

mean value is found to be 24k photons/muon (MIP)/plastic scintillator bar. This value is now taken as the threshold for the number of photons that must be produced in a water-based scintillator bar by protons, for protons to produce a MIP-like signal and thereby be around the minimum threshold for detection. The mean number of photons produced by protons, in CCQE interactions, in the water-based scintillator bars are calculated at each light yield from 10% to 100% that of the plastic scintillator bars in increments of 10%. The results of the first four values are illustrated in figure 3.10. It

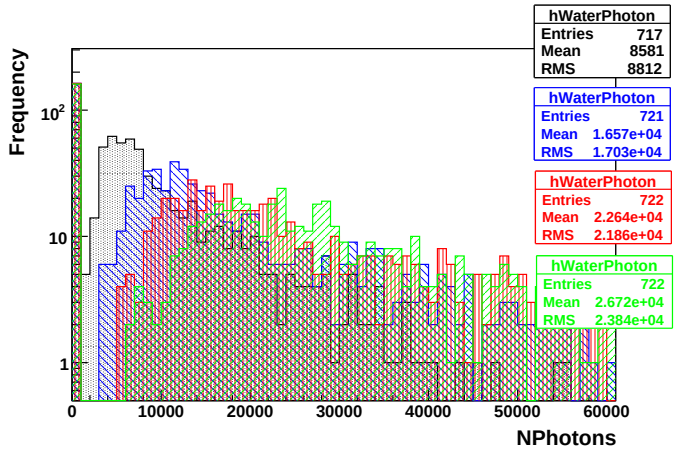

Figure 3.10: Number of photons produced by CCQE protons in water-based scintillator bars at efficiencies of 10% (black), 20% (blue), 30% (red) and 40% (green) that of plastic scintillator

can be seen that the minimum efficiency a water-based scintillator bar must exhibit when compared to a plastic scintillator bar is approximately 40% to enable further tracking of the CCQE proton.

3.5 Conclusions

A simulation of a T2K sub-detector comprising plastic scintillator bars and water-based scintillator bars has been written. A simulation of particle interactions when the efficiency of the water-based scintillator ranges from 0% to 100% that of the plastic scintillator bars is undertaken. A minimum threshold for the detection of MIPs in the detector is found by investigating the effect of muons traversing the plastic scintillator bars. This threshold is then applied to the photons created by protons in CCQE interactions in the water-based scintillator bars, as a minimum threshold for detection. It is found that the water-based scintillator bars must have an efficiency of at least 40% that of the plastic scintillator bars to provide information which may improve the sensitivity of the ND280 to CCQE recoil protons. This minimum efficiency is provided as a motivation for the rest of this thesis as such a water-based scintillator is developed. In the final chapter of this thesis this water-based scintillator will be compared with the standard plastic scintillator with a view as to whether this would be a viable upgrade to the ND280.

Chapter 4

Water-Based Scintillator Development

The motivation for developing a water-based scintillator has been justified in chapter 3. In this chapter the development of such a water-based scintillator will be described.

4.1 Introduction

Scintillation is the emission of light from a substance when a charged particle passes through it. Aromatic organics are commonly used as solvents for liquid scintillators. The molecules of aromatic compounds are characterised by benzenoid ring structures that contain unsaturated double bonds. Localised σ-electrons represent a single covalent bond and are aligned along the plane containing the atoms, linking the constituent atoms. The second bond of each unsaturated double bond represents π-electrons, in which the electron density is evenly distributed above and below the ring. These electrons are less tightly bound to their parent carbon atoms and are mobile within the molecular structure. The π-electron cloud of the aromatic ring provides a target for the particle interaction and captures the energy of the incident particle. The scintillator light arises from transitions made by these π-electrons.

Figure 4.1 illustrates the electronic levels of an organic molecule containing a π-electron system. S_0 represents the ground state and S_1, S_2, S_3 ... etc. up to the π-electron ionisation energy, I_π, represent a sequence of π-electron singlet states. Each of these electronic levels is further subdivided into vibrational sub-levels with much finer spacing. These are notated by a second suffix, e.g. S_{10}, S_{11}, etc. for the vibrational sub-levels of S_1. There is also a sequence of excited π-electron triplet states T_1, T_2, T_3 ... etc. For molecules of interest as organic scintillators the typical spacing between S_0 and S_1 is 3 - 4 eV and that between the vibrational states is of the order of 0.16 eV [96]. Since the average thermal energy associated with any mode of excitation of

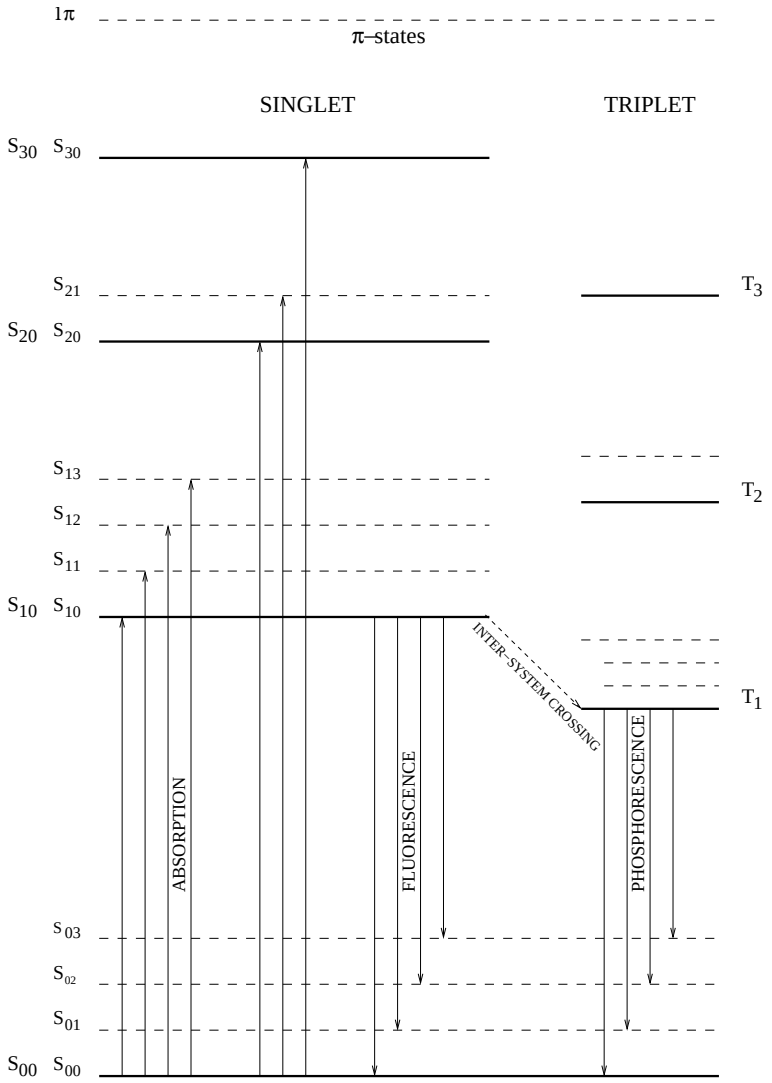

Figure 4.1: Energy Levels of an organic molecule with π-electron structure. S_0, ground state. S_1, S_2, S_3 excited singlet states. T_1, T_2, T_3 excited triplet states. S_{00}, S_{01} ... S_{10}, S_{11} ... etc. vibrational sub-levels. Adapted from [96]

a system at room temperature is 0.025eV, most molecules are in the lowest vibrational state S_{00} under normal conditions.

The kinetic energy absorbed by a scintillator from a charged particle passing through it is illustrated by upward pointing arrows. The excitation decays rapidly (on the order of picoseconds [97]) via radiationless internal conversion to the lowest excited singlet state S_1. Since any state with excess vibrational energy, such as S_{11} or S_{12}, is not in thermal equilibrium with its neighbours, it will quickly lose that vibrational energy. Since the π-electron system is weakly coupled to the molecular vibrations, internal quenching (further energy degradation below S_1) is inhibited, therefore the excited molecule emits scintillation light (labelled fluorescence). In summary, the principle scintil-

lation light is emitted in transitions between the state S_{10} and one of the vibrational states of the electronic ground state S_{00}, S_{01}, S_{02} ... etc.

Scintillators are transparent to their own fluorescence emission because nearly all the fluorescence transitions (represented by downward arrows) have a lower energy than that required for excitation, meaning that there is only small overlap between absorption and emission spectra.

In practical terms a liquid scintillator comprises in addition to an organic aromatic solvent, an aromatic fluorescent solute (or fluor) and a surfactant (a detergent type molecule that ensures proper mixing of aqueous samples). The passage of an ionising particle through the solution causes ionisation and excitation of the solvent molecules, which make up the majority of the scintillator. These ionised molecules rapidly recombine with slow electrons to yield excited solvent molecules. About 10% of the excited solvent molecules are in excited π-electronic singlet states (the remainder are in excited σ-electronic states and dissipate their energy thermally and do not contribute to the scintillator).

The excited solvent molecules undergo rapid internal conversion to the lowest excited singlet state of the solvent (as previously described). The solvent excited state does not remain stationary within the solution. In addition to thermal diffusion (Brownian motion) of the solvent and fluor molecules, there is excitation migration between the solvent molecules. The migration occurs because there is rapid formation and dissociation of excimers between adjacent excited and unexcited solvent molecules (an excimer, short for "excited dimer", is a short-lived molecule that bonds two molecules when in an electronic excited state). Via these two processes the excited solvent transports energy throughout the solution until it comes into proximity of a fluor molecule. The lowest excited singlet state of the fluor molecule is of lower energy that that of the solvent molecule. Therefore in the proximity of a fluor molecule, the excited solvent molecule undergoes solvent-fluor energy transfer to the fluor molecule. This rapidly excites the fluor molecule to its lowest excited singlet state, emitting fluorescence. If the molar concentration of the fluor is a few grams per litre then almost all of the excited solvent molecules transfer their energy to the fluor.

The fluor molecules induce a dipole moment in their solvation shell (a solvation shell is a shell of any chemical species acting as a solvent, surrounding a solute species). This allows direct transfer of energy between the scintillator and excited solvent molecules. Two fluor molecules are involved in this process: *primary fluors* which are excited to a light-emitting state by excited solvent molecules, and *secondary fluors* which capture the fluorescence energy of the excited primary fluor and re-emit it at a longer wavelength. It is vital that the emission spectrum of the primary fluor matches the absorption spectrum of the secondary fluor, and similarly that the emission spectrum of the secondary fluor matches the peak response of the photodetector used to record the scintillation light.

The intensity of the scintillation depends upon the energy of the parti-

cle dissipated in the scintillator. Particles passing through scintillators lose a small fraction of their initial energy. The rate of energy loss, $-dE/dx$, is given by the Bethe-Bloch formula, given simplistically in equation 3.1. The scintillation light is detected by photosensors, including photomultiplier tubes (PMTs), which are sensitive to weak light signals and convert them into amplified electrical pulses.

4.2 Water-based liquid scintillators

Prior motivation to create a liquid scintillator with water as the bulk solvent arises from the desire to create low cost and environmentally safe scintillator for use in large underground experiments requiring kilo-tonnes of active mass.

The optical properties of pure water are shown in figure 4.2 [98]. It is

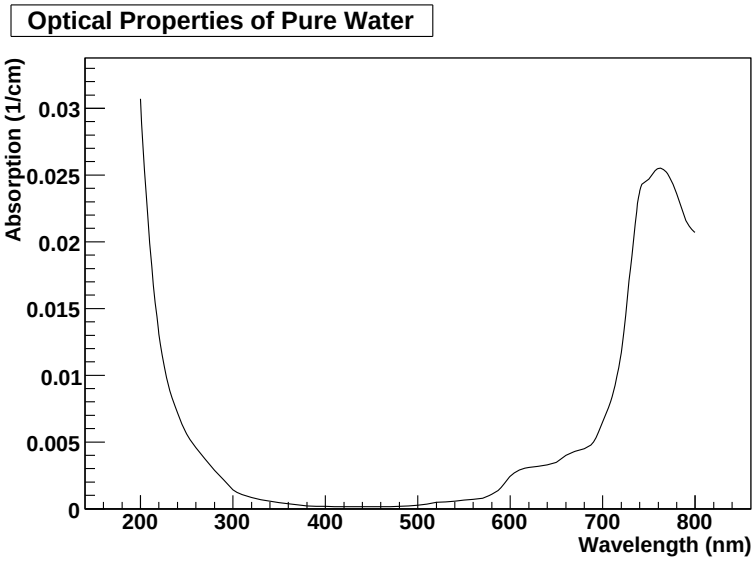

Figure 4.2: Optical properties of the clearest natural waters (200 - 800 nm). Plotted using data from [98]

seen that there is strong absorption below 200 nm with peak transmission at 440nm, well matched to the commonly used fluors PPO and POPOP emission (350 - 370 nm and 410 - 420 nm respectively [99]). Unfortunately these primary and secondary fluors are not soluble in water and when dissolved in water soluble intermediate solvents, such as alcohols or glycols the fluors generally precipitate and clump. This non-polar - polar solubility problem is ameliorated by the addition of surfactants whereby the organic "tails" form a cluster into which the organic fluor dissolves and the polar "heads" dissolve the micelle in water. This fluor-surfactant system alone must form a good scintillator and the water added will dilute or quench this mixture. Previous research [100] has produced a scintillator based upon water, surfactant, PPO and POPOP as a possible weak scintillator for bulk liquid counting at low cost

although light output is low and its suitability for high energy calorimetry unproven.

4.3 Liquid Scintillator Quicksafe A

Initial investigations identified two liquid scintillators that were developed to count tritium-bearing aqueous solutions so are therefore somewhat water tolerant. These scintillators are called Quicksafe A (QSA) manufactured by Zinsser Analytic [101] and Inflow 2:1, manufactured by IN/US Systems [102]. QSA was favoured since it exhibits a flash point of 140°C, compared to 50°C for Inflow 2:1. The flash point of a liquid scintillator is the minimum temperature at which there is sufficient concentration of evaporated liquid in the air to form an ignitable mixture with oxygen after introduction of an ignition source [97]. Another advantage of QSA is that it is biodegradable.

In the first instance various scintillator gels were investigated, the most successful being created with the use of Carbopol EZ-3 as a gelling agent (0.5%) mixed with 18% and 36% QSA concentrations in water [103]. The attraction of formulating a solid or semi-solid gel was initially that there would be less chance of leakage. However, it is laborious to create a gel that does not contain bubbles as well as being difficult to fill and drain any detector container with a gel; this avenue was not pursued further.

QSA consists of di-isopropyl naphthalene (DIPN) as the solvent with 2,5-Diphenyloxa-zole (PPO) and 1,4-bis(2-methylstyryl)benzene (bis-MSB) as the primary and secondary fluors. The density is measured at room temperature to be 0.95 ± 0.05 g/cm^3. Its high flash point classifies it as a non-hazardous liquid. It is a clear liquid with a blue tint and an aromatic odour. QSA also contains nonylphenol ethoxylate surfactants to improve the miscibility with water and mineral oil to increase the scintillator volume without decreasing the scintillation efficiency.

DIPN, molecular formula $C_{16}H_{20}$, contains two fused benzene rings in its molecular structure. See figure 4.3 for a diagram of DIPN. Chemical and

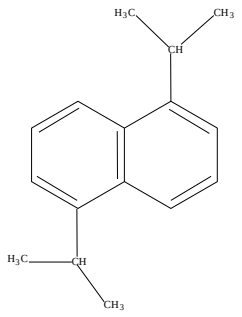

Figure 4.3: Diagram of di-isopropyl naphthalene

physical details which are of relevance for safety and detector design are

listed in table 4.1. DIPN is a clear, colourless and odourless liquid.

Description	Diisopropyl naphthalene isomers
Formula	$C_{16}H_{20}$
Molecular Weight	212.36 g/mol
Density at 20°C	0.96 g/cm^3
Melting Point	-40°C
Boiling Point	300°C
Flash Point	140°C
Ignition Temperature	450°C
Solubility in Water at 20°C	0.0002 g/l
Danger of Explosion	Does not present an explosion hazard

Table 4.1: Physical and Chemical Data of DIPN [101]

The emission spectra of pure DIPN and QSA were measured using a Jobin Yvon Flurolog Spectrophotometer (450W Xe arc-lamp, excitation at 265 nm) [104]. The transmittance through 10cm of QSA and DIPN were measured using a Transmittance Measurement Attachment added to an OL Series Spectroradiometric Measurement System [105]. The measured spectral transmittance and emission spectra are illustrated in figure 4.4. The peak in the QSA emission spectrum corresponds to the peak emission wavelength of bis-MSB of 430 nm.

4.4 Initial Investigations

Initial experimentation was undertaken to investigate how well the QSA liquid scintillator would mix with water. A table summarising the results of these investigations is given in table 4.2. In order to improve the scintillator's miscibility with water, extra surfactant is also included. Non-ionic surfactant Triton X-100 (TX100) [106] was initially chosen due to ease of availability and low cost and was found to mix well with water as well as dissolve solid powder fluors.

When deciding which concentrations to use it is important to balance water content with the dilution effect to the liquid scintillator. A standard scintillator mixture of 70% water, 25% QSA and 5% TX100 was initially chosen. This mixture contains contains 64% (by mass) of oxygen.

The liquid scintillator will be contained in 1 cm^2 long plastic cells (see section 5.6 for further detail). When the plastic of the walls is taken into account, the oxygen fraction is reduced to 49% (for polypropylene walls) and 54% (for polycarbonate walls).

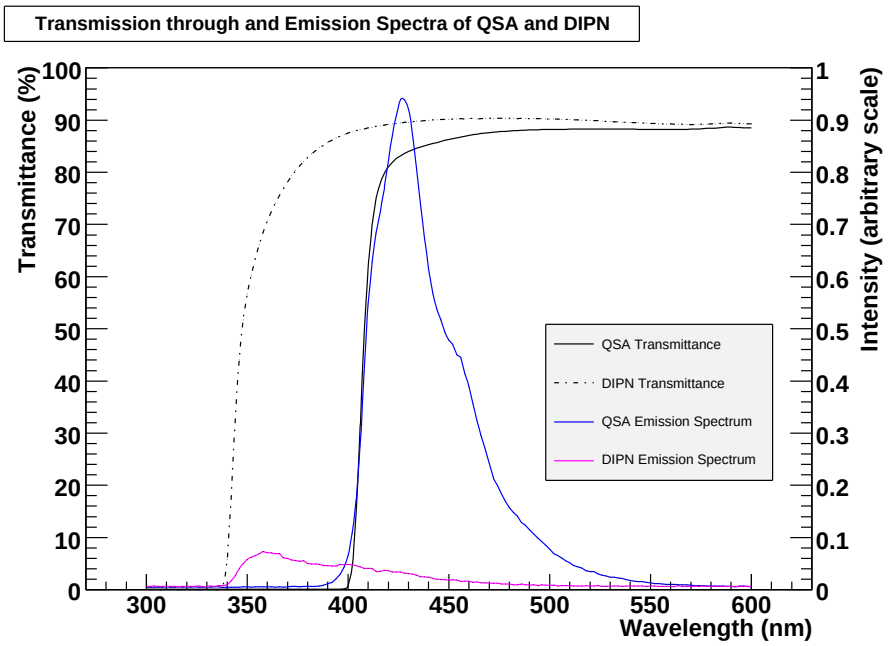

Figure 4.4: Transmittance through QSA and DIPN (left-hand scale) and emission spectra of QSA and DIPN (right-hand scale)

4.5 TRIUMF M11 Beam

TRIUMF (TRI University Meson Facility) is Canada's National Laboratory for Particle and Nuclear Physics and houses the world's largest cyclotron [107]. The M11 beamline provides low-intensity beams of protons, electrons, muons and pions of variable momenta. In collaboration with Canadian physicists this beam was utilised to test scintillator solutions with the aim of creating a water based scintillating mixture with the maximum scintillation efficiency. Two separate trips were made to Vancouver and the muon and proton beams were utilised for testing scintillators, beam choice primarily depending upon beam availability.

A schematic of the experimental setup and electronics in the beam test area is illustrated in figure 4.5. S1 and S2 represent plastic scintillator paddles that are each coupled to an XP2262 Photonis 51 mm PMT [109]. Each PMT is connected to a linear fan-out module which distributes multiple outputs to an Analogue to Digital Converter (ADC) and a discriminator. The ADC integrates and digitises the charge from the input pulse and the discriminator converts the pulse into a logic square signal, which feeds into a coincidence unit. The electronics of the setup require a coincidence signal between the PMT pulses from S1 and S2 to trigger an ADC which integrates and digitises the charge from the S3 pulse.

The central column illustrated in figure 4.5 represents the container housing the scintillator sample to be studied. The experimental configuration for

Water Concentration (by volume)	QSA Concentration (by volume)	TX100 Concentration (by volume)	Oxygen Content (by mass)	Observations
20%	55%	25%	24%	Gel
30%	35%	35%	37%	Gel
40%	30%	30%	41%	Gel
50%	50%	0%	47%	Clear fluid, separates over time
50%	40%	10%	48%	Clear fluid
60%	40%	0%	56%	Clear fluid, separates over time
60%	30%	10%	56%	Clear fluid
70%	20%	10%	65%	Clear fluid
70%	25%	5%	64%	Clear fluid
80%	20%	0%	72%	Clear fluid, separates over time
80%	10%	10%	73%	Clear fluid

Table 4.2: Observations of mixing QSA with water at various concentrations

this column drawn separately is illustrated in figure 4.6. The scintillator solution is poured into a 1 cm × 1 cm × 50 cm polypropylene cell through which a 1.5 mm diameter Kuraray Y11(200)[1] fibre passes through [110]. The structure, materials and absorption and emission spectra of the wavelength-shifting (WLS) fibres are shown in figure 4.7. The base of the cell is plugged with a plastic cap with an opening for the WLS fibre to be tightly placed. This apparatus is encased in a black light-tight tube. This end is directly coupled to the glass window of an XP2262 Photonis 51 mm PMT, with a thin layer of mineral oil for optical coupling.

A momentum selection slit only allows particles of a certain momentum to pass through to the detectors. A momentum slit selection of 400 MeV/c creates an emerging beam that consists almost exclusively of protons. At a momentum slit selection of 120 MeV/c the beam consists of approximately 60% muons, 35% electrons and 5% pions. At this fixed momentum the electrons, muons and pions travel at different velocities and can be easily identified by time of flight. A Time to Digital Converter (TDC) calculates the time between pulses in S1 and S2; a pulse from S1 starts the timing and a pulse from S2 stops it. The resulting TDC value is histogrammed over many

[1]Y11 is the name of the wavelength-shifting compound added to the fibre, and 200 is the amount added in ppm

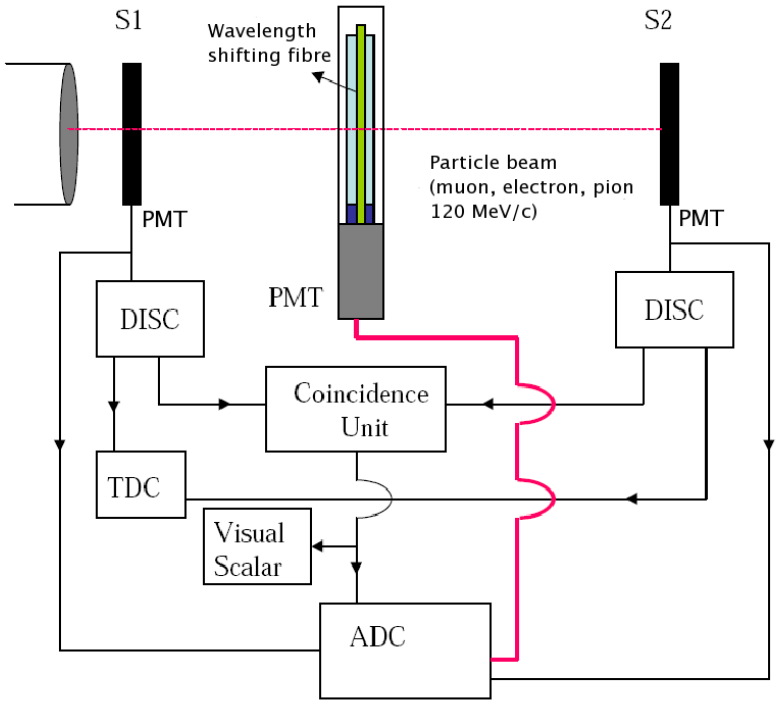

Figure 4.5: Schematic drawing of scintillator testing experimental setup and data acquisition system. Adapted from [108]

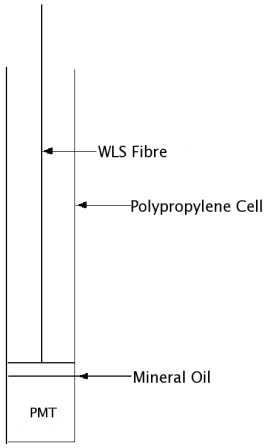

Figure 4.6: Scintillator test cell

triggers to enable the different particle species to be separated as illustrated in figure 4.8. ADC spectra are subsequently plotted for each particle type.

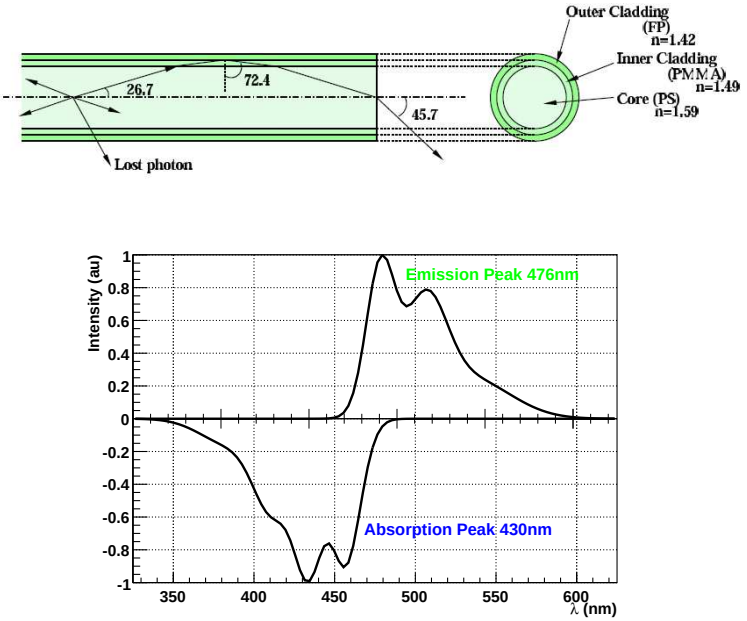

Figure 4.7: Drawing of the Kuraray Y11 WLS fibre (top) [77] and the absorption and emission spectra (bottom) redrawn from [77]

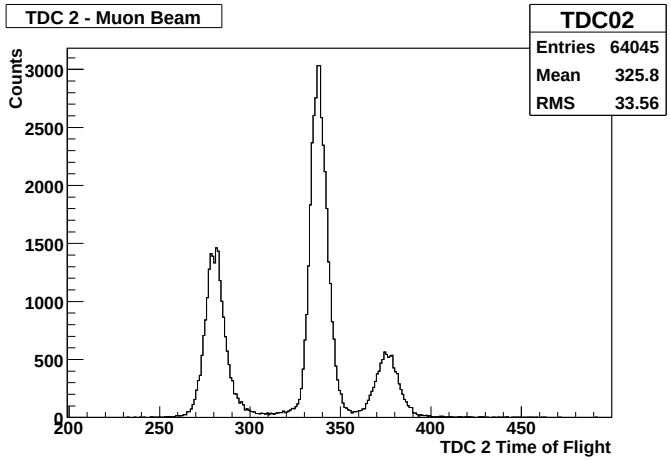

Figure 4.8: TDC spectrum which is used to perform particle identification via the time of flight between the trigger scintillators S1 and S2. From left to right, the three peaks correspond to electrons, muons and pions respectively (momentum slit selection 120 MeV/c)

4.5.1 A Typical Spectrum - Muon Beam

A typical ADC spectrum for the default scintillating mixture in the muon beam is illustrated in figure 4.9. This spectrum is plotted with a logarithmic y axis for clarity since the pedestal peak is much larger than the signal peak.

Peak A represents this pedestal peak, which arises because the scintillator

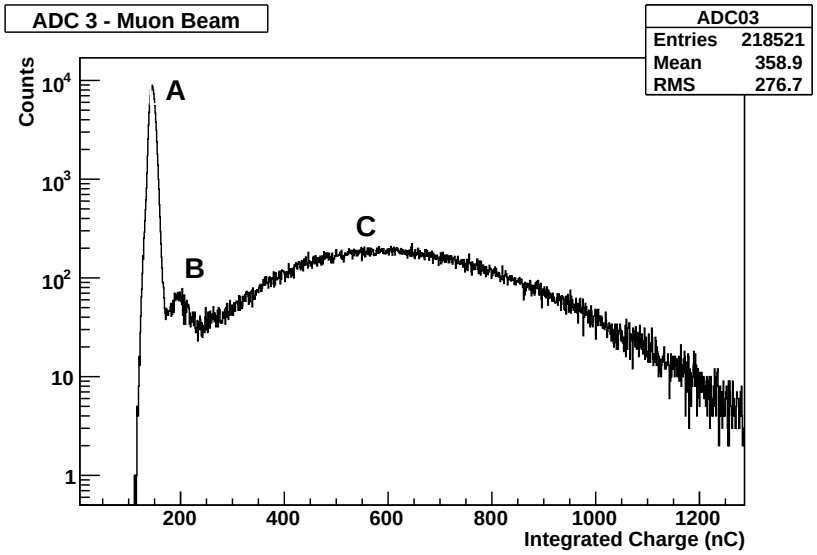

Figure 4.9: A typical spectrum of default scintillating mixture in muon beam

paddles are wider than the scintillator sample cell. This allows coincidences between S1 and S2 to occur when no charged particle has passed through the scintillator in S3. Peak B is the single photoelectron (s.p.e.) peak, caused by dark current in the PMT. Peak C is the scintillation signal from the scintillator being tested.

The data are analysed by fitting a Gaussian to each of the peaks for each scintillator test sample. The distance between peaks A and B determines the number of ADC channels per photoelectron. The distance between A and C divided by the number of ADC channels per photoelectron provides the average number of photoelectrons (Npe) per beam particle for the scintillator sample. The greater the Npe the more efficient the scintillator sample.

Successive samples of the standard scintillator mixture of 70% pure water, 25% QSA and 5% TX100 were tested in the muon beam. The Npe averaged over 5 runs gives a mean value for the standard scintillator mixture in the muon beam of:

$$\text{Npe} = 10.5 \pm 0.3 \tag{4.1}$$

4.5.2 A Typical Spectrum - Proton Beam

A typical spectrum of the default scintillating mixture in the proton beam is illustrated in figure 4.10. This spectrum is plotted with a logarithmic x axis to separate the pedestal peak (left hand peak) and the signal peak (right hand peak). Also included in this plot is are the two Gaussian fits to the pedestal and signal peaks.

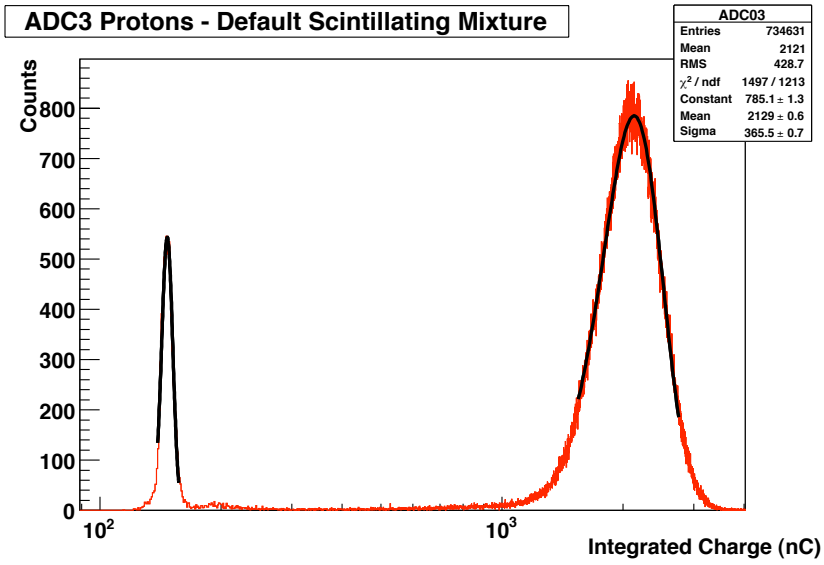

Figure 4.10: A typical spectrum of default scintillating mixture in the proton beam

Successive samples of the standard scintillator mixture of 70% pure water, 25% QSA and 5% TX100 were tested in the proton beam. The Npe averaged over 5 runs gives a mean value of:

$$\text{Npe} = 41.04 \pm 1.0 \tag{4.2}$$

4.6 Beam Tests 1: Improvements to Quicksafe A

The first attempt at improving the efficiency achieved from the liquid scintillator QSA was to formulate QSA from the raw ingredients and subsequently change the concentrations of fluors in the scintillator solution.

4.6.1 Method

The first test was performed with a sample made of 70% water, 25% QSA and 5% TX100. Thereafter the 25% scintillating portion of this nominal mixture was altered by either dilution with water or addition of extra primary and secondary fluors. Additionally, a "home brew" of QSA was formulated from the raw ingredients, which consist of approximately (percentages by volume): 47% DIPN, 43% non ionic surfactant blend, 8% mineral oil, 1% PPO and 0.1% bis-MSB. The ingredients were mixed together in a beaker, on a hot plate and maintained at a constant temperature and stirred with magnetic stirrers. Subsequently extra concentrations of the secondary fluor bis-MSB were added.

4.6.2 Results

The determined efficiency of the standard cocktail (labelled fluor concentration 100%) and standard cocktail with additional or reduced concentrations of fluors are illustrated in figure 4.11. These results were taken utilising a muon beam. The change in efficiency when extra amounts of secondary fluor are added is illustrated in figure 4.12.

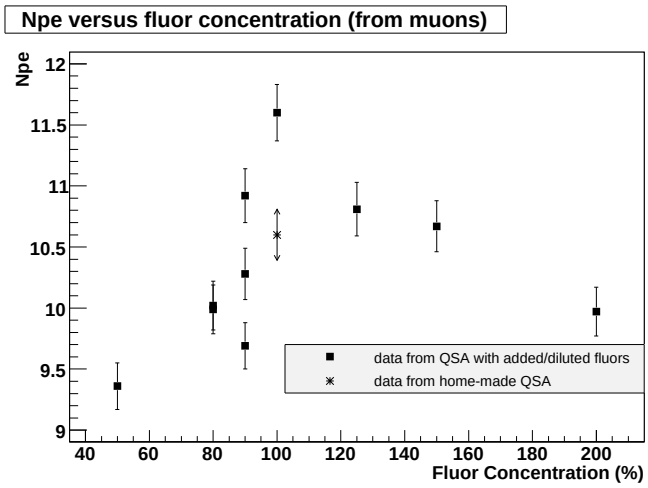

Figure 4.11: Results from testing scintillator samples with TRIUMF beam: Npe versus fluor concentration (from muons) relative to standard QSA

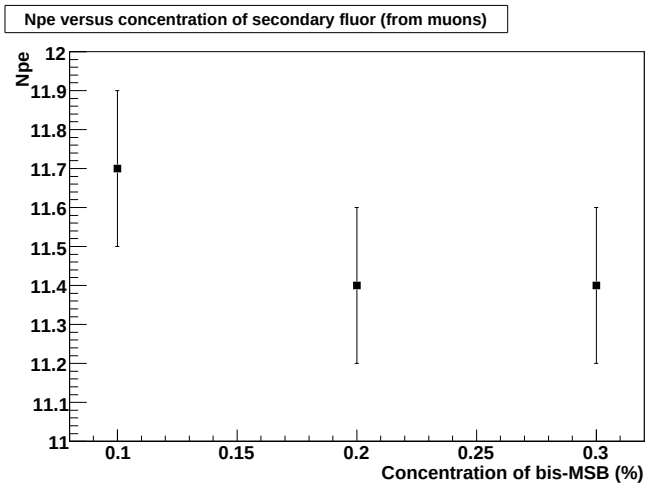

Figure 4.12: Results from testing scintillator samples with TRIUMF beam: Npe versus concentration of additional secondary fluor (from muons)

4.6.3 Investigation into Experimental Uncertainties

Although utmost care is taken to repeat each experimental run with the greatest accuracy there are many areas where uncertainties can arise. For example a home-made QSA sample with undissolved fluors was tested in the beam and this sample gave lower efficiency results when compared with a sample where the fluors had been completely dissolved. It is therefore imperative that the samples are well heated and mixed, and allowed to cool fully before testing.

Other sources of error arise in removing and replacing the test cell. A laser pointer is used to ensure the cell is correctly aligned within the beam and the setup is rigid to maintain as constant position as possible. The temperature can also effect the efficiency of the scintillator. During summer experimentation the temperature at the start and end of each run was recorded and the air-conditioning unit was switched on for each run in an attempt to maintain the constancy of the temperature.

In order to investigate the possible sources and magnitude of any errors the muon ADC data from two separate runs (runs that had occurred on different days so involved re-filling and replacing the apparatus) of the same scintillator sample were repeatedly analysed. The centroids for peaks A, B and C were re-measured 10 times. The overall error on the average number of photoelectrons (Npe) per beam particle for the scintillator sample was determined to be 2%. Therefore the trends indicated in figures 4.11 are significant above errors.

4.6.4 Conclusion

As illustrated in figure 4.11, the most efficient scintillator was found to be 100% fluor concentrations i.e. standard "off-the-shelf" QSA. This scintillating mixture of 70% water, 25% QSA and 5% TX100 gave the highest value of the average number of photoelectrons (Npe) per beam particle for that sample significant above experimental errors. Further dilution or addition of fluors consistently reduced the efficiency of the scintillator solution. Furthermore when the 25% active scintillator portion was formulated from the raw ingredients of QSA (a "home-brew") the efficiency was reduced by almost 9%. The addition of extra concentrations of bis-MSB actually reduces the efficiency of the scintillator solution by a few percent, possible caused by difficulties in dissolving the scintillator fluor.

4.7 Beam Tests 2: Alternative Solvents and Fluors

A full list of fluors and their absorption and emission characteristics is given in table 4.3. Since QSA contains DIPN as the solvent, PPO as the primary fluor

Ingredient	Peak Absorption (nm)	Peak Emission (nm)
DIPN		358-360
QSA		427
1-MN	285	320-340
Xylene	265-275	285-290
PPO	300-320	350-370
BPO	325	390
bis-MSB	345-350	420-424
POPOP	360-365	410-420
TFP	360	430-440
Y11 fibres	430	470

Table 4.3: Absorption and Emission Peak Wavelengths for scintillator ingredients [99]

and bis-MSB as the secondary fluor, from the peak emission and absorption wavelengths as given in table 4.3, it is apparent that this primary fluor is not playing the most crucial role within the QSA. It will however contribute to the overall scintillation efficiency. It can also be seen that the emission spectrum of DIPN is well overlapped with the low frequency band in the absorption spectrum of secondary fluor 1,4-Di-[2-(5-phenyloxazolyl)]-benzene (POPOP), creating favourable conditions for the transfer of electron excitation energy from the solvent to the fluor.

There is a large overlap between the emission spectrum of scintillator solvent 1-methylnaphthalene (1-MN) and the absorption spectrum of PPO. The absorption spectrum of TFP is well matched to the emission spectrum of PPO and DIPN. The emission spectrum of TFP is also well matched to that of the Kuraray WLS fibres.

In summary there are a number of promising solvent and fluor combinations which could be formulated and their efficiency tested. The most promising combinations are detailed in table 4.4.

	Contents
1	DIPN, PPO, POPOP
2	DIPN, TFP
3	1-MN, PPO, TFP
4	1-MN, BPO, TFP

Table 4.4: Scintillator solvent and fluor combinations that are well matched for promising scintillation efficiency

4.7.1 Method

In the case of combination 1 (DIPN, PPO, POPOP) two scintillator samples are tested, the first comprising (by mass) 47% DIPN, 43% surfactant blend 1% PPO, 0.1% POPOP with 8% mineral oil and the second replacing the mineral oil with 8% isopropanol (IPA). This test is attempted since IPA is a scintillator solvent and also provides compatibility with water particularly in the presence of a surfactant [111].

Combinations 2, 3 and 4 are formulated to contain (by mass) 47% DIPN or 1-MN, 43% surfactant, 8% mineral oil or IPA, 1% primary fluor (PPO or BPO) and 0.1% secondary fluor (TFP). They are then mixed with as much water as can be tolerated without clouding or separation and TX100 is added to try to improve the miscibility with water. The maximum water content successfully added and the corresponding oxygen content (by atomic mass) of each formulation is illustrated in table 4.5.

Scintillator Ingredients	Water Content (by volume)	Oxygen Fraction (by atomic mass)
Standard Cocktail	70%	0.49
DIPN/PPO/POPOP/mineral oil	70%	0.48
DIPN/PPO/POPOP/IPA	18%	0.17
1-MN/BPO/TFP/IPA	40%	0.31
DIPN/TFP/mineral oil	25%	0.21
1-MN/PPO/TFP/mineral oil	60%	0.43

Table 4.5: Comparison of water content (by volume) and oxygen content (by atomic mass) for different scintillator solvent/fluor combinations

4.7.2 Results

The efficiency results for the scintillator solvent and fluor combinations as measured in the TRIUMF beam are given in table 4.6.

4.7.3 Conclusion

Although the DIPN/PPO/POPOP/mineral oil combination is promising from an absorption and emission overlap perspective and its high oxygen content, it actually exhibits a much lower efficiency when measured in the proton beam than the standard cocktail. This is likely caused by the difficulties in synthesising scintillators from raw ingredients in the laboratory, such as difficulties in dissolving and mixing fluors and mixtures staying in solution. When mineral oil is replaced by IPA the mixture becomes incredibly water abhorrent.

Scintillator Ingredients	Beam Type	Particle Momentum	Npe
Standard Cocktail	proton	400 MeV/c	41.4 ± 1.0
Standard Cocktail	muon	120 MeV/c	10.1 ± 0.2
DIPN/PPO/POPOP/mineral oil	proton	400 MeV/c	22.2 ± 0.1
DIPN/PPO/POPOP/IPA	proton	400 MeV/c	93.9 ± 0.1
1-MN/BPO/TFP/IPA	muon	120 MeV/c	12.5 ± 0.1
DIPN/TFP/mineral oil	muon	120 MeV/c	only single photo electron peak visible
1-MN/PPO/TFP/mineral oil	muon	120 MeV/c	11.8 ± 0.1

Table 4.6: Efficiency results of different scintillator formulations

The combination of 1-MN/BPO/TFP/IPA and 1-MN/PPO/TFP/mineral oil both display a greater efficiency in the muon beam than the standard cocktail. However they do both also have a reduced oxygen content. The combination of DIPN/TFP/mineral oil was promising due to high overlap between the emission wavelengths of DIPN and absorption wavelengths of TFP, together with a high oxygen content. The efficiency results in the muon beam were however disappointing, in that the most dominant feature was the one single photoelectron peak, with no discernible further peaks. If further beam time were possible it would have been interesting to investigate whether the addition of a primary fluor such as PPO could have improved this measurement. In summary the standard cocktail is still the preferred solution because of its exhibited efficiency in the TRIUMF beam combined with its oxygen content.

4.8 Beam Tests 3: Alternative Solutions

Five liquid scintillator samples were procured from the Institute for Single Crystals, Ukraine [112]. The contents of these samples are displayed in table 4.7. 1-MN ($C_{11}H_{10}$) and xylene (C_8H_{10}) are solvents and act as the scintillator base. Unfortunately xylene is generally considered unacceptable in modern scintillators due to its low flashpoint of 25°C [113]. The xylene-based samples also chemically attacked the WLS fibres and were therefore discounted. The flashpoint of 1-MN is 82°C [114]. Isopropanol is added as it provides compatibility with water in the presence of a surfactant. Neonol is a non-ionic surfactant. BPO (2,5-(4-Biphenylyl)-1,3-oxazole) is a primary fluor and TFP (1,3,5-Triphenylpyrazole) is a secondary fluor.

The absorption and emission spectra of the constituents have been given

	Contents
A	1-MN, Isopropanol, Neonol, BPO
B	Xylene, Isopropanol, Neonol, BPO
C	1-MN, Isopropanol, Neonol, TFP
D	Xylene, Isopropanol, Neonol, BPO, TFP
E	Isopropylnaphthalene, Isopropanol, Neonol, BPO

Table 4.7: Contents of Ukrainian Scintillators

in table 4.3. The emission spectra of the Ukrainian scintillator samples, measured using a Jobin Yvon Flurolog Spectrophotometer (450W Xe arc-lamp, excitation at 265 nm) are shown in figure 4.13. The peaks of the emission spectra of scintillators A, B and E correspond to the peak emission wavelength of BPO and those of curves C and D to the peak emission wavelength of TFP. The measured transmittance through each sample is illustrated in figure 4.14.

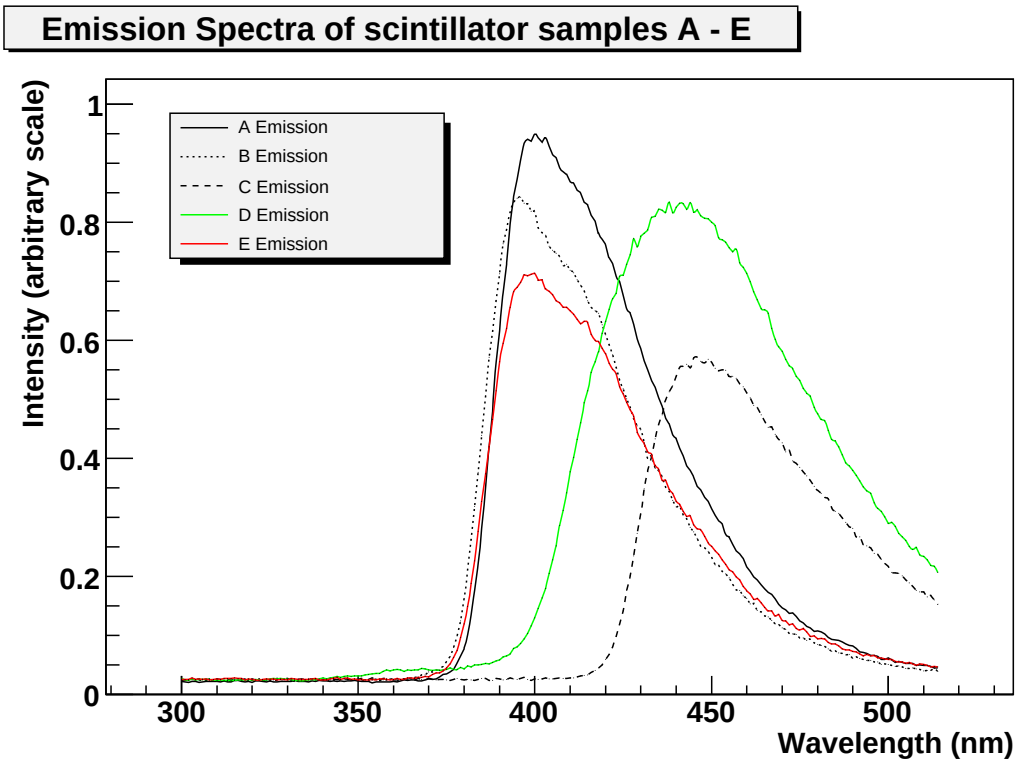

Figure 4.13: Emission Spectra of scintillator samples procured from the Institute for Single Crystals, Ukraine, A - E

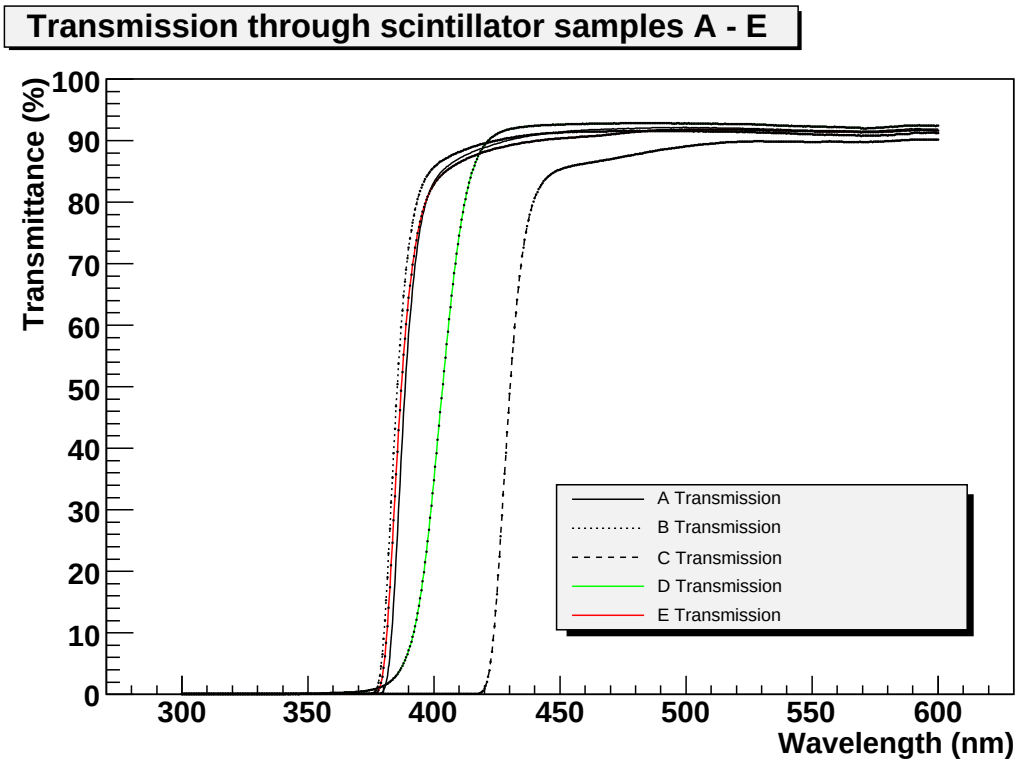

Figure 4.14: Transmission through scintillator samples A - E

4.8.1 Method

These scintillator samples were difficult to successfully mix with water. Repeated attempts in the laboratory with varying methods, heating, stirring, adding alternative surfactants could achieve on average only 25% water solutions, before the mixtures turned viscous or cloudy or stratified.

Samples A, C and E were nonetheless tested in the TRIUMF proton beam, at 100% scintillator concentrations, then re-tested with water added in 10% concentrations, up to the maximum concentration possible.

4.8.2 Results

The results of the beam tests for successive concentrations of water for each scintillator sample are illustrated in figure 4.15. Those samples which show an improvement in efficiency when compared to the standard scintillator mixture are scintillator A diluted with 20% water, scintillator C diluted with 10% water and scintillator E diluted with 30% water. A comparison of the oxygen content is given in table 4.8.

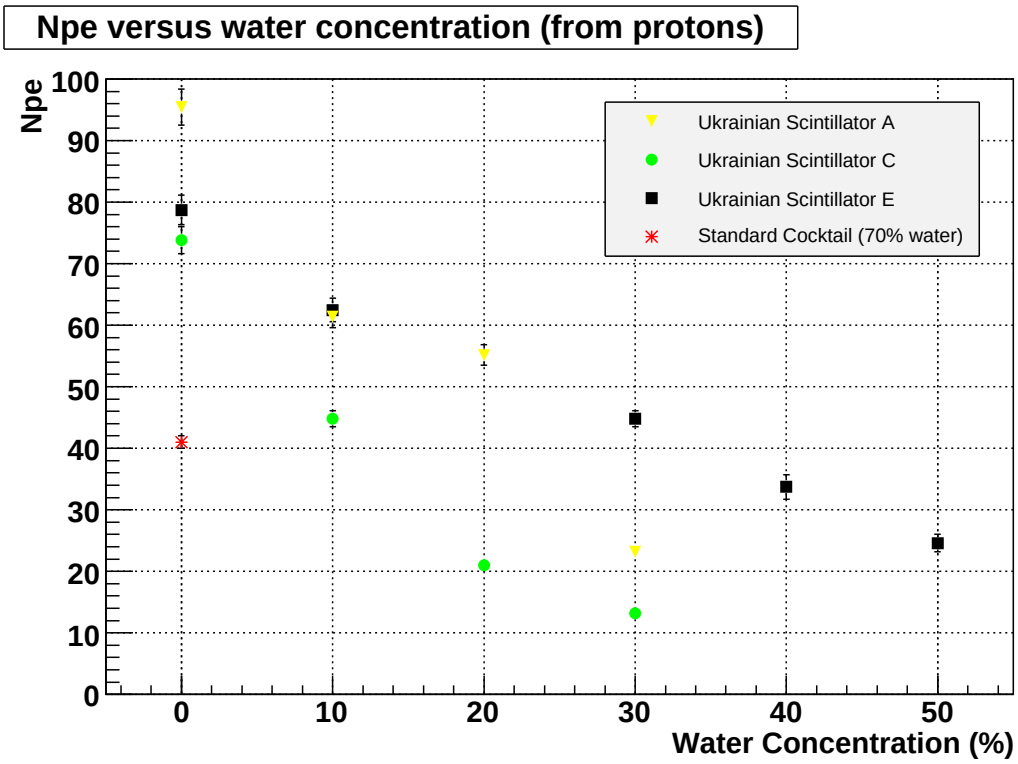

Figure 4.15: Measured number of photoelectrons for Ukrainian scintillator samples A, C and E with increasing levels of water concentration, tested in the proton beam

Scintillator	Water Content (by volume)	Oxygen Fraction (by atomic mass)
Standard Cocktail	70%	0.49
A	20%	0.19
C	10%	0.12
E	30%	0.25

Table 4.8: Comparison of water content (by volume) and oxygen content (by atomic mass) for Ukrainian scintillator samples that are more efficient that standard cocktail (containing 70% water)

4.8.3 Conclusion

It is extremely difficult to mix the Ukrainian scintillator samples with water. Furthermore two of the samples are unsuitable as they chemically attack the WLS fibre. The remaining samples were tested in a proton beam at 100% scintillator concentrations, then re-tested with water added in 10% concen-

trations. As can be seen in figure 4.15 at 20% water levels the Ukrainian scintillator sample A is less efficient than the standard cocktail (containing 70% water solution) and drastically reduced oxygen content. The same effect is observed in sample C at 10% water concentration and sample E with 30% water concentration. These scintillator solutions are therefore not an improvement to the standard scintillator mixture.

4.9 Beam Tests 4: An Aqueous Scintillator with Fluor-Containing Nanosuspensions

4.9.1 Introduction

A novel idea for a water-based liquid scintillator is an aqueous suspension of fluor-containing polystyrene nanoparticles [115]. To make such a suspension primary fluor PPO and secondary fluor bis-MSB are dissolved into styrene (C_8H_8). Subsequent polymerisation of this styrene phase yields polystyrene nanoparticles containing the entrapped fluors. They make up the oil phase of an oil-in-water microemulsion, also containing water and surfactant Brij78 ($C_{18}H_{37}(OCH_2CH_2)_{20}OH$) and co-surfactant 1-pentanol ($C_5H_{11}OH$). These surfactants align at the interface between the nanoparticle and the aqueous medium, providing a surface charge repulsion that maintains the nanoparticles in a suspended state.

The nanoparticle suspension qualifies as non-hazardous waste, as defined by the United States Environmental Protection Agency for toxicity, characteristic leaching, volatile organic compounds, semi-volatile organic compounds, metals, reactivity, pH and ignitibility. Furthermore the suspension exhibits low chemical reactivity. Its flashpoint is greater than 93°C. The nanosuspension is an attractive alternative to the standard cocktail due to its inertness and ability to stay in solution. It also has 50% water content.

4.9.2 Emission Spectrum of the Nanosuspension

The emission spectrum of the nanosuspension was measured using a Jobin Yvon Flurolog Spectrophotometer (450W Xe arc-lamp, excitation at 265nm), illustrated in figure 4.16. The peak at 430 nm corresponds to the peak emission wavelength of the secondary fluor, bis-MSB.

4.9.3 Transparency of Nanosuspension

The nanoparticles' average diameter varies between 30 nm to 100 nm with an approximate interparticle distance of 165nm [116]. Since these dimensions are smaller than the wavelength of visible light, it is naturally expected that the nanosuspension be clear and transparent. In actual fact the nanosuspension is opalescent and turbid, an effect probably caused by Rayleigh scattering.

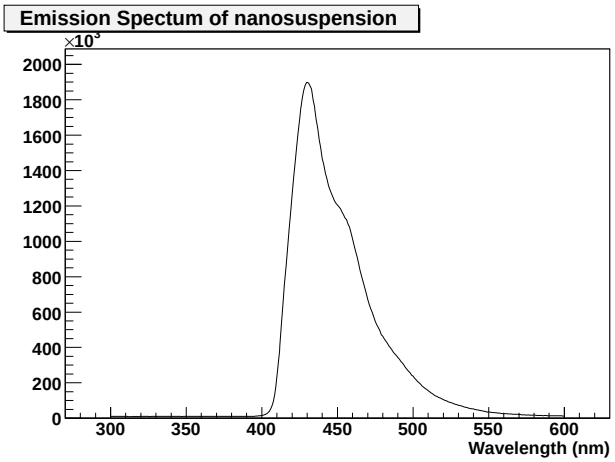

Figure 4.16: Emission spectrum of Nanosuspension

An idea to reduce scattering and create a clear solution is to match the refractive indices of the constituent ingredients [117]. This will allow light to transmit throughout the nanosuspension without refraction therefore improving clarity. Styrene exhibits the highest refractive index, n $\approx$ 1.55 [118]. The refractive indices of the surfactants are around n $\approx$ 1.40 [119], whereas that of pure water is n = 1.33 [120]. Various additives could increase the refractive indices of these water phases to match that of the styrene. Efforts were made by adding butylene glycol (n = 1.44) [117] and sucrose solution (n = 1.49) [120]. Unfortunately the additions of 25%, 50% and 100% (by volume) of glycol and sugar solution did not improve the transparency of the nanosuspension. This is evident when attempting to measure the transmission through the nanosuspension. Illustrated in figure 4.17 is the transmittance graph created in the same way as discussed in section 4.3. Excessive scattering means that the incident beam cannot transmit through the sample, even when the nanosuspension is diluted by the same volume with glycol and sugar solution.

4.9.4 Beam Tests of Nanosuspension

The spectrum of 100% nanosuspension is illustrated in figure 4.18 (top). There are two visible features, which could possibly represent the first and second photoelectron peaks. However these peaks are so slight that it is not possible to fit the spectrum to deduce a average number of photoelectrons per beam particle.

For comparison, a typical spectrum of the default scintillating mixture in the proton beam is shown in figure 4.18 (bottom). As described in subsection 4.5.1, peak A represents the pedestal peak, peak B the single photoelectron peak and peak C the signal caused by scintillation light created in the solution being tested. For the example spectrum shown in figure 4.18 the number of

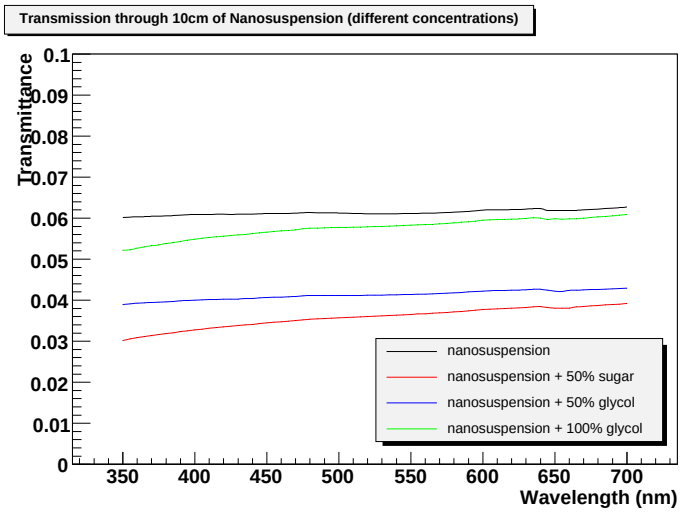

Figure 4.17: Transmittance through 10cm of nanosuspension at varying concentrations

photoelectrons, Npe = 41.46 ±0.03.

Attempts were made to improve the efficiency of the nanosuspension by adding butylene glycol and sucrose solution in concentrations of 25%, 50% and 100% by volume. These tests could not appreciably increase the efficiency of the nanosuspension. As an example the spectrum of nanosuspension plus 50% sucrose solution (by volume) is illustrated in figure 4.19. For this mixture Npe = 2.1 ± 0.05. The Gaussian fits used to calculate this Npe value are shown for clarity.

4.9.5 Summary of Nanosuspension Results

The results are summarised in table 4.9.

Sample	Npe
100% Nanosuspension	no fit possible
Nanosuspension + 25% sucrose solution (by volume)	1.8 ± 0.03
Nanosuspension + 50% sucrose solution (by volume)	2.1 ± 0.05
Nanosuspension + 25% glycol (by volume)	1.8 ± 0.06
Nanosuspension + 100% glycol (by volume)	1.8 ± 0.04
Standard cocktail	41.5 ± 0.04

Table 4.9: Npe values for nanosuspension samples compared with the default scintillating mixture

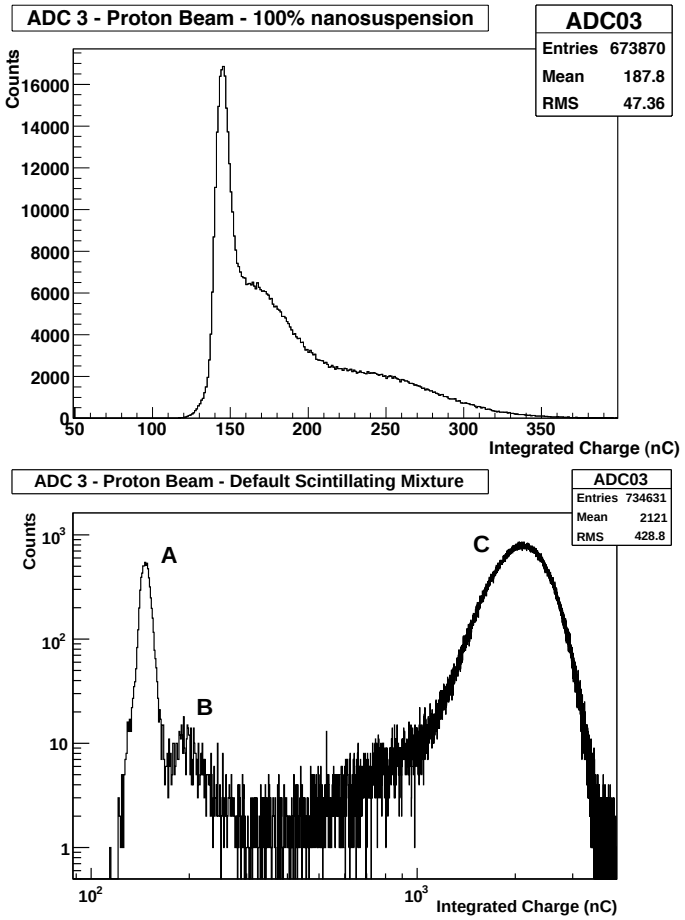

Figure 4.18: Spectrum of 100% nanosuspension in proton beam (top) and typical spectrum of default scintillating mixture in proton beam (bottom)

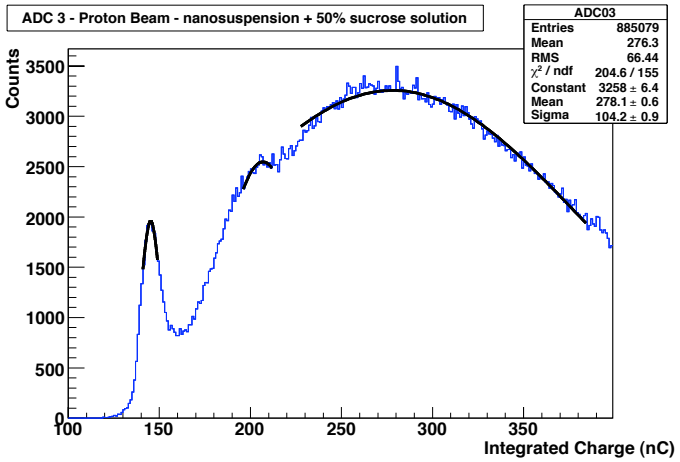

Figure 4.19: Spectra of nanosuspension plus 50% sucrose solution in proton beam. The gaussian fits are illustrated.

4.9.6 Conclusion

When compared with the standard scintillating mixture, the nanosuspension is too inefficient for the purpose of the T2K experiment. Although results of successful application of the nanosuspension for liquid scintillation counting have been presented elsewhere [115], the lack of success in this experiment can be attributed to the setup required by this experiment i.e. the long thin cells and single WLS fibre carrying the light approximately 2 m to the PMTs means that due to scattering the nanosuspension is too inefficient. Addition of sucrose solution and glycol of 25%, 50% and 100% by volume also does not appreciably improve the efficiency nor transparency.

4.10 Conclusion

A suitable water tolerant liquid scintillator, Quicksafe A (QSA), has been identified. Experiments revealed a stable water-containing mixture of 70% water, 25% QSA and 5% extra surfactant TX100. Initial investigations tried to improve upon the scintillation efficiency of this standard solution by the addition or dilution of fluors to the ingredients of QSA. It was found that standard QSA with no extra fluors was the most efficient solution. Subsequently the type of solvents and fluors were changed to try to choose solvent and fluor combinations that were well matched for good energy transfer within the scintillator. Once more standard QSA solution was found to be the most effective.

Alternative scintillator solutions from another source were also tested and were found not to mix well with water and also not to match the efficiency of the standard solution when mixed. Finally an alternative type of solution, known as a nanosuspension, was tested. Due to transparency issues this scintillator was found to exhibit a much drastically reduced efficiency in the T2K experimental setup.

The ultimate conclusion of these studies is that standard QSA cannot be improved upon for the purposes of this experiment. The scintillator solution will consist of 70% water, 25% QSA and 5% TX100.

Chapter 5

Design Tests of Active Water Prototype Detector

In the previous chapter a scintillator solution consisting of 70% water, 25% QSA and 5% TX100 was developed. In this chapter observations and tests performed on this solution will be described. In the second part of this chapter the mechanical structure necessary to house the solution within the T2K experiment will be addressed as well as other experimental challenges explored relating to the design and construction of such a detector.

5.1 Observations of Quicksafe A and DIPN

40 ml samples of QSA and DIPN were placed in ovens at different temperatures, one sample of each exposed to light and one made light-tight. The oven was modified to heat to 50°C, 65°C, 80°C and 95°C. In all these tests QSA yellowed faster than DIPN. The rate and degree of yellowing increased with temperature. Proximity to the heating bulb catalysed the yellowing of DIPN but both light exposed and light-tight samples of QSA turned the same shade of yellow.

To investigate the effect of the heating bulb further samples of light exposed and light-tight samples of QSA and DIPN were placed beneath a 100 W bulb. After 35 days both the QSA samples remained clear, the light-tight sample of DIPN remained clear and the light exposed DIPN sample discoloured yellow. These results suggest that the yellowing of QSA is catalysed by heat and the yellowing of DIPN is catalysed by light.

5.2 Observations of Default Scintillating Mixture

40 ml samples of the scintillator mixture were placed in a 25°C and 37°C temperature controlled room as well as one sample at room temperature.

The sample at room temperature maintained its clear blue consistency for an observation period of over 200 days. Similarly the sample maintained at 25°C stays as a clear blue liquid during this same time period. The sample kept at 37°C became a semi-solid and turbid off-yellow coloured gel.

A further sample was placed beneath a 100W bulb for a period of one month. This sample also discoloured yellow and turbid. This was likely caused by the heat from the bulb heating the samples and having the same effect as the hot oven.

In summary, maintaining the scintillator mixture long-term at 25°C does not cause visible degradation.

5.3 Mould Inhibitor Tests

Long term observations of the default scintillating mixture revealed black and white fungal growths. They were identified as "Stachybotys" and "Cladosporium herbarium" [121]. These are both common fungi that thrive in the carbon and nitrogen rich environment provided by the scintillator solutions. It is the addition of water that causes this mould growth; long term samples of pure QSA or DIPN never grow mould, even after over 700 days observation.

Each sample contained 70% water (by volume). Two types of water were used: deionised (DIW) and pure water (PW). Pure water was delivered from an Elga Purelab Option water filtration unit [122] fitted with pre-treatment, reverse osmosis, UV lamp and ion exchange cartridges. The resistivity of this water supply is constantly above 15 MΩcm. Deionised water is obtained from a similar Elga Purelab Option 3 [122] with resistivity above 18.2 MΩcm.

The samples contained 25% (by volume) of QSA and 5% (by volume) of surfactant Triton-X 100 (TX100). The following biological inhibitors were added at a concentration of 1000 ppm: Propanoic Acid (PA), Mould Preventer (MP), Germall Plus (GP), Sodium Azide (SA), Cadmium Nitrate (CN), Copper Sulphate (CS) and Methyl Paraben (PB). These are all well known mould and bacterial inhibitors; propanoic acid is used as a preservative in food as methyl paraben is widely used as a preservative in the cosmetics industry. Germall Plus is a widely used vegetable derived preservative. Sodium azide is a broad spectrum biocide commonly used to preserve cultures but is explosive and poisonous. There has been evidence found that growth of fungi can be prevented by addition of metal salts [123].

30 ml samples of the water/QSA/TX100/inhibitor solutions were made light-tight and placed at room temperature and in an oven at approximately 35°C. The temperature in the oven depended upon proximity to the heating bulb. After between 75 and 96 days these samples were moved to a 37°C temperature controlled room. Further samples of each solution were also placed in a 25°C temperature controlled room.

5.3.1 Results

Room Temperature The following samples grew black and white coloured mould within the first 20 days: DIW, PW, DIWMP, DIWGP, DIWPB, PWPB. The remaining samples are still mould free after approximately 120 days: PWMP, PWGP, PWSA and both water type samples of PA and CN. The DIWSA sample has formed a semi-solid gel. The CS samples are discoloured blue/green.

Elevated Temperature Samples - 25°C DIW, PW, DIWMP, DIWGP, DIWPB and PWPB samples show a small amount of white feathery mould.

All other samples were mould free and continue to be mould free after 22 days of elevated temperature. When the samples are removed from the oven they are remain clear solutions. However PW, PWPA, DIWSA, PWSA, DIWCS, samples contain minute white speck-like particles, which clear after 1 day of cooling. After 50 days exposure PWPA and DIWPA exhibit spores of dark mould.

Elevated Temperature Samples - 37°C When samples are maintained at 37°C they are all turbid and viscous. After the samples are allowed to cool the majority of samples revert to normal viscosity except for PWPA, PWMP and DIWGP which maintain a slightly increased viscosity and PWMP, PWCS, DIWCS, PWCN, DIWSA and PWSA which maintain turbidity and viscosity. The cooling and clearing takes a number of days.

The following sample is still mould free: PWGP. Mould is present in: PW, DIWMP, DIWGP, DIWPB. The following samples form gels or turbid solutions: DIW, DIWPA, PWPA, PWMP, DIWSA, PWSA, DIWCN, PWCN, DIWCS, PWCS and PWPB.

A summary of the mould observations is given in table 5.1.

5.3.2 TRIUMF Beam Tests of Mould Inhibitors

Due to time constraints not all the inhibitor samples could be tested in the TRIUMF beam. For details of the TRIUMF beam and the experimental method refer to section 4.5. Scintillator samples with added Germall Plus, Methyl Paraben and Copper Sulphate were tested and the results are shown in table 5.2.

5.3.3 Conclusion

The only sample that really survived the 37°C exposure was PWGP. As has been noticed in other long term temperature tests this temperature is too

Water/Biological Inhibitor	Room Temperature	25°C	37°C
DIW	mould present	mould present	gel (slight discolouration)
PW	mould present	mould present	mould present
DIWPA	**mould absent**	mould present	gel (slight discolouration)
PWPA	**mould absent**	mould present	gel (slight discolouration)
DIWMP	mould present	mould present	mould present
PWMP	**mould absent**	**mould absent**	gel (slight discolouration)
DIWGP	mould present	mould present	mould present (slight discolouration)
PWGP	**mould absent**	**mould absent**	**mould absent** (slight discolouration)
DIWSA	gel	**mould absent**	gel (yellow discolouration)
PWSA	**mould absent**	**mould absent**	turbid fluid
DIWCN	**mould absent**	**mould absent**	gel (slight discolouration)
PWCN	**mould absent**	**mould absent**	gel (dark discolouration)
DIWCS	**mould absent**	**mould absent**	gel (dark brown discolouration)
PWCS	**mould absent**	**mould absent**	gel (dark brown discolouration)
DIWPB	mould present	mould present	mould present
PWPB	mould present	mould present	gel (slight discolouration)

Table 5.1: Summary of mould inhibitor testing observations

high for the scintillator solutions to survive and they turn into turbid and gel-like solutions. At 25°C (and room temperature) the most successful samples are PWMP, PWGP, PWSA, DIWCN and PWCN and DIWCS and PWCS.

Since cadmium compounds are carcinogenic and highly toxic and sodium azide is also highly toxic, they were deemed unsuitable for use in the T2K experiment due to Health and Safety reasons. Of the remaining successful samples GP, MP and CS were tested in the TRIUMF beam and Germall Plus ex-

Inhibitor (1000 ppm)	Beam Type	Npe
Germall Plus	proton	41.04 ± 1.0
Germall Plus	muon	10.05 ± 0.3
Methyl Paraben	proton	27.5 ± 0.1
Methyl Paraben	muon	6.7 ± 0.1
$CuSO_4$	proton	37.1 ± 0.1
$CuSO_4$	muon	7.0± 0.1

Table 5.2: Results of mould inhibitor tests in the TRIUMF beam

hibited the most efficient scintillator mixture, exhibiting an unchanged light yield in the beam when compared with the standard scintillating mixture. The other mould inhibitors in tested in the beam all cause the scintillator mixture light yield to decrease.

Germall Plus is the least toxic and most widely used preservative and is the most favourable choice.

5.4 Cloud Point of the Scintillating Mixture

Cloud point is the sudden onset of (reversible) turbidity in a non-ionic surfactant solution when the temperature is raised. It is caused because the solubility in water of the surfactants decreases with increasing temperature. At temperatures below the cloud point the surfactant is distributed as micelles which are stabilised by hydrogen bonding between the water molecules and oxygen atoms present in the surfactant. As the temperature increases the micelles lose their stability in the aqueous environment and agglomerate causing the solution to become cloudy in appearance. If a solution is maintained at a temperature above the cloud point the separation may become distinct.

Since the working temperature of the ND280 is expected to be increased due to mechanical heating and warm and humid summer temperatures at the experiment location there is considerable motivation to increase the cloud point temperature of the default scintillating mixture.

The surfactants contained in QSA are a blend of nonylphenol ethoxylates. These consist of a nonylphenol portion $C_9H_{19}C_6H_4OH$ which forms a hydrophobic tail and an ethylene oxide chain $[OCH_2CH_2]_n$ which forms a hydrophilic polar head group. Increasing the number of ethylene oxide chains will create more hydrogen bonds in the molecules and therefore increase the capacity to retain water and in principle raise the cloud point.

Surfactant samples comprising longer ethylene oxide chains were obtained, called Tergitol NP-13 and NP-30 [124]. These are also water-soluble nonionic nonylphenol ethoxylates. Tergitol NP-13 is an oil so could be added directly to the scintillator mixture but Tergitol NP-30 is a wax so had to be first melted then mixed with 70% water.

5.4.1 Method

Varying amounts of these extra surfactants were added to the default scintillating mixture of 70% pure water, 25% QSA and 5% Triton X-100. The cloud points of the scintillator solutions were measured in a double water bath with a slow increase in temperature applied by a hot plate and stirred with a magnetic stirrer. A mercury thermometer is used to monitor the temperature and is held in place using a clamp stand. The samples are carefully observed at each 1°C increment in temperature. The experimental setup is shown in figure 5.1. Each experiment was repeated twice.

Figure 5.1: Photograph of the apparatus used to measure scintillator solution cloud points.

5.4.2 Results - Cloud Point Test

The results are shown in table 5.3. The 3% and 7% concentration solutions with NP-30 remained turbid and white coloured and upon heating a white layer separated along the top of the solution, so the cloud point could not be determined.

Percentage (by volume) and type of extra surfactant added to standard scintillating mixture	Cloud Point 1 (±1°C)	Cloud Point 2 (±1°C)
none added	30	30
1% NP-13	31	30
3% NP-13	33	32
7% NP-13	36	35
1% NP-30	34	33

Table 5.3: Cloud point test results with added extra surfactant

5.4.3 Results - Beam Test

To test any changes in the efficiency of the scintillator solutions with added extra surfactants the samples were tested in the TRIUMF beam[1]. For full explanation of the experimental procedure refer to section 4.5. The results are shown in table 5.4.

Percentage (by volume) and type of extra surfactant added to standard scintillating mixture	Water Content	Oxygen Content (by mass)	Number of photoelectrons (from muons) ± 1.1
Standard Scintilling Solution	70%	64%	10.1
1% NP-13	69%	64%	9.1
3% NP-13	67%	62%	9.1
7% NP-13	63%	63%	8.7
1% NP-30	69%	64%	9.0

Table 5.4: Muon beam test results of scintillator solutions with with added extra surfactant

5.4.4 Conclusion

Addition of a longer ethylene oxide chain surfactant (7% Tergitol NP-13) increased the cloud point from 30°C to 36°C. Subsequent testing in the muon

[1]These beam tests were kindly carried out by Patrick Bonnick, a student at the University of British Columbia, results reproduced with permission.

beam revealed a reduction in light yield by around 10% in addition to a slight drop in oxygen content. In fact the addition of all the extra surfactants tested reduces the number of photoelectrons produced. The most favourable result is that the T2K sub-detectors be cooled and maintained at temperatures less than 25°C such that the addition of these extra surfactants will not be necessary.

5.5 Cloud Point of the Scintillating Mixture with added Biological Inhibitors

To investigate the effect of addition of biological inhibitors on the cloud point, the experiment as described in section 5.4 was repeated for scintillator samples with added biological inhibitors.

5.5.1 Results

The results are shown in table 5.5.

Water/Biological Inhibitor	Cloud Point 1 (±1°C)	Cloud Point 2 (±1°C)
DIW	30	30
PW	30	29
DIWPA	28	29
PWPA	29	28
DIWMP	30	30
PWMP	28	29
DIWGP	28	28
PWGP	29	29
DIWSA	27	27
PWSA	30	30
DIWCN	31	30
PWCN	28	27
DIWCS	28	28
PWCS	28	28
DIWPB	27	27
PWPB	29	28

Table 5.5: Cloud point test results with added biological inhibitors

5.5.2 Conclusion

Of the successful combinations that did not grow mould nor turn into a gel (DIWPA and PWPA, PWMP, PWGP, PWSA, DIWCN and PWCN and

DIWCS and PWCS) the DIWCN sample exhibited the highest cloud point. However this inhibitor is not being considered for health and safety concerns. The remaining samples all exhibit a cloud point of 28°C to 30°C, with the actual choice of added inhibitor, Germall Plus exhibiting a cloud point of 29 ±1°C.

5.6 Mechanical Design of Prototype Detector

The mechanical design for the water scintillator layers is based on a successful prototype designed for the MINOS [125] experiment and also adopted by the NOνA experiment [126]. In this design the detector will consist of planes of liquid scintillator built from layers of extruded plastic. The chosen plastic is cellular extruded twin-wall polypropylene sheets, manufactured as Correx [127] or Matraplast [128]. This plastic is favoured as it is inexpensive and easily available. Alternating x and y layers will be glued together for strength. This concept is shown diagrammatically in figure 5.2.

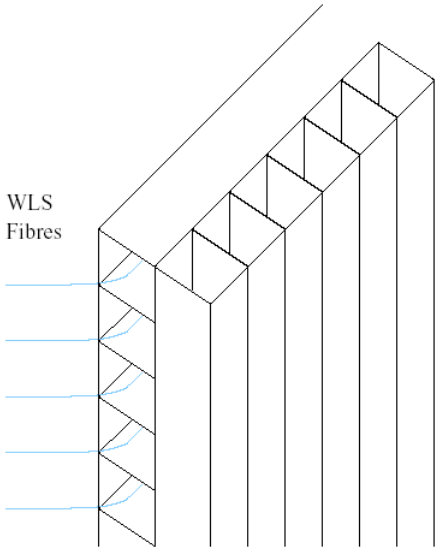

Figure 5.2: Side view of an x-y layer of extruded cells, showing WLS fibres for the x layer [129]

Scintillation light produced by the passage of a charged particle through the scintillator will be reflected inside the cell and hit the WLS fibre which will act as a light guide to transmit the trapped light to a photodetector. This concept is illustrated in figure 5.3. 1.5 mm diameter Kuraray Y11(200) WLS fibres run through the centre of each cell. In the ND280 these liquid scintillator layers will be able to replace the passive water layers in the FGD and P0D.

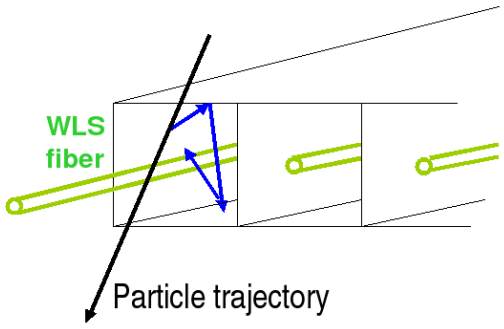

Figure 5.3: The principle of the detector [130]

5.7 Accelerated Ageing Tests of Plastics

Initial plastic tests were undertaken to determine the most appropriate plastic with which to construct the prototype. Accelerated ageing tests are based on the assumption that the chemical reactions involved in the deterioration of materials follow the Arrhenius reaction rate function [131]. This states that a 10°C increase in temperature of a homogeneous process causes the change in rate of a chemical reaction to approximately double. Therefore in order to test the durability of the plastic samples when exposed to liquid scintillator they are subjected to elevated temperatures to allow results to be obtained in a short timescale.

Samples of the following plastics were obtained: polypropylene (PP), polycarbonate (PC), polyethylene terepthalate (PET), polyethylene (PE), polytetrafluoroethene (PTFE), high density polyethylene (HDPE), nylon, oil-filled nylon, polyvinyl chloride (PVC), foam PVC, acrylic, acetal and two miscellaneous samples of Akyplen (made of PP) and a sample of Tufnol (also known as Bakerlite). A perspex oven was constructed containing a heating lamp, a fan and temperature gauges. Each plastic sample (measuring 4 cm × 4 cm) was placed in a light-tight jar of the active liquid scintillator ingredient DIPN (see section 4.3 for more information) and exposed to a temperature of 95°C for 1 week.

This high temperature was chosen as an extreme environment with which to test the plastics, such that if any survived that would be a good indication of a suitable plastic. Images of the samples before and after exposure can be found in [132]. In all the samples the DIPN changed from a clear liquid to a dark yellow liquid of varying degrees of discolouration. Samples of PVC and foam PVC leached plasticisers and stabilisers into the DIPN leaving the samples pliable and flaccid. Coloured plastic samples such as perspex and Akyplen leached colourants into the DIPN, causing discolouration. Five plastics survived this test: PET, PTFE, acetal, nylon and Tufnol. Many of the other plastics lost integrity or dissolved in the DIPN, and all the other

plastics' masses increased during the test due to absorption of DIPN.

It was realised that this test was too extreme and that the high temperature itself could cause a chemical reaction with the plastics. Therefore the experiment was repeated at lower temperature levels. Further ovens were created to operate at temperatures of 35°C and 50°C. At these temperatures the following plastics maintain integrity: PP, PC, PET, PTFE, HDPE and Tufnol. Since it is of vital importance that the detector be made out of an easily accessible material, the preferred material is Correx (PP), which is already extruded in the chosen design. Extruded sheets of PC can be found, manufactured as roofing material, but no such sheets made of PET, PTFE, HDPE or Tufnol exist.

5.8 Long Term Tests of Correx and Polycarbonate

Samples of Correx and extruded sheet PC were placed in QSA and monitored for degradation, yellowing and mass increase. 3 cm × 4 cm × 1 cm samples of twin-wall extruded white Correx and twin-wall extruded clear PC were placed in light-tight containers with 35ml QSA or distilled water. Samples were kept at room temperature, 35°C and 50°C. The masses of the plastic samples were measured to monitor any absorption of liquid into the plastic.

5.8.1 Results

The mass results are detailed in table 5.6.

Sample Contents	Temperature	Initial Mass	Mass Increase
Correx, QSA	RT	1 g	0.1 g (721 days)
Correx, distilled water	RT	1 g	none (721 days)
Correx, QSA	35°C	2.2 g	0.1 g (707 days)
Correx, distilled water	35°C	2.3 g	none (707 days)
Correx, QSA	50°C	2.3 g	0.1 g (707 days)
Correx, distilled water	50°C	2.3 g	none(707 days)
PC, QSA	RT	1.2 g	0.4 g (743 days)
PC, distilled water	RT	1 g	none (743 days)
PC, QSA	35°C	1.5 g	0.5 g (743 days)
PC, distilled water	35°C	2.3 g	none (743 days)
PC, QSA	50°C	1.5 g	0.5 g (743 days)
PC, distilled water	50°C	1.5 g	none(743 days)

Table 5.6: Observations of unpainted Correx and Polycarbonate

5.8.2 Conclusion

All the room temperature samples exhibit no change in the plastic or the QSA. For the samples maintained at 35°C and 50°C the plastics appear to be unchanged in appearance but the QSA shows a slight yellow discolouration after over 700 days exposure, with a greater degree of yellowing in the hotter oven. Although the appearance of the Correx seems unchanged, an experiment to measure any change in the Correx strength will be discussed in section 5.12.

A small mass increase observed for the Correx samples does not increase after around 100 days exposure. A 30% increase in mass for the PC samples means that Correx is preferred from this test. This small mass increase is not anticipated to cause any problems for the experiment.

5.9 Adhesive Tests

Since the scintillator layers will need to be glued together to form the detector, eight possible adhesives were selected for their ability to adhere to plastics. The chosen adhesives were: Araldite, Tensol, Fast Glass (fine and coarse), Solvent Cement, JB Weld, Stick Weld and Dielectric Polymers NT-988 High Tack Laminating Adhesive. Araldite is a well-known and widely available epoxy resin. Tensol is a single component cement which hardens due to solvent evaporation [133]. Fast Glass consists of a Glass Fibre sheet (a soft, flexible cloth available in coarse and fine weavings) which is covered in a mix of resin and hardener to form a strong reinforced plastic. JB Weld and Stick Weld are steel reinforced sealants; JB Weld is a two part mix of steel reinforced component and hardener and Stick Weld is a steel reinforced adhesive sealant putty that must be sufficiently kneaded before application. Dielectric Polymers NT-988 High Tack Laminating Adhesive is an acrylic copolymer adhesive with silicone treated paper liner. It is specially developed to adhere to low energy surfaces, such as polypropylene, so called because the forces between the hydrocarbon molecules that make up the polymer are weak and therefore liquids tend to form droplets on the surface rather than spread out.

An experiment was designed to investigate how Correx and the adhesive survived with exposure to QSA. The experiment consisted of pieces of Correx glued together with the various adhesives and exposed to QSA. The strength of the adhesives before and after exposure were then measured.

The strength tests were performed on a Hounsfield Universal Testing Machine [134]. The machine was loaded with a 10 kN load cell allowing it to apply up to 10 kN in tension or compression. A constant extension was applied via a moving cross-head, set to a constant speed of 5mm/min. Force is monitored in the load cell using a temperature compensating full bridge strain gauge configuration (a Wheatstone bridge where all four resistive arms are replaced by active strain gauges, whose electrical resistance varies in

proportion to the amount of strain).

5.9.1 Sample Preparation

3 cm × 3 cm pieces of Correx were cut. One surface of each piece was abrased with rough sandpaper and cleaned with isopropyl alcohol (IPA). The adhesives were prepared as per manufacturer's instructions and applied to each of the abrased surfaces. These surfaces were pressed together and the samples left to set overnight supported in a clamped vice. Three such samples glued with each adhesive were made. The three glued samples were then placed into a sample jar containing 190 ml of QSA and placed in a light-tight 35°C oven.

To test the glue strength after exposure to QSA, the samples were removed (monthly) from the jars, cleaned with IPA and allowed to dry. Specially made metal rods were inserted into the central flutes of the Correx. A small hole was drilled into the side of the Correx to allow another metal rod to screw perpendicularly into the first rod. This second rod was then inserted into the clamps of the Hounsfield Testing Machine. The Hounsfield Universal Testing Machine and a glued sample are shown in figure 5.4.

The machine software produces a graph of force versus extension as extension is applied. The tensile strength is recorded as the maximum force reached at the instant the two glued pieces start to separate.

5.9.2 Results

Figure 5.5 displays a force/extension graph produced by the Hounsfield Testing Machine. The graphs in general exhibit a straight line region where the cross-head is advancing at a constant speed until the system yields and the glued surface start to separate, whereupon the curves become irregular until the pieces separate.

After one month exposure the samples glued with Tensol, Solvent Cement and NT-988 High Tack Laminating Adhesive were already separated and no longer effectively glued. The results of the mean tensile strength for the remaining samples, which survived exposure for 5 months are illustrated in graphs 5.6 and 5.7.

5.9.3 Conclusion

In this experiment the main sources of error arise from inconsistencies in gluing the samples. Although utmost care is taken to ensure the same method is used to prepare all of the samples, uncertainties may arise in the amount and uniformity of the adhesive applied. Three samples were tested for each adhesive and each exposure time in an attempt to reduce this error. The Hounsfield Testing Machine performs measurements with an accuracy of 0.5%.

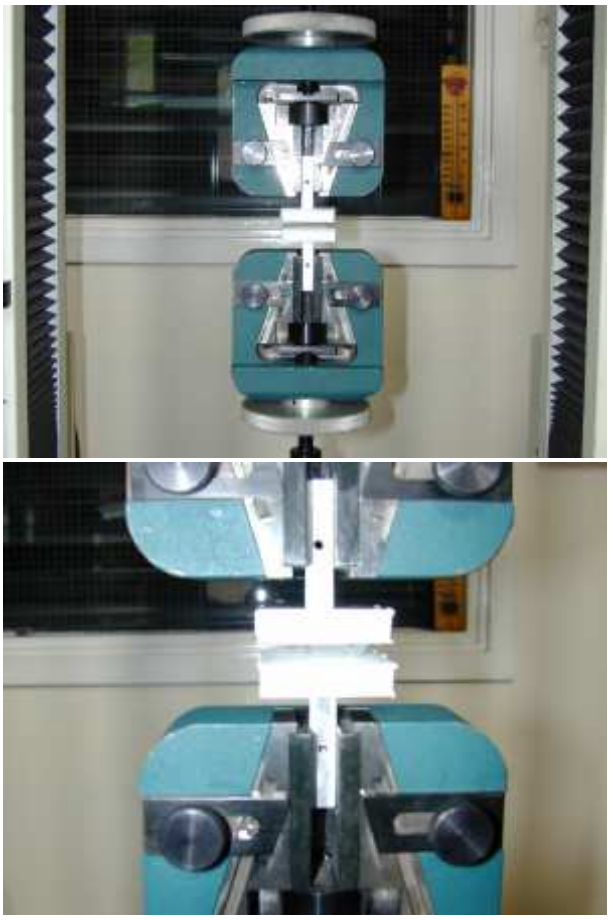

Figure 5.4: The Hounsfield Testing Machine performing a glue strength test (top) and close up view of a glued sample becoming separated (bottom).

It soon became apparent that Tensol, Solvent Cement and NT-988 High Tack Laminating Adhesive were unsuitable for use as an adhesive in this experiment. The remaining samples glued with Fast Glass (fine and coarse), Araldite and JB Weld all survived the 5 month exposure time. The change in the measured mean tensile strength over the 5 months exposure times for the Fast Glass coarse and fine samples have been illustrated in figure 5.6. These two graphs illustrate quite inconsistent patterns of change of the mean tensile strength over the exposed period. For the purposes of this detector a consistently reliable gluing process will be required to ensure confidence in mass-producing the planes of the detector. Due to the fluctuations in the measurements for these two adhesives, neither is considered optimal for use in this experiment. Furthermore the process of gluing with these adhesives is a difficult and rather untidy process; the glass fibre that must be cut to the correct size is flimsy and breakable and labourious to manage when it is covered in the mixture of resin and hardener. It is difficult to lay flat between the surfaces and to maintain a consistency in the samples. On a large scale

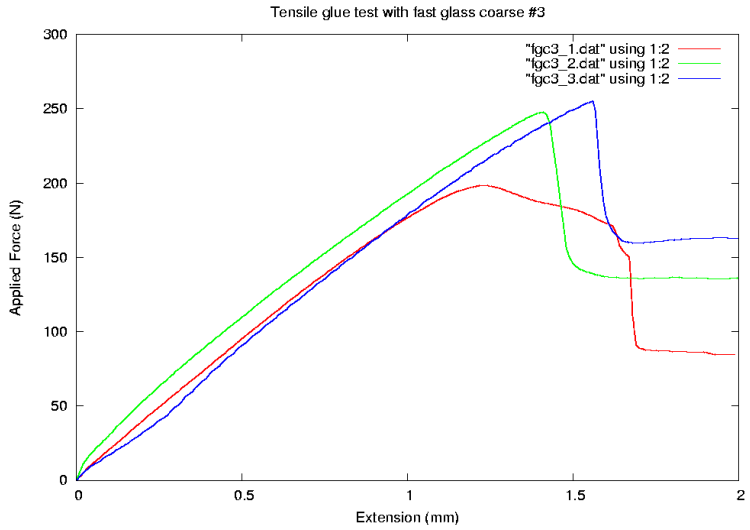

Figure 5.5: Fast Glass (coarse) 3 months exposure to QSA (mean tensile strength 234±15N)

these difficulties would be even more pronounced.

The change in the measured mean tensile strength over the 5 months exposure times for the Araldite and JB Weld samples has been illustrated in figure 5.7. The two graphs display somewhat more consistent behaviour. In terms of a realistic detector Araldite is easier to use on a larger scale since moulding the JB Weld putty is also quite laborious and would be difficult on a larger scale. Furthermore Araldite is the adhesive chosen for the gluing of scintillator to lead in the DSEcal.

5.10 Reflectance Measurements

Since scintillation light may be reflected many times before being collected by the WLS fibre, the reflectivity of the cell walls is a critical factor in maximising the light collection from the passage of a charged particle through the scintillator.

5.10.1 Method

Diffuse spectral reflectance measurements of plastic samples were undertaken with an integrating sphere, which is essentially a hollow cavity coated with a high diffuse reflectance material and with relatively small holes for sample entrance and exit ports. The equipment used was an OL Series 750 Spectroradiometric Measurement System and its Integrating Sphere Reflectance Attachment, made by Optronic Laboratories Inc [105].

The equipment consists of a source module containing a quartz-halogen lamp and a single monochromator with its output collected by the Integrat-

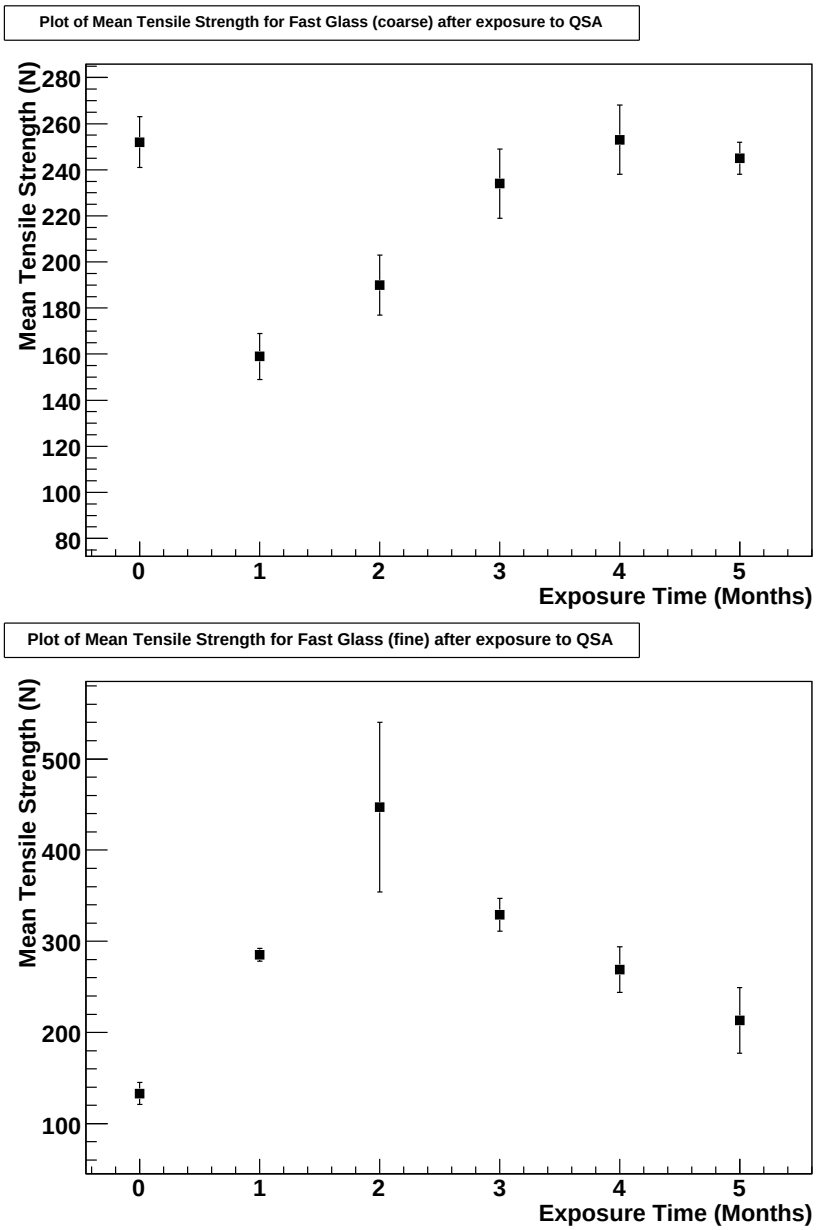

Figure 5.6: Plot of Mean Tensile Strength after exposure to QSA for Fast Glass (course) (top) and Fast Glass (fine) (bottom)

ing Sphere Reflectance Attachment and focused into the integrating sphere, the inside of which is coated with highly reflective PTFE. A pivoting mirror acts as the beam switch, which can be positioned to direct the beam onto either the "sample" port or the internal sphere wall for "comparison" measurements. The Integrating Sphere Attachment measures ρ_{18h} that is, the total hemispherical reflectance (the integral of all photons reflected from the surface at any angle) when the incident light falls on the surface at 18° from the perpendicular. A silicon detector is positioned on a port mounted on top

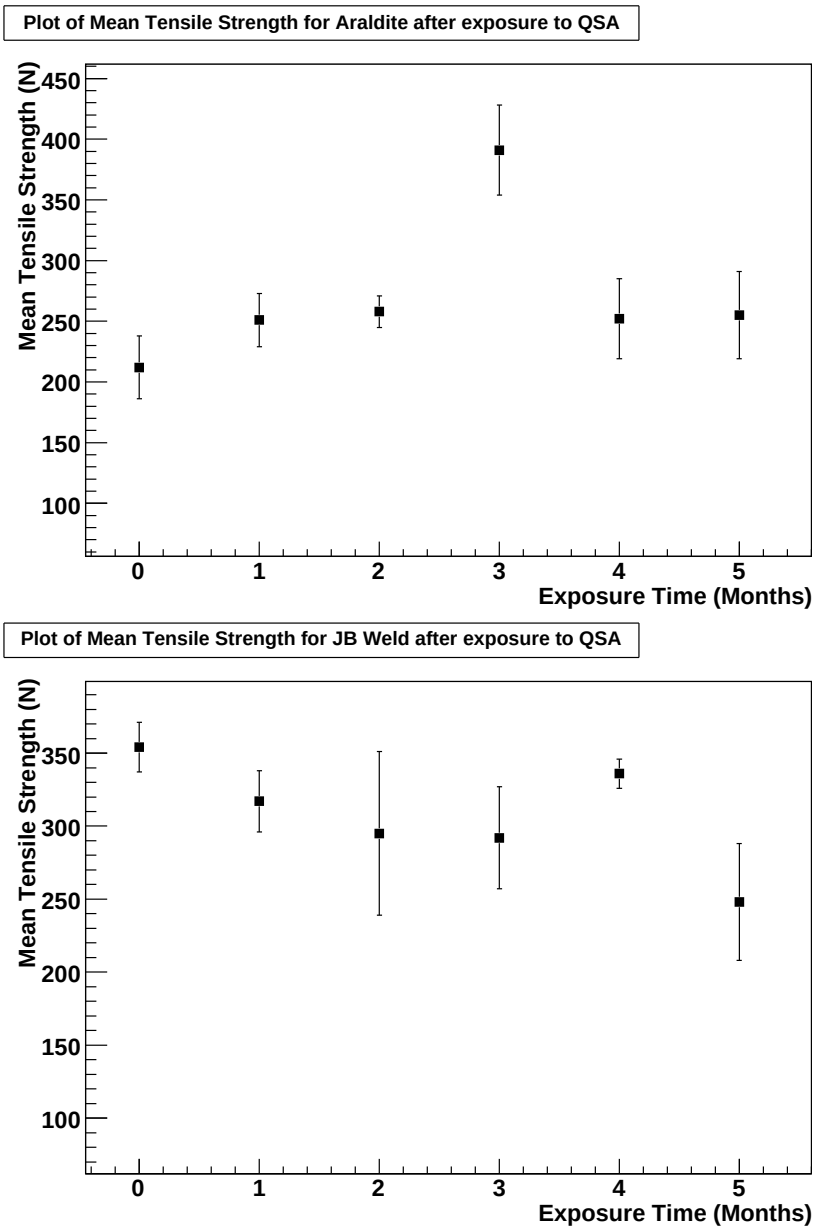

Figure 5.7: Plot of Mean Tensile Strength after exposure to QSA for Araldite (top) and JB Weld (bottom)

of the integrating sphere. A separate controller houses all data acquisition and control electronics and the entire system is computer controlled using software from Optronic Laboratories.

Calibration is first performed with a standard pressed PTFE powder reflectance sample placed in the sample port. In this way the measurements are traceable back to National Institute of Standards and Technology (NIST) standards [136]. A calibration scan is recorded as the first scan on each occasion the equipment is used. Signal readings are recorded over the wavelength

range 300 to 700 nm in the "comparison" and "sample" port positions. The calibration factor ($C(\lambda)$) is calculated by:

$$C(\lambda) = \frac{R_S(\lambda)S_{CS}(\lambda)}{S_S(\lambda)} \tag{5.1}$$

where

$C(\lambda)$ = the spectral calibration factor for the reflectance attachment
$R_S(\lambda)$ = the reflectance of the standard reference sample
$S_{CS}(\lambda)$ = the signal with the beam focused on the comparison sample
$S_S(\lambda)$ = the signal with the beam focused on the standard reference sample

The plastic sample is then placed into the sample port and the signal readings recorded in the "comparison" and "sample" positions over the same wavelength region. The reflectance ($R_T(\lambda)$) of the the test sample is given by:

$$R_T(\lambda) = \frac{C(\lambda)S_T(\lambda)}{S_{CT}(\lambda)} = R_S(\lambda)\frac{S_{CS}(\lambda)}{S_{CT}(\lambda)}\frac{S_T(\lambda)}{S_S(\lambda)} \tag{5.2}$$

where

$R_T(\lambda)$ = the spectral reflectance of the test sample
$S_{CT}(\lambda)$ = the signal with the beam focused on the comparison sample
$S_T(\lambda)$ = the signal with the beam focused on the test sample
$C(\lambda)$ = the spectral calibration factor for the reflectance attachment

Pieces of Correx were cleaned with alcohol, abrased with sandpaper and painted with three different primers: Krylon Fusion for Plastic (P1), Rust-Oleum Speciality Plastic Primer (P2) and Dr Schoch Polypropylene Primer (DSP). These primers are required as polypropylene (PP) exhibits a low surface tension interface which is notoriously difficult to paint and until recently required specialist pre-treatment. The samples were then coated with Eljen-520 [137] reflective paint. This paint consists of a titanium dioxide pigment and a paint base selected for its inertness to the solvent action of liquid scintillators. For each sample, a measurement scan was repeated three times and a mean reflectance calculated.

Since mould was observed to form in the standard scintillator mixture (as described in section 5.3) an anti-fouling paint was identified. This paint, Seajet 034 Emperor [138], contains cuprous thiocycanate (used as a pesticide) and zincpyrithone (antibacterial) as anti-fouling agents. Samples of Correx were painted with primers and this anti-fouling paint were also tested.

5.10.2 Results

The measured reflectances of Correx, unpainted and painted with primers and primers and Eljen-520 are shown in figures 5.8 and 5.9.

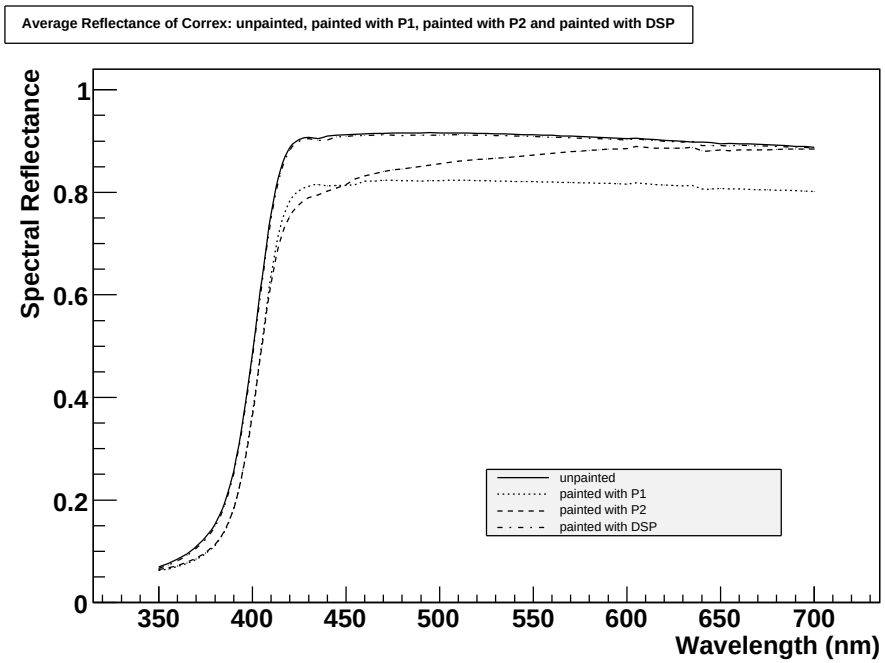

Figure 5.8: Reflectance of Correx: unpainted and painted with primers P1, P2 and DSP

The reflectance results for Correx painted with P1, P2, DSP as well as Krylon Fusion for Plastic in black followed by anti-fouling paint is illustrated in figure 5.10.

5.10.3 Conclusion

The reflectance of Correx has been measured and is shown in figure 5.8. The reflectance after painting with various polypropylene appropriate primers is also shown in this figure. Interestingly, Correx which has been treated with P1 and P2 has reduced reflectance compared to unpainted, by approximately 25% at 400nm in both cases. The reflectance of Correx painted with P1 remains reduced by about 10% to that of unpainted at wavelengths longer than around 430nm whereas the reflectance of Correx treated with P2 steadily increases at these wavelengths. By contrast treatment with DSP makes almost no difference to the reflectance.

Figure 5.9 displays the average reflectance of unpainted Correx, and Correx that has been painted with Eljen-520 over the primer coatings. At wavelengths shorter than 420nm unpainted Correx has a higher reflectance, by as much as 20% at some wavelengths. At 420nm and longer wavelengths

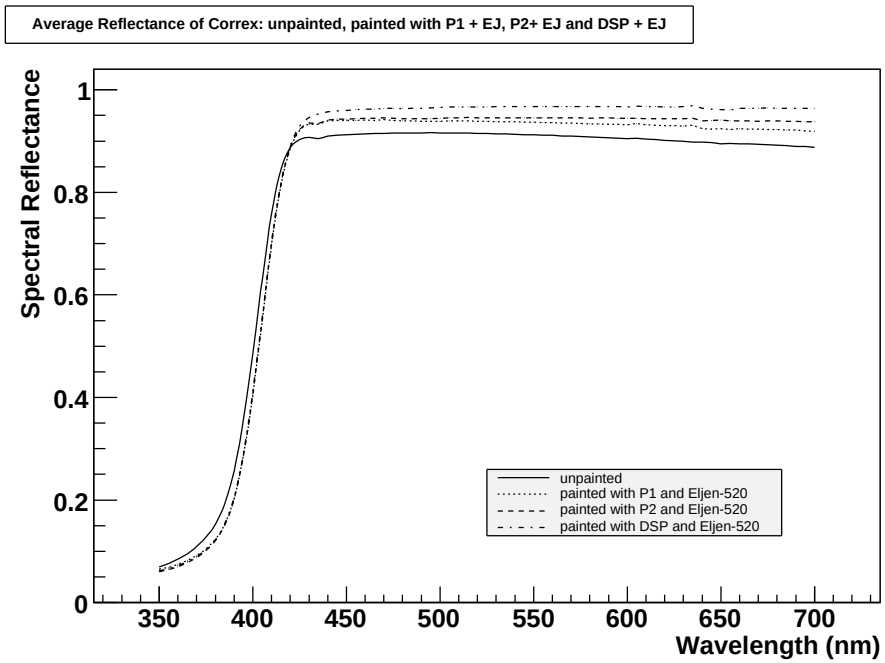

Figure 5.9: Reflectance of Correx: unpainted and painted with Eljen-520 over primers P1, P2 and DSP

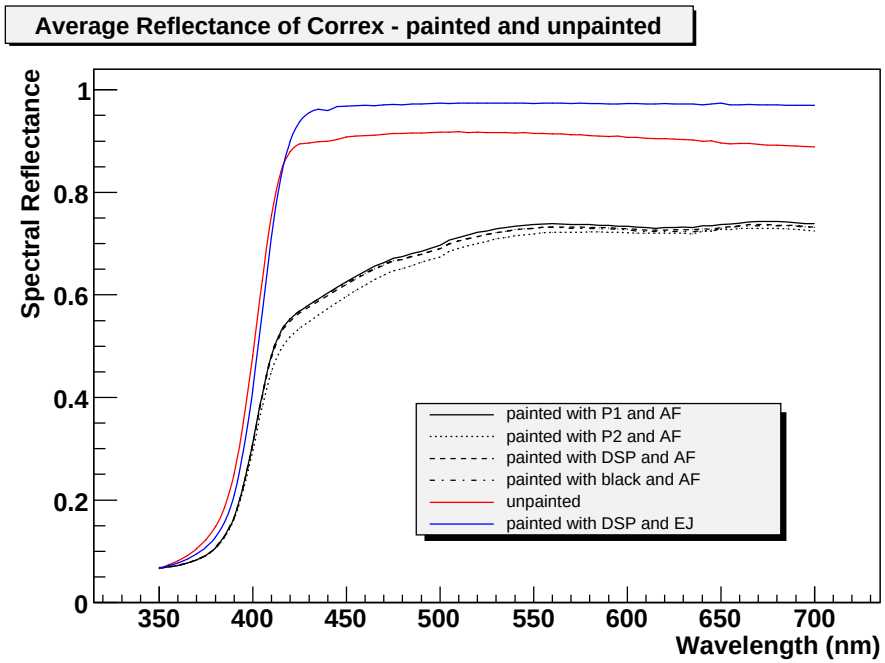

Figure 5.10: Reflectance of Correx: unpainted and painted with Seajet Emperor 034 anti-fouling paint over primers P1, P2 and DSP, unpainted Correx and Correx painted with Dr Schoch primer and Eljen-520 are included for comparison.

the painted samples have a higher reflectance when compared to unpainted. At 425nm P1 and Eljen-520 and P2 and Eljen-520 increase the reflectance by approximately 2.2%. However there is no statistical significance between the difference between the two coatings, until the wavelength is increased to around 640nm.

At 425nm DSP and Eljen-520 increase the reflectance compared to unpainted by 2.9%, which is compatible with that from the P1 and P2 primers. At 435nm DSP and Eljen-520 increases the reflectance by 4.9% above unpainted, which is a significant increase above the other two primers. Thereafter using DSP and Eljen-520 systematically improves the reflectance of Correx to the highest levels attained by any treatment in this study.

As can be seen on figure 5.10 painting the Correx surface with anti-fouling paint drastically reduces the reflectance of the surface by as much as a third. Ultimately the final choice will be determined by which paint can protect the Correx from degradation by the liquid scintillator.

5.11 Long Term Tests of Painted Correx

There is considerable motivation to apply a layer of protective paint to the Correx, to increase its resistance to chemical attack from the liquid scintillator. The identified primers and suitable paint have been described in subsection 5.10.1. The initial challenge was to effectively coat the surfaces of the Correx, made more difficult by the long thin flute design. Various methods were attempted to completely coat Correx flutes, the simplest being to submerge the flute into a bath of paint and rotate, allow the coat to dry and repeat. Some success was achieved using sponges soaked in paint/primer threaded onto wire and repeatedly passed through the Correx flutes, although this was time consuming and quality varied. Some success was also achieved using an airbrush technique [108].

In the first instance it was decided to expose small samples of Correx (4 cm $\times$ 3 cm $\times$ 1 cm) to liquid scintillator. The samples were cleaned with IPA and then sanded to roughen all the surfaces and cleaned again. The samples were painted with the primers and Eljen-520 as per the manufacturer instructions and a minimum of three coats of paint/primer were applied (after drying each time) to try to ensure total covering of the plastic. The samples were then placed in jars of 70 ml QSA and left in light-tight ovens at 35°C and 50°C as well as room temperature.

5.11.1 Results

The observations of the painted Correx samples are described in table 5.7.

5.11.2 Long Term Tests of Correx Painted with Anti-Fouling paint

The same experiment was performed with Correx samples painted with the anti-fouling paint. This paint could not survive any exposure to QSA, the paint peels away and dissolves into the scintillator, discolouring it dark brown and leaving a white sediment in the jar.

5.11.3 Conclusion

The room temperature samples have survived exposure to QSA fairly well, but there is some evidence of paint starting to peel. The higher temperature samples have all suffered from paint peeling and yellowing of the QSA, regardless of which primers were used. The sample masses were recorded before and after exposure to the liquids, however it is likely that the masses measured after exposure do not reflect a true mass increase because of the paint peeling a lot of fluid remained on the sample that could not be dried. Even painted samples that had been left in distilled water suffered from blistering and bubbling of the paint surface. The samples painted with anti-fouling paint faired even worse as all the paint peeled off and discoloured a dark brown.

5.12 Strength Tests of Correx

Since the Correx is subject to chemical attack from the liquid scintillator strength tests were performed on samples of Correx to investigate if the strength of the plastic was degraded over time after exposure to the liquid scintillator. The plastic strength tests are performed on a Hounsfield Universal Testing Machine [134]. In the three-point bend test, force is gradually applied to a plastic sample until the sample begins to compress. Each Correx sample is supported by two adjustable support arms. A third contact point travels down at a constant speed applying constant extension to the sample up until its fracture point. In this regime the strengths of different samples can be compared by the maximum load recorded.

Correx is cut into pieces 8 cm $\times$ 3 cm $\times$ 1 cm. Three such pieces were then placed in sample jars containing 190 ml QSA and placed light-tight in a 50°C oven. Each month one jar was removed from the oven and the three samples cleaned with IPA and allowed to dry before the three-point bend test was performed on each sample. The apparatus for the three-point bend test is illustrated in figure 5.11.

5.12.1 Results

An applied force versus extension graph produced by the Hounsfield testing machine software is shown in figure 5.12. The graphs in general exhibit a

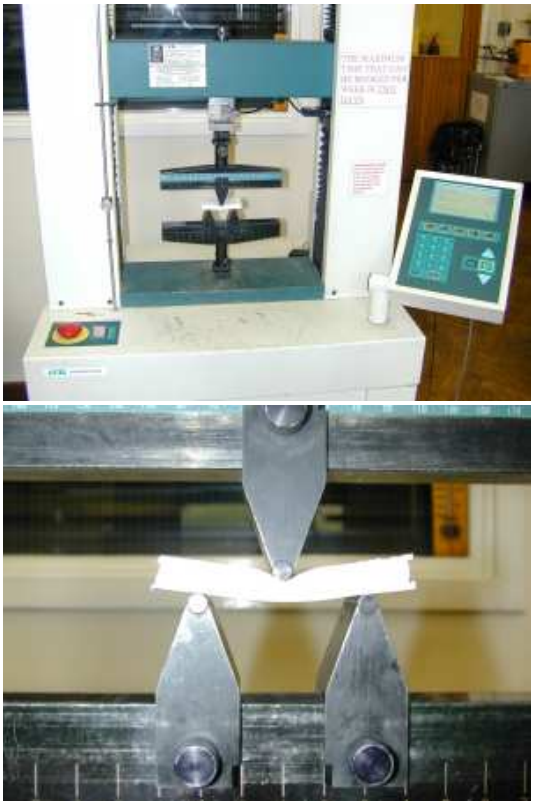

Figure 5.11: The Hounsfield Testing Machine performing a three point bend test (top) and zoomed in view to the sample (bottom).

straight line region where the third point is advancing at constant speed until the sample starts to yield. The mean maximum load recorded by the Hounsfield testing machine for each set of three Correx samples (unpainted and painted) after exposure to QSA are shown in figure 5.13.

5.12.2 Conclusion

The strength of Correx has been characterised by a measurement of the mean maximum load as measured by a 3 point bend test. After 5 months exposure unpainted Correx reduces in strength by 62±5 % and painted Correx reduces in strength by 63±5 % after 4 months exposure to QSA. These strength measurements stabilise after an initial large drop after 1-2 months exposure. Since the layer of paint does not survive the long term tests, there is no difference in the strength of Correx when painted or unpainted and although the strength of the plastic is reduced after an initial drop it stabilises.

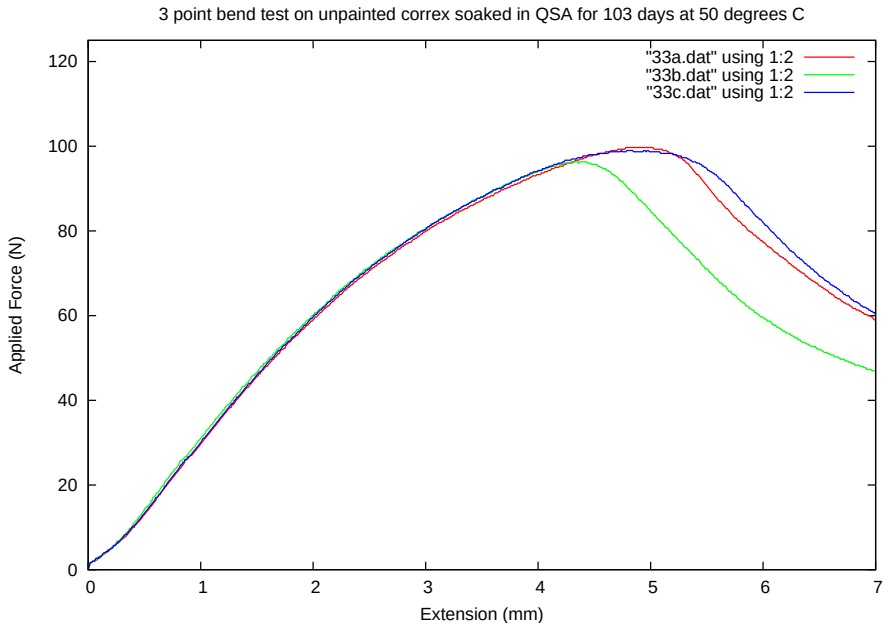

Figure 5.12: Graph illustrating the extension caused by an applied force to Correx soaked in QSA at 50°C for 5 months (mean maximum load 98±2 N)

5.13 Discussion

A default scintillating mixture of 70% pure water, 25% QSA and 5% Triton X-100 was chosen after a myriad of scintillator cocktails were tested in the TRIUMF muon and proton beams. Long term observations of QSA reveal it to discolour yellow after exposure to light and heat, however long term observations of the water/QSA/surfactant mixture do not exhibit this discolouration as long as it is left light-tight and maintained at temperatures less than 37°C (observations recorded at 25°C). Unfortunately adding water to liquid scintillator provides a favourable environment for fungal growth. A long term test of various biological inhibitors was undertaken to attempt to find a suitable inhibitor that would prevent the growth of mould but not effect the scintillation efficiency. Sixteen scintillator and mould inhibitor samples were produced and maintained at room temperature, 25°C and 37°C. At 37°C all of the samples discolour to varying shades of yellow to brown. However at 25°C, a more realistic temperature that the T2K detector may have to withstand, eight samples remain mould free after over 250 days exposure. Ultimately Germall Plus (a biological inhibitor commonly used in the cosmetics industry) was chosen after TRIUMF beam measurements and experimental safety constraints were taken into consideration. The addition of Germall Plus also did not effect the cloud point of the scintillator mixture within experimental errors. Although the cloud point temperature was raised with the addition of extra surfactants, the scintillation efficiency was reduced. It is hoped that the T2K sub-detectors will be maintained at a

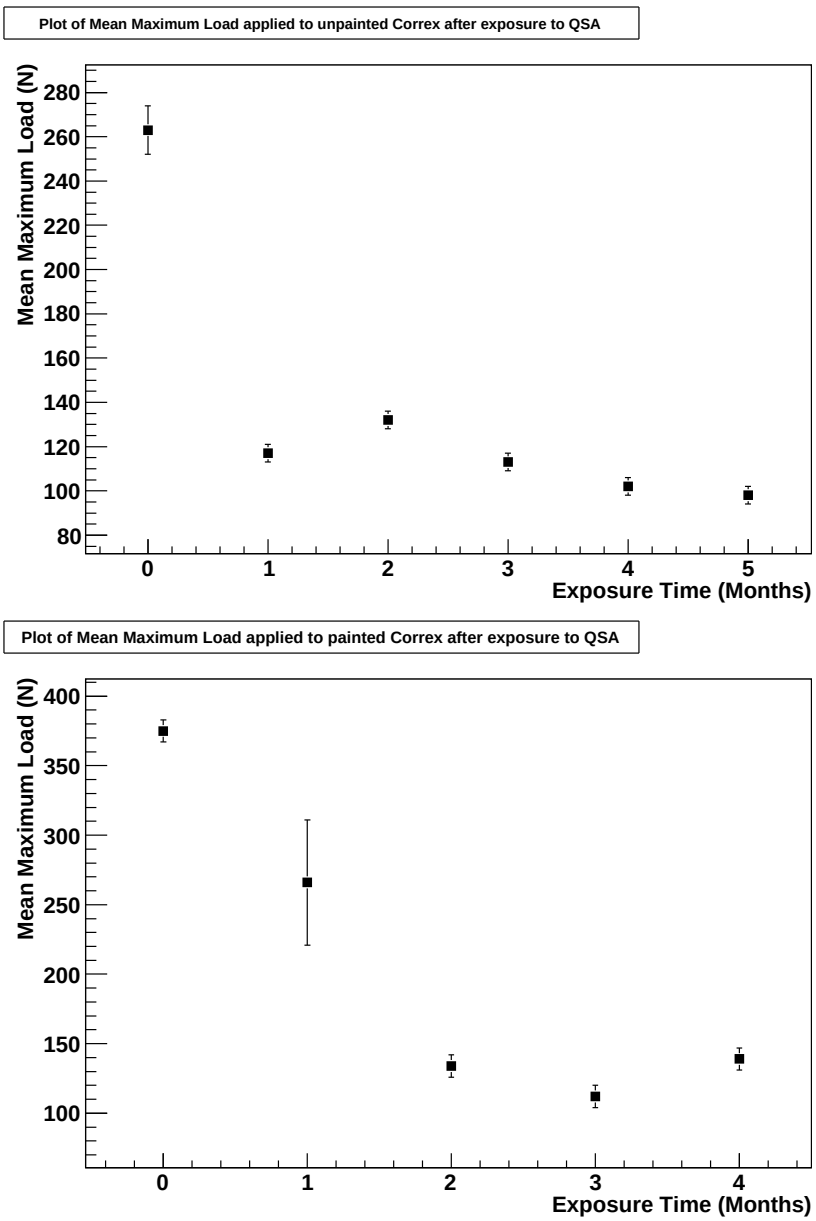

Figure 5.13: Plot of Mean Maximum Load after exposure to QSA for unpainted Correx (top) and Correx painted with Eljen-520 (bottom)

temperature less than 29°C. In summary, the default scintillating mixture is 70% water, 25% QSA and 5% TX100 plus 0.5% of mould inhibitor Germall Plus.

Twin-walled extruded white Correx is chosen as the most suitable plastic to form the main detector volume of the active water section of a ND280 sub-detector. White Correx appears to visibly survive after long term exposure to QSA and is chosen over a wide choice of plastics tested for this reason. It is also readily available cheap and off-the-shelf in corrugated sheets that suit

the sub-detector design.

The strength of Correx exposed to QSA has been characterised and is found that after one month's exposure the strength stabilises and although reduced, its structural integrity does not appear to be affected. It was attempted to protect the Correx from degradation by QSA by painting with a protective layer of paint. Three polypropylene appropriate primers and a paint resistant to attack by liquid scintillators were identified. Unfortunately long term tests of painted Correx revealed all samples to peel and discolour. It was also difficult to ensure that the insides of the Correx flutes were totally covered in paint with no gaps nor air bubbles. A paint identified to protect against mould damage also could not withstand exposure to QSA.

Since the reflectivity of the cell walls is a vital factor to ensure that the maximum amount of scintillation light is transferred to the photodetectors a detailed study of the reflectance of the chosen plastic was undertaken. At wavelengths shorter than 420nm the reflectance is highest when the sample is unpainted and longer than 420nm the reflectance is improved by painting with all the three primers and Eljen-520, and the reflectance is systematically increased up to longer wavelengths with DSP and Eljen-520 coatings. However long term tests do not support painting the Correx.

The sheets of Correx will be glued together in layers and various adhesives were tested and exposed to QSA. Araldite was chosen as it maintained a fairly constant strength over time, maintaining resistance to the QSA. It is also readily available and easy to use and scale up to a prototype detector.

Sample Contents	Temp	Observations	Initial Mass	Mass Increase (in 275 days)
Correx, P1, EJ, QSA	RT	slight crack in paint	3.6g	0.2g
Correx, P1, EJ, distilled water	RT	blistering of paint	4g	0.1g
Correx, P2, EJ, QSA	RT	cracks in paint	4g	0.2g
Correx, P2, EJ, distilled water	RT	blistering of paint	3.3g	0.2g
Correx, DSP, EJ, QSA	RT	cracks in paint	3.6g	0.2g
Correx, DSP, EJ, distilled water	RT	blistering of paint	3.6g	0.1g
Correx, P1, EJ, QSA	35°C	badly cracked paint, QSA yellow discolouration	3.7g	1.3g
Correx, P1, EJ, distilled water	35°C	crack in paint	4.2g	0.2g
Correx, P2, EJ, QSA	35°C	peeling paint, QSA yellow discolouration	4.3g	1g
Correx, P2, EJ, distilled water	35°C	blistered paint	3.1g	0.3g
Correx, DSP, EJ, QSA	35°C	cracked paint	3.8g	1.5g
Correx, DSP, EJ, distilled water	35°C	cracked paint	3.7g	0.2g
Correx, P1, EJ, QSA	50°C	cracked paint, QSA yellow discolouration	4.1g	1.6g
Correx, P1, EJ, distilled water	50°C	blistered paint	4.2g	0.3g
Correx, P2, EJ, QSA	50°C	paint badly peeled	4.3g	n/a lost a lot of paint
Correx, P2, EJ, distilled water	50°C	blistered paint	3.2g	0.3g
Correx, DSP, EJ, QSA	50°C	paint badly peeled	4g	1.7g
Correx, DSP, EJ, distilled water	50°C	few cracks	3.7g	0.2g

Table 5.7: Observations of Correx painted with primers Krylon Fusion for Plastic (P1), Rust-Oleum Speciality Plastic Primer (P2) and Dr Schoch Polypropylene Primer (DSP), followed by Eljen-520 (EJ) reflective paint and exposed to QSA or distilled water at different temperatures

Chapter 6

Detector Prototype

In this chapter the design, construction and testing of a detector prototype will be described. In particular comparisons between the water-based liquid scintillator and the plastic scintillator bars which will actually be used in the T2K Near Detector from day one of operation will be discussed.

6.1 Construction of a Detector Prototype

The mechanical design of the prototype detector (layers of extruded plastic with WLS fibres passing through the centre) has been described in section 5.6. Various methods to fabricate such a container were considered. In all the designs the main challenges were sealing the ends of the Correx flutes and WLS fibre feedthrough without any leakage of scintillator.

The prototype was designed with 10 channels i.e. 10 WLS fibres with a length of 30 cm. These dimensions were chosen so that the liquid scintillator container was the same size as the plastic scintillator paddles in the muon telescope, purpose built to test the prototype in the Sheffield laboratory. The muon telescope will be described in section 6.2.1.

6.1.1 Early Designs of Prototype

Early designs consisted of two or three sheets of Correx glued together in the same way as would be in the full scale detector and fabrication of various end-plugs and end-plates was attempted. The simplest design consisted of a polypropylene plate glued onto the end of the correx sheet with 0.6 mm holes drilled in for the WLS fibres to fit through. This design leaked so the Correx columns were first plugged with Silicone sealant before the plate was fixed on. Sealant was also placed all over the holes after the fibres had been fed through. Unfortunately this also leaked.

More sophisticated plugs were subsequently attempted. Tight fitting end-plugs were made for each individual square cell. One type was made with Stick Weld putty moulded around each fibre then fitted into the cell. After this method leaked, compressing the end of the Correx block with clamps

while the putty was setting was also attempted. Others plugs tried were cut from plastic with holes drilled through and fit into each cell with sealant. Unfortunately also none of these attempts proved leak-proof.

One design is illustrated in figure 6.1. It consisted of Correx sheet with a flange of Tufnol (a stable and rigid plastic consisting of multiple layers of heated and compressed thin sheet material) constructed around it. On the front of the flange another Tufnol face plate was fastened onto it, with machined holes to allow the WLS to pass. To seal the WLS fibre connections various gasket materials and sealants were used. The first was Viton, a type of rubber commonly used in O-rings and gaskets. This material has been successfully used in another liquid scintillator experiment, Zeplin 2 [139]. Unfortunately upon exposure to QSA the Viton is rapidly attacked and discolours the QSA a bright, almost illuminous yellow. Covering the Viton with a silicon sealant did not prevent the chemical attack. Another gasket sealant, Rocol Oilseal Hardsetting Sealant, was forced into the cavities and allowed to cure for 3 hours. After this time it had reached a state of reasonable solidity allowing the WLS fibres to be fed through the Tufnol flanges. The Tufnol flanges were then tightened to compress the sealant. It was hoped that compressing the sealant around the fibres would create a tight seal, but unfortunately this device leaked instantly when QSA was added.

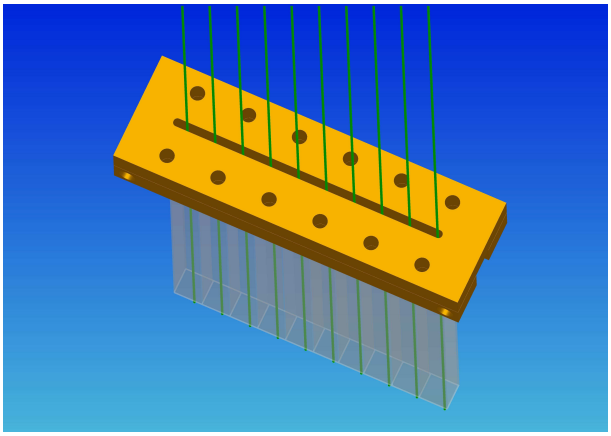

Figure 6.1: Diagram of Tufnol flange for WLS fibre feedthrough [140]

Another design explored was to place Correx sheets into a basin which would prevent leaks. The pressure of the liquid scintillator would be supported by the sides of the basin and the only role of the plastic now would be to optically separate the cells. The challenge for this design would be how to collect the WLS fibres from out of the basin. A "gutter" concept was also explored; this concept resolves the need for individual sealing of each cells by placing a single "gutter" over the ends of a panel. This concept is illustrated in figure 6.2. While this provides an obvious fill mechanism, but no satisfactory leak-proof way to join the gutter to the panel was discovered.

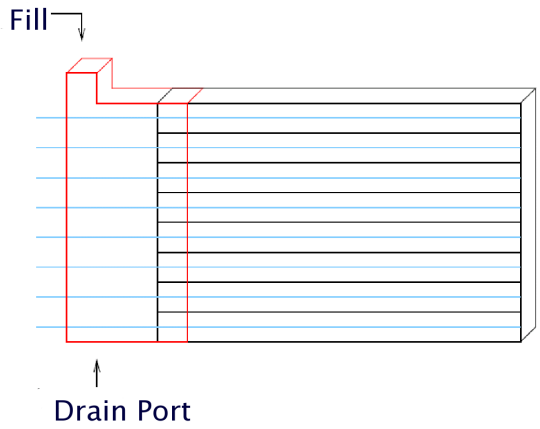

Figure 6.2: Side view of the gutter concept. Gutter (shown in red) attaches to end of Correx sheet so the end of each cell is open and the fibres pass out via the gutter [141]

6.1.2 Final Design of Prototype

Due to the leakage issues when using Correx it was ultimately decided to construct a prototype out of a solid block of material. This would negate the need to seal the ends meaning that the only serious mechanical issue is the WLS fibre feedthroughs. PTFE block was chosen which will withstand exposure to QSA and is an inert and chemically stable material. It is very non-reactive and commonly used as containers or pipework for corrosive materials. A piece of PTFE (dimensions 2 cm $\times$ 3 cm $\times$ 1.5 cm) was placed in a sample of DIPN for an extended period of time ($>$ 150 days) and showed no sign of any surface degradation. The diffuse spectral reflectance of the PTFE block was measured with an integrating sphere on an Optronic Laboratories OL750 dual grating spectroradiometer [105]. The results are illustrated in figure 6.3. The measured high reflectivity across all wavelengths is advantageous in this experiment for the maximum scintillator photon collection.

Although all of the previous designs and performance tests have centred around Correx sheets for the liquid scintillator container, at this stage it became more important to provide a realistic and stable enough container with which to test and compare the water-based scintillator with the plastic scintillator in the Sheffield neutrino laboratory. So although the PTFE was not planned to be used in a final prototype and detector, the performance of the scintillators could be measured and compared with the performance estimates as made in chapter 3.

The PTFE prototype block measures 30 cm $\times$ 13 cm $\times$ 2 cm out of which 10 channels are carved through which the WLS fibres are passed. These channels were machined on a vertical milling machine using fly cutters and end mills to the dimensions shown in the attached figure 6.4. Figure 6.4 shows the design of the prototype. Ten screws are drilled onto the lid

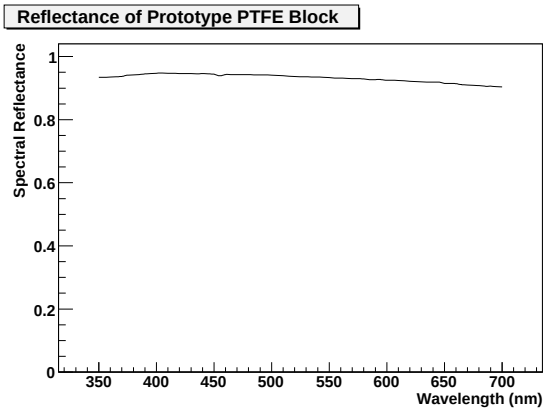

Figure 6.3: Plot of the reflectance of the PTFE block used to construct a detector prototype

allowing the lid to firmly seal the prototype detector. The channels are 0.6

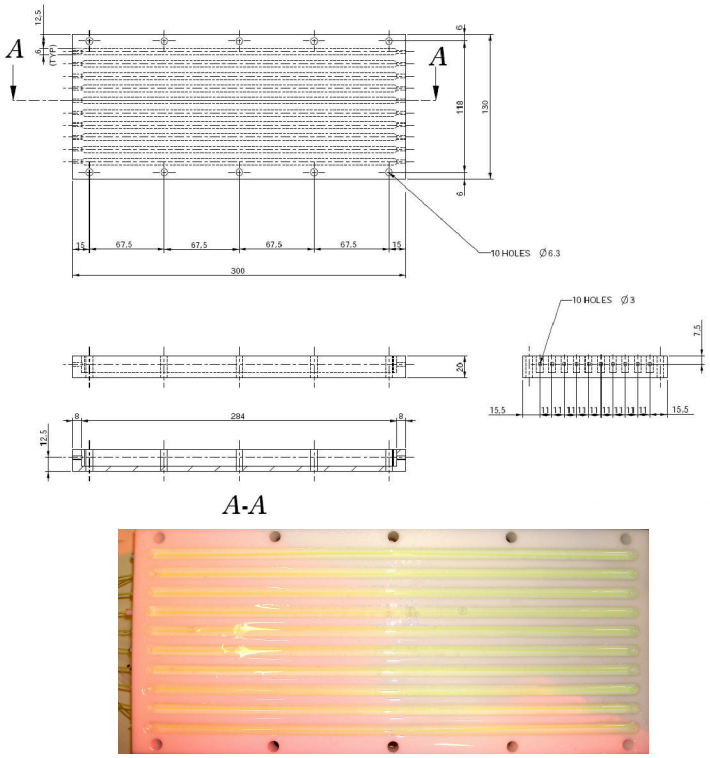

Figure 6.4: Design and dimensions of PTFE prototype; top, side and end-on view, all dimensions stated are in mm [140] (top) and top view photograph, including WLS fibres and filled with liquid scintillator (bottom)

cm wide separated by walls of thickness 0.5 mm. This wall thickness was chosen because thin samples of PTFE are visibly translucent to the naked eye. Measurements have shown that the reflectance is a strong function of

the thickness of the material [142]. The results of an experiment to measure the reflectance of PTFE of different thicknesses are displayed in figure 6.5. These results show that to attain a high reflectance over a wide range of

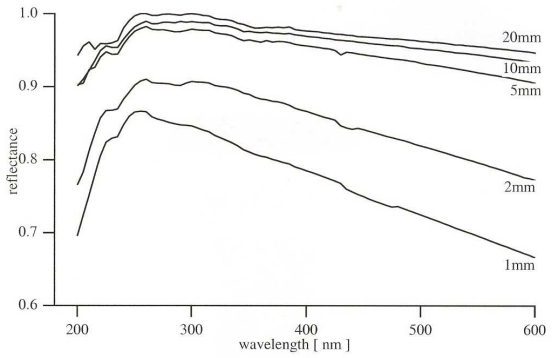

Figure 6.5: Plot of the reflectance PTFE of different thicknesses [142]

wavelengths, a thickness of more than 5 mm is required.

6.1.3 Final Fibre Feedthrough

Ultimately, none of the sealants tested could withstand long-term exposure to QSA. Various types of sealant were tested, including Wickes Silicone outdoor frame sealant, UniBond water-proof and mould resistant bath and kitchen sealant, Dow Corning Neutral Silicone, Rhodorsil acetoxy silicone, Rocol Oilseal Hardsetting Sealant, Araldite 2014 and Temflex. Additionally a gasket material (Klingersil) was tried with the compression flanges but did not compress. None of the fibre feedthrough designs that utilised any sealant could be made successfully leak-proof.

In the final design the WLS fibres are fed through PTFE tapered plugs. The design of the plugs is illustrated in figure 6.6. These were machined from a 6 mm diameter bar to the dimensions depicted in figure 6.6. They were machined on a lathe with the compound slide angled to 1.5° to achieve the inclusive angle of 3°. Firstly the WLS fibres are forced through the hole in the plug. Sometimes a small drill bit (0.7 mm) was passed through first to clear any stray PTFE blocking the hole. After some work the fibres could be made to fit through. Thereafter the tapered plugs were forced into the holes at the end of the cells as tight as possible to create an incredibly tight seal.

The ends of the fibres are prepared by sanding with wet coarse sandpaper (grading P600) followed by dry coarse sandpaper, followed by wet fine sandpaper (grading P240), followed by dry fine sandpaper. For one-sided readout one end of the fibres is cut at a 45° angle before preparation and then mirrored by gluing on a small piece of silver foil with Araldite.

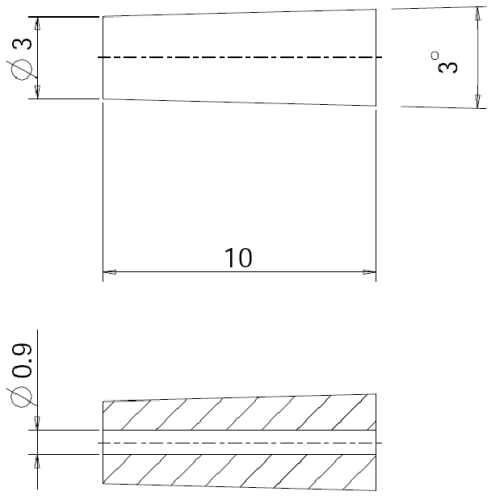

Figure 6.6: Design of PTFE tapered plug WLS fibre feedthroughs, all dimensions stated are in mm [140]

6.1.4 Filling and Draining

The prototype was filled with liquid scintillator using a pipette then the lid firmly screwed into place. Although the final prototype is a single layer, successive layers could be built up in this way.

6.2 Comparison Between Active Water and Plastic Scintillator Detector Prototypes

The efficiency of the liquid scintillator solution in the prototype detector is measured in a muon telescope. T2K plastic scintillator of the same dimensions is also tested in the same manner allowing a direct comparison of the light yields of the two scintillating materials to be made.

6.2.1 The Muon Telescope

The efficiency of scintillator samples is measured by means of the passage of cosmic-ray muons through the samples. The constructed muon telescope is shown schematically in figure 6.7. It consists of two plastic scintillator paddles Each comprises a plastic scintillator panel, a lightguide, an Electron Tubes 9813B photomultiplier (powered by a 2 kV supply) [143]. Each PMT is housed inside a protective cylindrical metal tube mount. The top paddle plastic scintillator dimensions are 15 cm × 33 cm and the bottom paddle 18.5 cm × 30 cm. The scintillator paddles are wrapped in aluminium foil then

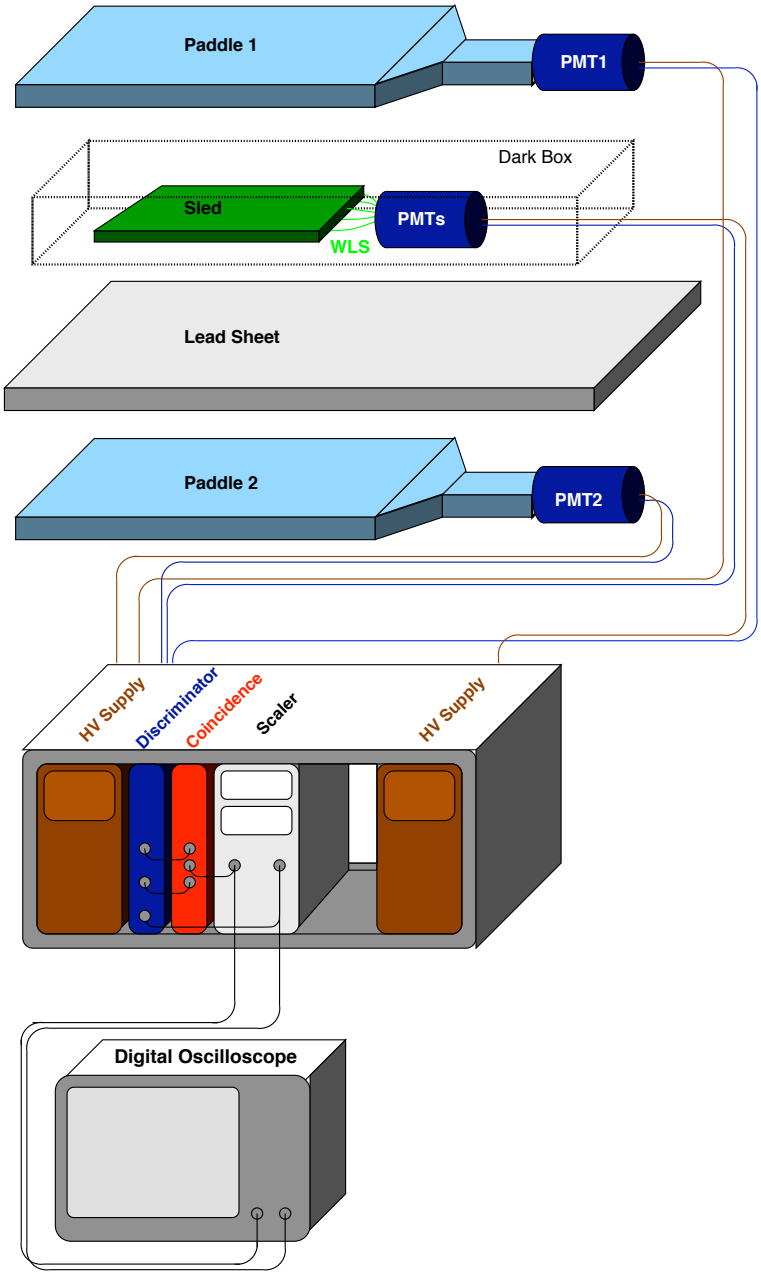

Figure 6.7: Schematic diagram of the Muon Telescope

covered in a light-tight layer of black electrical tape. In the first instance each PMT was individually tested to ensure there were no light-leaks, and the gains were adjusted to ensure both paddles exhibited similar count rates when run separately in the laboratory.

Between the plastic scintillator paddles stands a dark box which houses the prototype detector. Beneath the dark box lies a 5 cm thick layer of lead. The lead was found to reduce the rate of double coincidences between P1 and P2 by approximately 23%. The double coincidence rate of the two paddles

when orientated separately in the laboratory is approximately 5% of the flux when the paddles are in line.

10 WLS fibres from one end of the PTFE prototype are coupled to an Electron Tubes 52 mm 9813B photomultiplier, labelled PMT s on figure 6.7. The fibres are guided to the surface of the PMT by a self-made metal attachment that gathers the fibres and holds them firm to the PMT surface. Each end of the fibres is coated with Cargille optical gel (n = 1.46) to avoid any air-gaps between the fibre and the PMT surface.

The PMT outputs are coupled to a LeCroy Waverunner 6100 oscilloscope and an Ortec 401C NIM crate. The crate houses a NIM Model 623 Octal Discriminator, UCL Coincidence Unit Type N6234, Dual Scaler RL 586 and two Ortec 556 High Voltage power supplies (one supplying power to the paddles 1 and 2 and the other to PMT s inside the dark box). The entire setup is held in a secure shelving unit.

A schematic for the electronics of the telescope is illustrated in figure 6.8. One of each of the paddle PMT outputs is fed into the octal discriminator.

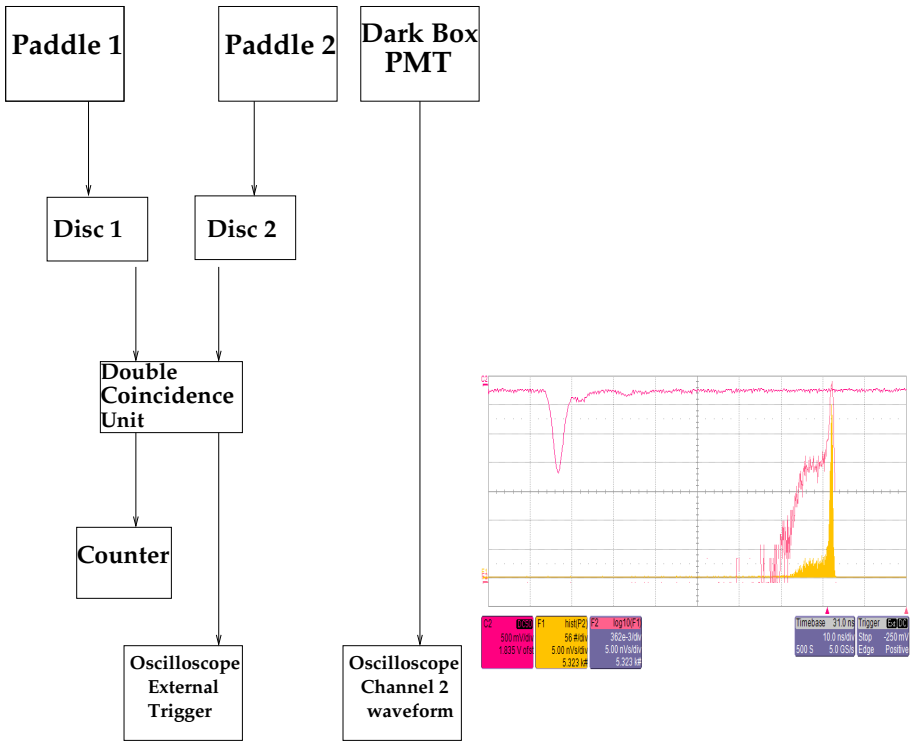

Figure 6.8: The electronics of the muon telescope

This converts the input pulse into a logic square signal (standard signal height 0.8 V), when the pulse is above a certain threshold. The width and threshold of the discriminator unit are varied by means of adjustment screws positioned on the front panel.

The electronics demands that these pulses occur within a small time window, and these “coincidences” will then be counted as cosmic ray events

through the 2 paddle scintillators. The width of all the channels is set to approximately 50 ns, a window deemed acceptable to allow "real" coincidences to occur, but with a low probability that random coincidences will occur. When a particle passes in coincidence through both of the paddles it will also pass through the scintillator sample most of the time. If it does not a pedestal will be created in the histogram which can be subtracted.

The discriminator thresholds were chosen by experimentation. A too low threshold would cause too many pulses to be triggered by noise. A too high threshold would reduce the rate of PMT pulses such that coincidences would become rarer. At present the thresholds for paddles 1 and 2 are set to approximately -900mV (the pulses are typically -1V high).

6.2.2 PMT Tests: Single Photoelectron Measurements

Before performing comparison tests of different scintillators it it vital to fully understand the PMT being used to perform the tests. The first step is to measure the single photoelectron spectrum of the dark box PMT. The single photoelectron (spe) spectrum is the spectrum of the PMT output pulses created by the entry of single electrons only into the multiplier system. This is achieved by completely darkening the photosensitive area and placing the whole system within the dark box, so it is essentially a dark current output pulse.

Integrating each pulse at different voltages within the acceptable range for the detector gives the response to the multiplier and inherent gain fluctuations. An exponential curve is expected and if observed provides not only a confirmation that the detector is working as expected, but provides a measured spe area for each particular running voltage. The spe spectrum of the dark box PMT was measured between 1.75 V tp 2 kV and the exponential relationship was observed. The relation between the spe area and applied voltage is shown in figure 6.9. The PMT was maintained at 2.1 kV for each experiment.

6.2.3 Results

Prototype detectors containing liquid scintillator and plastic scintillator bars of the same dimensions were tested in the dark box of the muon telescope. A histogram of the area of the dark box PMT lightcurve was plotted when triggered on paddles 1 and 2 double coincidences. The histogram for the plastic and liquid scintillator samples are shown in figures 6.10 and 6.11. Gaussian curves were fitted to the pedestal and signal peaks and the efficiency determined as described in section 4.5.1. The spe peak was measured separately in the dark current measurement that was repeated before and after every measurement. The average light yields determined were:

$$\text{Npe(plastic)} = 4.0 \pm 0.3 \tag{6.1}$$

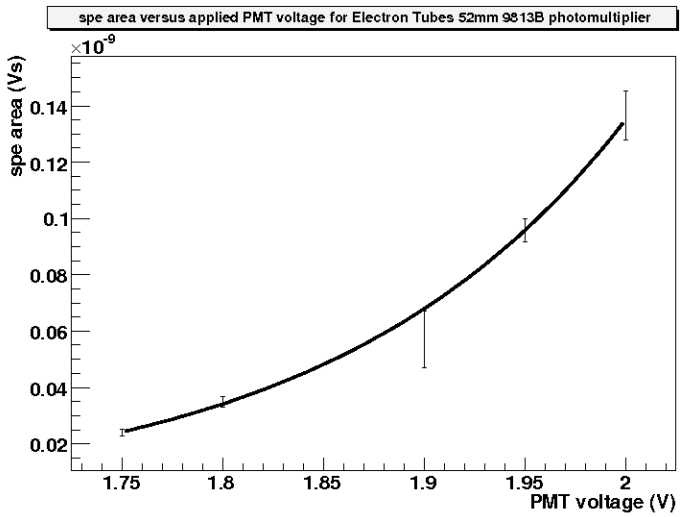

Figure 6.9: Single photoelectron pulse area versus applied PMT voltage for the dark box PMT

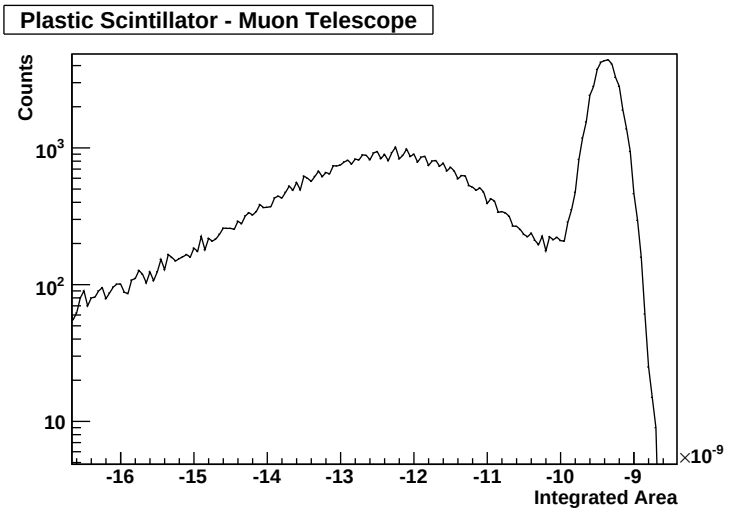

Figure 6.10: Spectrum of plastic scintillator in the muon telescope

$$\mathrm{Npe(water-based)} = 2.1 \pm 0.2 \tag{6.2}$$

6.2.4 Conclusion

The light yields of the developed liquid scintillator and T2K plastic scintillator bars have been measured in a muon telescope. An approximately 50% reduction in efficiency of the chosen water-based scintillator is observed when compared to the standard plastic scintillator. Referring back to chapter 3, a water-based scintillator with an efficiency of 40% when compared to

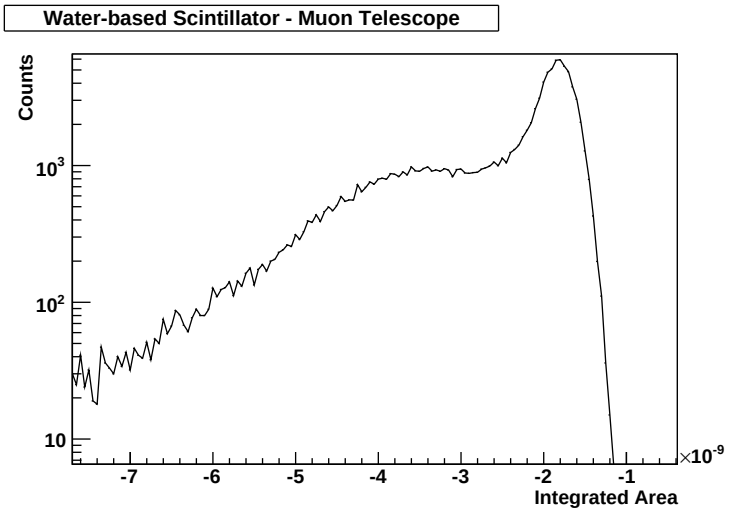

Figure 6.11: Spectrum of water-based scintillator in the muon telescope

the plastic scintillator was deemed acceptable to make a worthwhile upgrade from passive water layers to active water layers. Therefore in principle this upgrade would be a worthwhile enterprise allowing the T2K experiment to further achieve its goals.

Chapter 7

Conclusions

The T2K experiment has been designed to precisely measure some of the parameters for neutrino oscillation in a second generation experiment probing the frontiers of particle physics beyond our current Standard Model understanding. A muon neutrino beam will be fired 295 km into the Super-Kamiokande detector to search for electron neutrino appearance. The beam will be parameterised before oscillation at a distance of 280 m by a highly segmented near detector situated 2.5° off-axis (ND280).

The ND280 contains bags of pure water in some of its sub-detectors to provide an oxygen target for neutrino interactions, in an attempt to reduce systematic uncertainties arising by comparing a neutrino signal at the Super-Kamiokande water Cherenkov detector to those detected in a primarily plastic scintillator based near detector. This thesis has described the development of a water-based scintillating solution to replace the passive water layers in the ND280, providing not only an oxygen rich target, but an active component to the detector allowing greater precision measurements of the interactions within the near detector.

One way to achieve this is by increasing the detection (and therefore reconstruction) of the outgoing protons in CCQE interactions within the detector. These proton tracks are short and therefore more difficult to reconstruct especially if they occur in the uninstrumented passive water layers. A simulation study is undertaken to investigate how efficient a water-based scintillator must be in order to provide information about these tracks which would increase sensitivity to the CCQE identification, the main neutrino interaction mechanism at the oscillation maximum energy.

In chapter 3 a ND280 sub-detector is simulated, containing plastic scintillator bars interlaced with water-containing plastic flutes. Simulations are undertaken with pure water filling these flutes, then repeated with a scintillator solution of varying efficiencies when compared to a standard plastic scintillator; running at 10% increments from 10% the efficiency of plastic scintillator up to 100%. Muons are confirmed to be minimum ionising particles in their interactions within this detector and a threshold for their detection in plastic scintillator bars is determined. This threshold is then applied to the

detection of protons created in CCQE interactions, as a minimum threshold to detect these protons in the water-based layers. In this regime it is found that the water-based scintillator must be at least 40% as efficient as the plastic scintillator to be a worthwhile upgrade to the current configuration of the passive water bags within the detector. This conclusion is used as motivation to develop such a water-based scintillator.

In chapter 4 a water-based scintillator mixture is developed. It began as a default mixture comprising 70% pure water, 25% liquid scintillator QSA and 5% surfactant Triton X100. The light yield of this mixture was measured to be Npe = 10.5 ± 0.3 photoelectrons/muon or Npe = 41.04 ± 1.0 photoelectrons/proton in a beamline at TRIUMF, Vancouver. Thereafter extensive experimentation attempted to improve upon this light yield by a number of methods. Firstly QSA was synthesised in a "home-brew" as well as adding additional primary and secondary fluors to standard off-the-shelf QSA. Alternative solutes and fluors, away from the QSA recipe, were explored by firstly investigating their absorption and emission curve overlaps and formulating the most favourable options from raw ingredients, as well as other mixings procured from the Institute for Single Crystals in Ukraine. Finally a novel new recipe was tested, that of an aqueous scintillator with fluor-containing nanosuspensions. Some of these samples did not mix well with water and none of the alternatives tested yielded a light yield as high as the original mixture proposed, which was subsequently adopted as the water-based liquid scintillator mixture for this potential upgrade.

Chapter 5 detailed the extensive observing and testing phase of the scintillator mixture and materials with which a prototype detector would be made. Various mould inhibitors were tested since the mixture exhibited mould growth in aging tests. A mould inhibitor at a concentration of 1000 ppm of Germall Plus was found to be favourable after long term observation and beam tests. Cloud point measurements were also taken at the mixture containing Germall Plus exhibited a cloud point temperature (the point at which the mixture turns turbid) of 29 ± 1°C, meaning that for this scintillating mixture to be a viable upgrade the near detectors must be maintained below this temperature.

The container to house the active water will be extruded twin-wall sheets in alternating orientated layers made of plastic. Long term accelerated aging tests of plastics are undertaken since QSA is found to chemically attack and discolour upon contact with many plastics. Ready-made sheets of polypropylene named Correx are found to withstand the attack so are suitable for the detector. Various primers and paints are also tested as a protective layer but none of them are found to withstand the chemical attack from QSA, most likely because it is difficult to guarantee 100% coverage of the plastic with the paint. The reflectance of the painted and unpainted samples are measured and although the reflectance of the surface is increased by painting after 425 nm (close to the peak QSA emission of 430 nm) the paint cannot withstand long-term exposure to the QSA. The strength of Correx after long term ex-

posure to QSA is measured and found to stay constant after an initial drop in strength close to first exposure. Various adhesives are also tested after exposure to the scintillator and Araldite is found to withstand exposure so is the adhesive of choice to attach alternating layers of Correx together.

In chapter 6 a single layer small prototype detector is constructed. Due to difficulties in designing a non-leaking fibre feedthrough system, rather than use the ready-made sheets of Correx, the flutes were carved out of a single solid piece of PTFE. It is possible that if a future upgrade was undertaken Correx manufacturers would collaborate and specially manufacture sheets of Correx with sealed ends, allowing water-tight fibre feedthrough. However this is not possible for a single prototype construction so this alternative solution is implemented. The prototype is filled with the liquid scintillator mixture and its light yield measured in a purpose built muon telescope. Another prototype of the same dimensions, but made of plastic scintillator bars is also tested to directly compare the light yield of the water-based scintillator with the standard plastic scintillator. The light yield of the water-based scintillator is found to be 50% that of the plastic, meaning that if the experimental challenges such as sealing the liquid inside the Correx could be overcome that this would be a worthwhile future upgrade for the ND280.

Bibliography

[1] C. Ansel *et al*, Phys. Lett. B **667** (2008).

[2] F. Halzen and A. D. Martin, *Quarks and Leptons: An Introductory Course in Modern Particle Physics* (John Wiley and Sons, 1984).

[3] L. M. Brown, Physics Today **31 (9)** (1978).

[4] H. A. Bethe and R. E. Peierls, Nature **133**, 532 (1934).

[5] F. Reines and C. L. Cowan, Physical Review **92**, 830 (1953).

[6] G. Danby *et. al.*, Phys. Rev. Lett. **9**, 36 (1962).

[7] J. -E. Augustin *et al*, Phys. Rev. Lett **33**, 1406 (1974).

[8] J. J. Aubert *et al*, Phys. Rev. Lett. **33**, 1404 (1974).

[9] M. L. Perl *et al*, Phys. Rev. Lett. **35**, 1489 (1975).

[10] S. W. Herb *et al*, Phys. Rev. Lett. **39**, 252 (1977).

[11] F. Abe *et al*, Phys. Rev. Lett. **74**, 2626 (1995).

[12] S. Abachi *et al*, Phys. Rev. Lett. **74**, 2632 (1995).

[13] K. Kodoma *et al*, Phys. Lett. B **504**, 218 (2001).

[14] D. S. H. R. Davis Jr. and K. C. Hoffman, Phys. Rev. Lett. **20**, 1205 (1968).

[15] K. S. Hirata *et al*, Phys. Rev. Lett. **58**, 1490 (1987).

[16] R. M. Bionta *et al*, Phys. Rev. Lett. **58**, 1494 (1987).

[17] Ch. Kraus *et al*, Eur. Phys. J. **C40**, 447 (2005), hep-ex/0412056.

[18] O. Cremonesi, Nucl. Phys. B. (Proc. Suppl.) **118**, 287 (2003).

[19] K. Assamagan *et al*, Phys. Rev. D. **53**, 6065 (1996).

[20] R. Barate *et al*, Eur. Phys. J. C. **2**, 395 (1998).

[21] S. Hannestad, JCAP **05**, 4 (2003).

[22] B. Pontercorvo, Sov. Phys. JETP **6**, 429 (1957).

[23] M. N. Z. Maki and S. Sakata, Prog. Theor. Phys. **28**, 870 (1962).

[24] B. Pontercorvo, Sov. Phys. JETP **26**, 984 (1968).

[25] J. N. Bahcall *et al*, Phys. Rev. Lett. **20**, 1209 (1968).

[26] L. Wolfenstein, Phys. Rev. D **17**, 2369 (1978).

[27] Y. Oyama *et al*, Results from K2K and Status of T2K, arXiv:hep-ex/0512041v2, 2005.

[28] Y. Fuduka *et al*, Phys. Rev. Lett. **77**, 1683 (1996).

[29] Y. Fukuda *et al*, Phys. Rev. Lett. **81**, 1158 (1998).

[30] J. Bahcall and M. Pinsonneault, Rev. Mod. Phys. **67**, 1 (1995).

[31] J. N. Abdurashitov *et al*, Phys. Rev. C **60**, 055801 (1999).

[32] W. Hampel *et al*, Phys. Lett. B **447**, 127 (1997).

[33] E. Bellotti , Nucl. Phys. B. (Proceed. Suppl.) **91**, 44 (2001).

[34] M. P. J. Bahcall and S. Basu, Astrophys. J. **555**, 990 (2001).

[35] A. W. P. Poon, Int. J. Mod. Phys. **A21**, 1855 (2006).

[36] J. Boger *et al*, Nucl. Instr. and Meth. **A449**, 172 (2000).

[37] Q. R. Ahmed *et al*, Phys. Rev. Lett. **87**, 071301 (2001).

[38] Q. R. Ahmed *et al*, Phys. Rev. Lett. **89**, 011301 (2002).

[39] Q. R. Ahmed *et al*, Phys. Rev. Lett. **92**, 181301 (2004).

[40] M. Aharmim *et al*, Phys. Rev. C. **72**, 055502 (2005).

[41] V. Barger *et al*, Phys. Lett. B **537**, 179 (2002).

[42] B. Aharmim *et al*, Phys. Rev. Lett. **101**, 111301 (2008).

[43] Y. Declais *et al*, Nucl. Phys. B. **434**, 503 (1995).

[44] G. Zacek *et al*, Phys. Rev. D **34**, 2621 (1986).

[45] G. S. Vidyakin *et al*, Sov. Phys. JETP **71**, 424 (1990).

[46] A. I. Afonin *et al*, JETP Lett. **45**, 247 (1987).

[47] M. Apollonio *et al*, Phys. Lett. B **466**, 415 (1999).

[48] F. Boehm *et al*, Phys. Rev. D **64**, 112001 (2001).

[49] K. E. et al., Phys. Rev. Lett. **90**, 021802 (2003).

[50] T. Araki *et al*, Phys. Rev. Lett. **94**, 081801 (2005).

[51] V. D. Barger *et al*, Phys. Rev. Lett **92**, 2640 (1999).

[52] Y. Grossman and M. P. Worah, Atmospheric Muon Neutrino Deficit from Decoherence, arXiv:hep-ph/9807511v1, 1998.

[53] T. Schwetz, hep-ph/0710.5027v1.

[54] Y. Fukuda *et al*, Phys. Rev. Lett. **81**, 1562 (1998).

[55] T. K. Gaisser *et. al.*, Phys. Rev. D **54**, 5578 (1996).

[56] D. Casper *et al*, Phys. Rev. Lett. **66**, 2561 (1991).

[57] K. S. Hirata *et al*, Phys. Lett. B **205**, 416 (1988).

[58] K. S. Hirata *et al*, Phys. Lett. B **280**, 146 (1992).

[59] S. Fukuda *et al*, Nucl. Inst. Meth. A **501**, 418 (2003).

[60] T. Kearns, Frascati Phys. Ser. **28**, 413 (2002).

[61] Y. Ashie *et al*, Phys. Rev. Lett. **93**, 101801 (2004).

[62] Y. Abe *et al*, Phys. Rev. Lett. **97**, 171801 (2006).

[63] M. H. Ahn *et al*, Phys. Rev. Lett **90**, 041801 (2003).

[64] MINOS Collaboration, Preliminary Results from MINOS on ν_μ Disappearance Based on an Exposure of 2.5×10^{20} 120 GeV Protons on the NuMI Target, arXiv:0708.1495 (hep-ex), 2007.

[65] M. Apollonio *et al*, Eur. Phys. J. **27**, 331 (2003).

[66] J. Hosaka *et al*, Phys. Rev. D **74**, 032002 (2006).

[67] S. Yamamoto *et al*, Phys. Rev. Lett **96**, 181801 (2006).

[68] The LSND Collaboration, A. Aguilar *et al*, Phys. Rev. D **64**, 112007 (2001).

[69] M. Sorel *et al*, Phys. Rev. D **70**, 073004 (2004).

[70] T. Katori *et al*, Phys. Rev. D **74**, 105009 (2006).

[71] A. A. Aguilar-Arevalo *et al*, Phys. Rev. Lett. **98**, 231801 (2007).

[72] B. Armbruster *et al*, Phys. Rev. D **65**, 112001 (2002).

[73] B. Achkar *et al*, Nucl.Phys. **B434**, 503 (1995).

[74] MINOS Collaboration, New Results from MiniBooNE: A Search for Electron Antineutrino Appearance at 1 eV^2, arXiv:0910.0263 (hep-ex), 2009.

[75] Y. Itow *et al*, The JHF-Kamioka Neutrino Project, arXiv:hep-ex/0106019v1, 2001.

[76] The T2K Collaboration, Letter of Intent: Neutrino Oscillation Experiment at JHF, 2003.

[77] The T2K ND280 Collaboration, T2K ND280 Conceptual Design Report, DRAFT: Version 1.0, 2005.

[78] P. Lipari, Nucl. Phys. Proc. Suppl. **112**, 274 (2002).

[79] The T2K Collaboration, A Proposal to Extend T2k with a Detector 2km away from the JPARC Neutrino Source, T2K Internal Note, (2007).

[80] O. Ferreira, Private communication.

[81] A. Vacheret, Talk given at the 5th International Workshop on Neutrino-Nucleus Interactions in the Few-GeV Region, Fermi National Accelerator Laboratory, Batavia, IL, June 2007.

[82] The T2K ND280 Collaboration, ND280 TPC: Technical Design Report, Version 1.0, 2007.

[83] The T2K ND280 Collaboration, ND280 Fine-Grained Detector: Technical Design Report, Version 0.95, 2006.

[84] The T2K ND280 Collaboration, T2K ND280 Sub-Detector Review: Side Muon Range Detector, Version 4.7.1, 2007.

[85] H. Kume *et. al.*, Nucl. Inst. and Meth. **205**, 443 (1983).

[86] A. Suzuki *et. al.*, Nucl. Inst. and Meth. A **329**, 299 (1993).

[87] T. Kato, *Tau Neutrino Appearance via Neutrino Oscillations in Atmospheric Neutrinos*, PhD thesis, Stony Brook University, 2007.

[88] Y. Fukuda *et al*, Nucl. Inst. Meth. A **501**, 418 (2003).

[89] R. J. Wilkes, Private communication.

[90] GEANT4 Collaboration, Nucl. Instrum. Meth. **A506**, 250 (2003).

[91] D. Casper, Nucl. Phys. Proc. Suppl. **112**, 161 (2002).

[92] A. K. Ichikawa, Private communication.

[93] LHEP Physics Lists http://geant4.cern.ch/support.

[94] W. R. Leo, *Techniques for Nuclear and Particle Physics Experiments* (Springer-Verlag, 1987).

[95] W.-M. Yao *et al*, **33** (2006).

[96] J.B.Birks, *The Theory And Practise of Scintillation Counting* (Pergamon Press, 1964).

[97] G.F.Knoll, *Radiation Detection and Measurement* (G.Wiley and Sons, New York, 1989).

[98] R. C. Smith and K. S. Baker, Appl. Opt. **20**, 177 (1981).

[99] I. B. Berlman, *Fluorescence Spectra of Aromatic Molecules* (Academic Press, 1971).

[100] D. R. Winn and D. Raftery, IEEE Trans. Nucl. Sci. **NS-32:1** (1985).

[101] Zinsser Analytic (UK) Ltd, Unit 5, The Quadrant, Howarth Road, Maidenhead, Berkshire, SL6 1AP, *http://www.zinsser-analytic.com/137.asp.*

[102] IN/US Systems http://www.inus.com.

[103] S. Yen, Private communication.

[104] Horiba Jobin Yvon http://www.jobinyvon.co.uk/ukdivisions/fluorescence/.

[105] OL Series 750 Automated Spectroradiometric Measurement System, *Glen Spectra Ltd, 2 Dalston Gardens, Stanmore, Middlesex, HA7 1BG, http://www.glenspectra.co.uk/.*

[106] TX-100 www.roche-applied-science.com/pack-insert/1332481a.pdf.

[107] triumf http://www.triumf.ca/.

[108] H. Nakahara, Private communication.

[109] http://www.photonis.com/data/cms-resources/File/Photomultipliertubes/spec/XP2262.pdf.

[110] http://www.kuraray.co.jp/en/index.htm.

[111] L. Patsenker, Private communication.

[112] SSI Institute for Single Crystals, NAS of Ukraine, 60 Lenin Ave, Kharkov, 61001, Ukraine.

[113] *Sigma Aldrich Catalogue (Material Safety Data Sheet)*, Sigma-Aldrich Company Ltd., The Old Brickyard, New Road, Gillingham, Dorset, SP8 4XT, http://www.sigmaaldrich.com/catalog/search/ProductDetail/RIEDEL/46194.

[114] *Sigma Aldrich Catalogue (Material Safety Data Sheet)*, Sigma-Aldrich Company Ltd., The Old Brickyard, New Road, Gillingham, Dorset, SP8 4XT, http://www.sigmaaldrich.com/catalog/search/ProductDetail/RIEDEL/49795.

[115] J. C. Weekley *et. al.*, Applied Radiation and Isotopes **60**, 887 (2004).

[116] D. Zhu *et. al.*, J. Pharm. Innovation **1**, 76 (2006).

[117] M. C. E. Erickson et. al., J. Cosmet. Sci. **56**, 253 (2005).

[118] http://www.cefic.be/sector/styrene/guide9801/02.htm.

[119] *Table 1500: Solvents Having the Same Refractive Index and the Same Density at 25°C*, http://www.engineeringreference.com.

[120] http://www.robinwood.com/Catalog/Technical/Gen3DTuts/Gen3DPages/RefractionIndex

[121] M. Wainright, Private communication.

[122] Elga LabWater http://www.elgalabwater.com/.

[123] J. Dluzniewska, Electronic Journal of Polish Agricultural Universities; Agronomy **6**, 2 (2003).

[124] Dow Surfactants http://www.dow.com/surfactants/products/nonylph.htm.

[125] P. Border et. al., Nucl. Inst. Meth. A **463**, 194 (2001).

[126] D. Ayres *et al*, hep-ex/0503053.

[127] http://www.cordek.co.uk/correx/products.

[128] http://www.matraplast.com.

[129] S. Oser et. al., Feasibility studies for a finely segmented water scintillator detector version 1.0: November 26, 2004.

[130] P. Adamson *et al*, Phys. Rev. D **73**, 072002 (2006).

[131] B. J. Lambert and F. Tang, Radiation Physics and Chemistry **57** (2000).

[132] http://www.shef.ac.uk/physics/research/pppa/research/t2k.htm.

[133] Tensol Cement http://www.mcmordiebros.co.uk/tensolcement.htm.

[134] http://www.hounsfield.com.

[135] J. Workman and A. Springsteen, editors, *Applied Spectroscopy* (Academic Press, 1998).

[136] http://www.nist.gov.

[137] http://www.eljentechnology.com/.

[138] Seajet Products 034 Emperor anti-fouling paint http://www.ybw.com/ybw/seajet/products.html.

[139] P. Lightfoot, Private communication.

[140] T. Gamble, Private communication.

[141] S. Oser, Private communication.

[142] J. McMillan, Private communication.

[143] Electron Tubes http://www.et-enterprises.com/pdf/9813b.pdf.